

Interactions between a flat slab and overriding plate: Controlling factors of  
subduction dynamics and continental deformation

by

Xiaowen Liu

A thesis submitted in partial fulfillment of the requirements for the degree of

Doctor of Philosophy

in

Geophysics

Department of Physics  
University of Alberta

© Xiaowen Liu, 2022

---

## Abstract

---

Subduction zones are active plate margins that have an important role in mantle and lithosphere processes. Subduction is driven by the negative buoyancy of the downgoing oceanic plate, resulting in a steep descent angle at most subduction zones. However, in approximately 10% of modern subduction zones, shallow to flat-slab subduction occurs. In these regions, the oceanic plate unbends to become subhorizontal, underplating the continental plate for several hundred kilometers inboard of the plate margin at depths of 45-150 km. Development of a flat slab is generally characterized by migration and termination of arc magmatism, reduced continental surface heat flow, and thick-skinned deformation in the continental interior. The mechanisms that lead to flat-slab subduction include anomalous buoyancy of the oceanic plate, high trenchward velocity of the continental plate, and increased suction force in the mantle wedge. Recent studies have made significant progress in mapping flat slabs and understanding how a flat slab develops. However, there are many fundamental problems that are still not well understood, such as why the depth of the flat slab varies between different regions, and how flat slabs affect the thermal structure and deformation of the continental upper plate.

This thesis uses 2D thermal-mechanical models to investigate flat-slab dynamics and the interactions between a flat slab and the overlying continent. Models focus on regions of flat-slab subduction in western North and South America, where slab flattening is driven by a combination of trenchward continental motion and subduction of a buoyant aseismic oceanic ridge. The models show that flat-slab depth is primarily determined by the initial thickness of the overriding plate, such that the slab is deeper below an initially thick

(cool) continent. The depth is also controlled by the strength of the continental mantle lithosphere, whereby a weak (hydrated) lithosphere is able to be displaced by the flat slab. Through reasonable variations in these parameters, the depth of the flat slab varies by more than 100 km, in good agreement with observed depths. The models also indicate that the observed low surface heat flow in flat-slab regions does not solely result from conductive cooling by the cold slab. The continental lithosphere cools over 10's of millions of years through conductive heat transfer after flat-slab emplacement. The timescale of cooling is mainly controlled by flat-slab depth, with an earlier onset of cooling and a greater amount of cooling for a shallower slab. The magnitude of cooling is also enhanced by longer slab emplacement times, faster convergence rate, and an older oceanic plate. The presence of a flat slab can also trigger thick-skinned deformation of the continent 100's of km from the plate margin. Deformation is the result of both high compressional stresses through end-loading at the distal plate margin and the presence of pre-existing weak structures in the continent. Deformation is modulated by dynamic topography associated with the flat slab, where dynamic uplift inhibits deformation. The model results are in good agreement with geological and geophysical observations from flat-slab regions. This thesis provides new insights into the flat-slab regions in both North and South America and deepens our understanding of flat-slab subduction dynamics and the origin of thermal anomalies and thick-skinned deformation of the Laramide Orogeny in North America and the Sierras Pampeanas in South America.

---

## Preface

---

The work presented in this thesis is an original work by myself, Xiaowen Liu. It has been written to fulfill the requirements for the degree of Doctor of Philosophy at the University of Alberta. The work was originally inspired by my passion to study and have a better understanding of plate tectonics and dynamics of subduction zones, especially flat-slab subduction. Dr. Claire Currie, as my Ph.D. supervisor, provided helpful guidance and instruction during the program and offered constructive feedback for my dissertation.

Chapter 3 has been published as Liu, X., & Currie, C. A. (2019), “Influence of Upper Plate Structure on Flat-Slab Depth: Numerical Modelling of Subduction Dynamics”, *Journal of Geophysical Research: Solid Earth*, 124(12), 13150-13167. I was responsible for the numerical model design, modelling experiments, interpretation and manuscript preparation. Dr. Currie was the supervisory author that offered research direction, concept formation, and was involved with manuscript preparation and revision.

Chapter 4 has been published as Liu, X., Currie, C. A., & Wagner, L. S. (2021), “Cooling of the Continental Lithosphere During Flat-slab Subduction”, *Geosphere*, 18(1), 49-68. I designed the models, conducted the modelling experiments, prepare the manuscript. Dr. Currie was the supervisory author and was involved with concept formation and manuscript composition. Dr. Wagner provided the Pampean flat-slab region map and contributed to the interpretation of the model results. All co-authors were involved with manuscript revision.

Chapter 5 has been submitted to *Geology* as a manuscript entitled “Origin of Sierras Pampeanas: Flat-slab subduction and inherited structures”, by Liu, X. and Currie, C. A. I

was responsible for model set up, results analysis, and manuscript construction. Dr. Currie was the supervisory author who helped with manuscript composition and revision.

Chapter 6 of this thesis is an original work and is written as a manuscript draft, in preparation for submission to the *Journal of Geophysical Research: Solid Earth*.

---

## Acknowledgements

---

I started the journey to Ph.D. with courage and determination. This road is not easy but memorable and splendid. A look back from the finish line, I cannot stand where I am now without many people's helps. Here, I would like to express my deep and sincere gratitude to those who supported and accompanied me through this journey.

First and foremost, I would like to thank my research supervisor, Dr. Claire Currie, for her guidance, support, encouragement, and advice throughout my Ph.D. Dr. Currie is an exemplary mentor and friend to me, whose passion for science and enthusiasm for life will always motivate me. It had been a great pleasure working with Dr. Currie.

I appreciated my committee members and examiners, Dr. Stephen Johnston, Dr. David Potter, Dr. Mauricio Sacchi, and Dr. Jeroen van Hunen, for their great comments and feedback on this work, which greatly improved this thesis. I would also like to thank Dr. Vadim Kravchinsky and Dr. Martyn Unsworth who had sited on my committee for their constructive suggestions in shaping this thesis.

I would also like to thank Dr. Lara Wagner, as a co-author, for her contribution and great ideas.

Thanks to Tai-Chieh Yu, Zhihong Pan, David Quiroga, and all my fellow graduate students for those insightful discussions on research and for making my life at the University of Alberta full of joy and fun. Thanks also to Yiru Zhou for being such a good friend who provided continued help to both my academic and personal life. I would like to extend a special thank you to Hui Wang, my dear friend in China, for her time and support despite the distance and different time zones.

At last, I would like to thank my partner and family for their endless love, cheering, and support through the ups and downs. Words cannot express my gratitude for my beloved parents, without you, I might not be the person I am today.

To the future, happy and bright.

---

# Table of Contents

---

<b>Abstract .....</b>	<b>ii</b>
<b>Preface .....</b>	<b>iv</b>
<b>Acknowledgement.....</b>	<b>vi</b>
<b>Table of Content .....</b>	<b>viii</b>
<b>Lists of figures.....</b>	<b>xii</b>
<b>Lists of tables.....</b>	<b>xvii</b>
<b>Chapter 1 Introduction .....</b>	<b>1</b>
1.1    Subduction zones .....	1
1.2    Flat-slab subduction.....	4
1.3    Research objectives.....	7
1.4    Thesis outline.....	8
<b>Chapter 2 Numerical modelling method .....</b>	<b>10</b>
2.1    Governing equations .....	10
2.2    Material properties .....	13
2.3    Boundary conditions .....	15
2.4    Modelling phases .....	16
<b>Chapter 3 Influence of upper plate structure on flat-slab depth: Numerical modelling of subduction dynamics.....</b>	<b>18</b>
3.1    Introduction.....	19
3.2    Materials and methods .....	22
3.2.1    Model geometry .....	22
3.2.2    Material properties .....	24
3.2.3    Boundary conditions .....	27

3.2.4	Modelling phases .....	27
3.2.5	Flat-slab depth.....	27
3.3	Factors affecting the creation of a flat slab .....	28
3.4	Effect of continental mantle lithosphere on flat-slab depth .....	31
3.4.1	Continental lithosphere thickness .....	31
3.4.2	The strength of continental mantle lithosphere.....	33
3.4.3	Distance between craton and trench .....	35
3.5	Controls on flat-slab geometry.....	40
3.5.1	Effects of CML on flat-slab depth .....	40
3.5.2	Variations in oceanic plate age and convergence rate .....	44
3.5.3	Implications for ancient and modern flat slabs .....	46
3.5.4	Model limitations .....	49
3.6	Conclusions.....	50
3.7	Supporting information.....	51
3.7.1	Introduction.....	51
3.7.2	Effect of oceanic plateau properties on flat-slab development.....	53
3.7.3	Shallow flat slab.....	54
3.7.4	Models with weak craton CML .....	56
3.7.5	Craton mantle lithosphere density .....	57
3.7.6	Viscosity and strain rate of the reference model.....	59
<b>Chapter 4</b>	<b>Cooling of the continental plate .....</b>	<b>61</b>
4.1	Introduction.....	62
4.2	Methods.....	67
4.3	Results.....	73
4.3.1	Reference model .....	73

4.3.2	Effect of subduction angle .....	77
4.3.3	Variations in thickness of initial continental lithosphere and flat-slab depth.....	79
4.3.4	Effects of other factors .....	82
4.3.4.1	Thermal conductivity .....	82
4.3.4.2	Continental crust thickness .....	84
4.3.4.3	Convergence rate .....	84
4.3.4.4	Oceanic plate age .....	85
4.4	Discussion .....	86
4.4.1	Summary of numerical models .....	86
4.4.2	Limitation of the numerical models .....	88
4.4.3	Timescale for continental cooling.....	89
4.4.4	Implications for modern and ancient flat-slab regions .....	95
4.5	Conclusion .....	100
<b>Chapter 5 Formation of the Sierras Pampeanas during Pampean flat-slab subduction .....</b>		<b>102</b>
5.1	Introduction.....	102
5.2	Tectonics of Pampean flat subduction and the Sierras Pampeanas ....	104
5.3	Geodynamic modelling.....	106
5.4	Discussion.....	109
5.5	Implications and conclusion .....	112
5.6	Supplemental materials.....	113
5.6.1	Numerical model setup .....	113
5.6.2	Material properties .....	116
5.6.3	Boundary conditions and model initialization .....	117
5.6.4	Supplemental model plots.....	118

5.6.5	Table of model parameters.....	121
<b>Chapter 6 Controlling factors of inboard deformation .....</b>		<b>122</b>
6.1	Introduction.....	122
6.2	Numerical model setup .....	126
6.3	Results.....	127
6.3.1	Reference model .....	127
6.3.2	Effects of presence of weak zone and flat-slab subduction .....	131
6.3.3	Weak zone depth and mantle lithosphere strength .....	133
6.3.4	Weak zone locations and widths.....	137
6.3.5	Thickness of continental lithosphere .....	138
6.3.6	Oceanic plate age and convergence rate .....	140
6.4	Discussion and conclusions .....	144
<b>Chapter 7 Conclusion.....</b>		<b>148</b>
7.1	Conclusions.....	149
7.2	Future work.....	153
<b>References .....</b>		<b>156</b>

---

## List of figures

---

Figure 1.1. Schematic cross-sections of (a) a steep-angle subduction zone and (b) a flat-slab subduction zone.....	4
Figure 2.1. General geometry and thermal and mechanical boundary conditions of the numerical models in this thesis.....	16
Figure 3.1. Distribution of flat-slab subduction in North and South America.....	21
Figure 3.2. (a) Initial geometry and boundary conditions of the Farallon subduction models. (b) Initial geotherms of the model. (c) Model geometry at the beginning of Phase 3.....	24
Figure 3.3. Models that investigate the creation of a flat slab: (a) without oceanic plateau; (b) fully eclogitized plateau crust; (c) partially eclogitized plateau crust; (d) non-eclogitized plateau crust; (e) the full width of the model domain for the reference model.....	30
Figure 3.4. Models with initial continental thicknesses of: (a) 60 km, (b) 120 km, (c) 180 km, and (d) 240 km.....	32
Figure 3.5. Models with different CML strengths for a lithosphere thickness of 180 km, corresponding to rheologies of (a) $WO \times 1$ , (b) $WO \times 2$ , (c) $WO \times 30$ , and (d) $WO \times 50$ .....	35
Figure 3.6. Models with a 240 km thick craton located: (a) 600 km, (b) 950 km, and (c) 1300 km from the trench. The craton mantle lithosphere has a reference density	

of 3250 kg/m <sup>3</sup> . (d) Model with a craton 950 km from the trench that has a reference density of 3210 kg/m <sup>3</sup> .....	37
Figure 3.7. Numerical models for strong cratons that are: (a) located at trench with CML of WO x 30 and (b) 600 km from trench with CML of WO x 50. ....	39
Figure 3.8. Contour plots of models with a uniform continental plate: (a) Flat-slab depth and (b) CML thickness displaced by flat slab. ....	41
Figure 3.9. Viscosity and temperature profiles of the CML for a strain rate of 10 <sup>-16</sup> s <sup>-1</sup> . (a) CML with a strength of WO x 10 that has different initial thicknesses. (b) 180 km thick continent with different CML strengths. ....	43
Figure 3.10. Numerical models with a convergence rate of 7 cm/yr: (a) 100 Ma oceanic plate and (b) 30 Ma oceanic plate. ....	46
Figure 3.11. Models with different oceanic plateau crust thicknesses and plateau widths. Model geometry at (a) 6 Myr and (b) 14 Myr. ....	54
Figure 3.12. Full model domain for the model shown in Figure 3.4a. ....	55
Figure 3.13. Model with 60 km continental lithosphere and weak CML rheology (WO x 1).....	56
Figure 3.14. Models containing a weak craton (rheology of WO x 2) located: (a) at the trench, and (b) 600 km from the trench. ....	57
Figure 3.15. Numerical models with different craton mantle lithosphere density: (a) 3250 kg/m <sup>3</sup> and (b) 3210 kg/m <sup>3</sup> .....	58
Figure 3.16. (a) Effective viscosity and velocity field of the reference model. (b) Second invariant of the strain rate of the reference model.....	60
Figure 4.1. (a) The Pampean flat-slab area. (b) Cross section along X-X' profile.	65

Figure 4.2. (a) Initial model geometry and boundary conditions. (b) Initial geotherms for the continental and the oceanic lithosphere. ....	68
Figure 4.3. Reference model evolution with surface elevation. ....	74
Figure 4.4. Thermal evolution of the reference model. (a) Model temperature field. (b) Vertical temperature profile and (c) surface geothermal gradient. (d) Moho temperature and (e) surface heat flow at three positions. ....	77
Figure 4.5. Normal-angle subduction model. (a) Model temperature field. Temporal changes in (b) Moho temperature and (c) surface heat flow of the normal subduction model and flat-slab subduction model. ....	79
Figure 4.6. (a) Temperature fields for models with different continental thicknesses. (b) Geotherm profiles. Temporal changes in (c) Moho temperature and (d) surface heat flow relative to the initial values. ....	81
Figure 4.7. Numerical model results with different thermal conductivities. ....	83
Figure 4.8. (a) Moho temperature of models with different continental crustal thicknesses. (b) Moho temperature of models with different convergence rates. (c) Moho temperature of models with old and young oceanic plates. ....	86
Figure 4.9. 1D time-dependent temperature calculations. (a) Vertical temperature profiles. (b) Surface heat flow and (c) Moho temperature. ....	92
Figure 4.10. Contour plots of (a) Moho temperature and (b) surface heat flow. ....	94
Figure 4.11. (a) Moho temperatures and (b) surface heat flows for a 600°C flat slab at 50 km depth. ....	95
Figure 5.1. (a) Map of the Pampean flat-slab region. (b) Cross section along X-X' .....	105

Figure 5.2. Model evolution with surface elevation. (a) Flat subduction below a continent with no weak zones. (b) Flat subduction with weak zones. (c) Steep-angle subduction with weak zones.....	108
Figure 5.3. (a) Horizontal deviatoric stress field of the model in Figure 5.2b. (b) Theoretical continental yield stress profiles. (c) Model horizontal deviatoric stress profile. (d) Horizontal deviatoric stress field of the steep-angle subduction model in Figure 5.2c.....	110
Figure 5.4. (a) Temporal changes in surface maximum shear strain rate for the continent of the model in Figure 5.2b. (b) Temporal evolution of continental surface elevation of the model in Figure 5.2b.....	112
Figure 5.5. (a) Initial model geometry and boundary conditions. (b) Initial geotherms for the continental and oceanic lithosphere.....	115
Figure 5.6. Evolution of the model shown in Figure 5.2 with the full model domain.....	119
Figure 5.7. Model geometry and surface maximum shear strain rate of models with different weak zone depths.....	120
Figure 5.8. Surface maximum shear strain of model in Figure 5.2c.....	120
Figure 6.1. Shallow and flat subduction in North and South America.....	123
Figure 6.2. a) Initial model geometry and boundary conditions. b) Initial geotherms for the continental and oceanic plates.....	127
Figure 6.3. Reference model evolution and maximum shear stress.....	130

Figure 6.4. (a) Strain rate at the surface for the reference model. (b) Surface elevation for a model with flat-slab subduction below a continent with no weak zones. (c) Horizontal shortening of the weak zone of the reference model.....	131
Figure 6.5. Model geometry for (a) steep-angle subduction with continental weak zone, (b) a flat-slab subduction without the weak zone, and (c) flat-slab subduction with the weak zone. (d) Comparison of the shortening for the three models.....	133
Figure 6.6. (a) Model geometry for a model with a weak zone in the upper crust only and the reference model with weak zone through the whole continental crust. (b) Comparison of weak zone shortening. ....	134
Figure 6.7. Model evolution for models with various continental mantle lithosphere strengths.....	136
Figure 6.8. Model geometry for models with different weak zone locations.....	138
Figure 6.9. (a) Model geometry for models with different initial continental thicknesses. (b) Initial geotherms. (c) Effective viscosity of the weak zone. ....	140
Figure 6.10. Model geometry and surface elevation for models with different oceanic plate ages and convergence rates.....	141
Figure 6.11. Maximum shear stress for the model in Figure 6.10a.....	143
Figure 7.1. Summary of the key findings in this thesis. ....	152
Figure 7.2. Flat-slab subduction in 3D. ....	154

---

## List of tables

---

Table 3.1. Material properties and model parameters .....	26
Table 3.2. Subduction numerical models to examine flat-slab development using an old oceanic plate (100 Ma).....	52
Table 3.3. Numerical models to examine flat-slab depth. Craton location indicates the distance between trench and left boundary of the craton. ....	52
Table 4.1. Model parameters. ....	72
Table 4.2. List of models and the change in Moho temperature and surface heat flow. ....	88
Table 5.1. Model parameters .....	121

---

# Chapter 1 Introduction

---

## 1.1 Subduction zones

Subduction zones are the largest recycling system of the Earth and are the main driving force for plate tectonics and mantle convection (e.g. Davies and Richards, 1992; Stern, 2002). Oceanic lithosphere is generated at a mid-ocean ridge (MOR), and as it moves away from the MOR, the lithosphere cools, thickens, and becomes denser. At an ocean-continent subduction zone, the oceanic plate converges with the continental plate, with the cooler and denser oceanic plate descending into the mantle. Subduction is driven by the negative buoyancy of the down-going oceanic plate as the cold oceanic lithospheric rocks are denser than the surrounding mantle rocks; this results in a steep descending angle slab at most subduction zones (e.g., Turcotte and Schubert, 2002; Hayes et al., 2012). Part of the descending slab may get recycled in the upper mantle (e.g., through slab dehydration, and slab melting), while the rest of the slab penetrates the mantle transition zone (410-660 km deep) and may sink to the core-mantle boundary, where it may be reheated and ascend as a mantle plume after billions of years (Hofmann, 1997).

Subduction zones as active convergent plate margins that play an important role in mantle and lithosphere processes. Earth's most powerful and devastating earthquakes, large volcanoes, mountain building, and large-scale deformation are caused by subduction processes. Subduction zones are the sites of many large and deep earthquakes (Fig. 1.1). The subducting plate is thrust under the overlying plate along the megathrust fault (e.g. Meier et al., 2017; Bilek and Lay, 2018). However, friction along the thrust fault causes

the two plates to lock together and stress builds up with continued plate convergence. The fault ruptures when the stress exceeds the fault strength, triggering a megathrust earthquake. The magnitude of megathrust earthquakes can exceed 9.0, and these earthquakes may trigger tsunamis (Meier et al., 2017). Earthquakes also occur within the subducting oceanic plate. As the oceanic lithosphere descends into the mantle, plate bending and extension cause slip-on faults within the oceanic lithosphere (e.g. Bevis, 1986). In addition, metamorphic phase changes may also affect stresses, causing earthquakes (e.g., Kirby et al, 1996). As a result, earthquakes may occur within the interior of the cold subducted plate to depths of ~660 km; these define the Wadati-Benioff zone (Turcotte and Schubert, 2002; Stern, 2002).

Volcanism is also associated with subduction zones. Volcanic arcs are lines of volcanism that occur approximately parallel to the trench at a distance of about 100 to 120 km above the subducting plate (Tatsumi and Eggins, 1995). The cause of arc volcanism is widely believed to be slab dehydration-related partial melting. The subducting plate carries a large amount of fluids into the subduction zone. These fluids may be present in several forms, including free water in the subducted sediments and oceanic crust pores, as well as water that is bound in minerals that make up the crust and shallow lithospheric mantle (e.g. van Keken et al., 2011). As the subducting plate descends, hydrous fluids are released in the overlying material. The magmas that make up the volcanic arc in most places are derived from melting of the mantle above the subducting plate (i.e., the mantle wedge). Corner flow in the mantle wedge is driven by the down-going slab (Batchelor, 1967), and brings hot mantle into the wedge. As fluids released from the slab enter the mantle wedge, the melting temperature is reduced, and this leads to partial melting of this material at

temperatures of  $\sim 1000^{\circ}\text{C}$  (e.g. Schmidt and Poli, 1998; Mibe et al., 2011). The partially melted mantle material is buoyant enough to ascend and may undergo additional melting due to the reduction in pressure (Turcotte and Schubert, 2002). The formation of most ore deposits and continental crust occurs due to arc volcanism (e.g. Stern, 2002).

Subduction can also induce deformation of the upper plate. The strain regime is divided into 7 classes in the arc and back-arc regions, ranging from strong extension to strong compression (Jarrard, 1986). Subducting slab angle plays an important role in upper plate deformation, with the higher compressional force for a shallow-angle slab (Jarrard, 1986). The upper plate deformation is also depends on the direction of motion of the upper plate and absolute motion of the trench (e.g. Heuret and Lallemand, 2005). Extensional back-arcs are associated with rifting and seafloor spreading (e.g. Mariana subduction zone) and compressional back-arcs experience shortening and retroarc foreland basins with fold-and-thrust belts (e.g. the Andean system) (e.g. Stern, 2002).

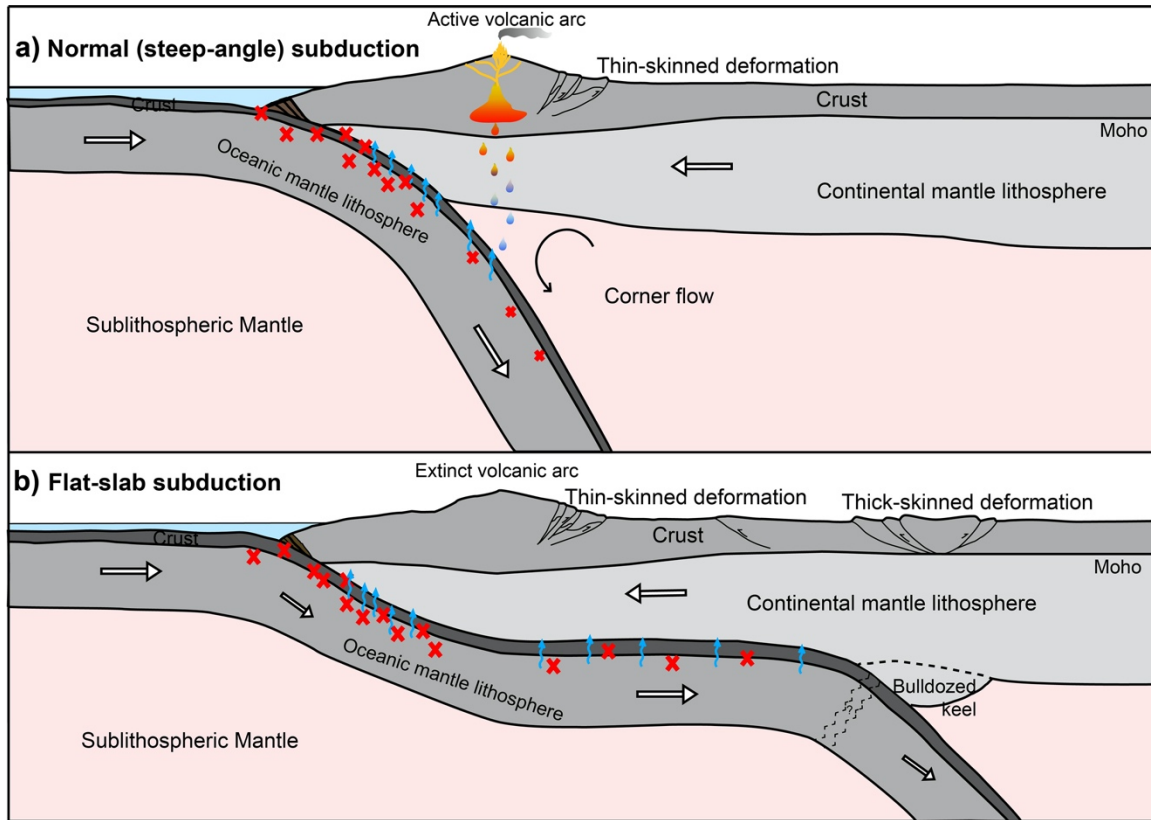


Figure 1.1. Schematic cross-sections of (a) a steep-angle subduction zone and (b) a flat-slab subduction zone. The red crosses show earthquake locations. The blue arrows indicate the slab dehydration process. White arrows show the directions of plate motions relative to the deeper mantle.

## 1.2 Flat-slab subduction

The shape of the subducting plate affects the location and magnitude of earthquakes, volcanic arcs, and deformation patterns (e.g. Jarrard, 1986). A special type of subduction is flat-slab subduction, which is observed in approximately 10% of modern subduction zones (Gutscher et al., 2000a). Modern flat slabs are found in areas where an oceanic plate subducts horizontally below a continental plate. In these places, the oceanic plate bends downward to enter the trench and then unbends to become sub-horizontal, underplating the continental plate for several hundred to thousand kilometers inboard of the plate margin at

depths of ~45 to ~150 km (Fig. 1.1b). The horizontal portion of the subducting plate is in contact with the continental mantle lithosphere (CML) which is referred to as a flat slab. Modern flat slabs can be recognized through a sub-horizontal distribution of Wadati-Benioff earthquakes and the presence of a flat-lying segment of oceanic lithosphere in the shallow mantle from seismic and other geophysical imaging methods (e.g., Gutscher et al., 2000b). Flat slabs are observed at present-day and have been inferred to have existed in the past. Three regions with flat slabs today are in central Mexico, Peru, and central Chile, and areas of shallow-angle subductions are observed in Alaska and Colombia (e.g. Ramos and Folguera, 2009; Manea et al., 2017). Flat slabs have also been inferred to have existed in the western United States (US) in the late Cretaceous, the central Andes from the Late Paleogene to early Neogene, and South China in the Mesozoic (Usui et al., 2003; Li and Li, 2007; Ramos and Folguera, 2009).

The development of flat slab generally causes the termination of arc magmatism (McGeary et al., 1985), as well as the generation of high stresses in the interior of the upper plate that may cause inboard deformation, and changes in mantle wedge flow patterns that may lead to topography changes (e.g., Coney and Reynolds, 1977; Dickenson and Snyder, 1978; G erault et al., 2015; Cramer et al., 2017; Axen et al., 2018). These characteristics may allow ancient flat slabs to be identified in the geological record. With the development of a flat slab, the hot asthenosphere wedge is displaced by the incoming slab. The closure of mantle wedge leads to the cessation of arc volcanism (Coney and Reynolds, 1977; Humphreys et al., 2003). As the tip of the flat slab moves landwards, the new mantle wedge also moves landwards, which may lead to a landward shift in the location of magmatism. The development of a flat slab may also remove the bottom of the continental mantle

lithosphere, causing it to accumulate as a keel at the leading edge of the flat slab (Axen et al., 2018). This could lead to cessation of the arc magmatism if it fully displaces the high-temperature mantle. The formation of a flat slab is also linked to increased compressional stresses in the overriding continental lithosphere (e.g. Dickinson and Snyder, 1978; Bird 1988). Flat slab subduction has been linked with basement-cored block uplifts in the foreland region, such as the Laramide Orogeny in the western US and the Sierras Pampeanas in South America (e.g. Bird, 1988; Jordan and Allmendinger, 1986).

The mechanisms that cause the formation of a flat slab are complex and might involve multiple factors (e.g. van Hunen et al., 2000, 2002, 2004; Manea et al., 2012; Skinner and Clayton, 2013; Liu and Currie, 2016). In general, the subducting slab geometry is controlled by the combined effects of the structures of subducting and overriding plates and dynamical pressure in the mantle wedge (Stevenson and Turner, 1977). Geodynamic studies show that flat-slab subduction is associated with three main factors: a buoyant subducting plate, a high slab suction force, and a high overriding plate velocity (e.g. van Hunen et al., 2000, 2002).

Slab flattening appears to be more likely for regions with a relatively buoyant oceanic plate, due to a young plate age (e.g., Skinner and Clayton, 2011) or the presence of an aseismic ridge where there is a thicker layer of low-density oceanic crust (i.e., oceanic plateau) (e.g., Livaccari et al., 1981; van Hunen et al., 2002; Liu and Currie, 2016). When the density of the subducting plate is lower than the surrounding mantle, the force causing the slab to descend into the mantle is removed. However, subduction of an aseismic ridge (i.e., oceanic plateau) is not always associated with the formation of a flat slab (e.g. Gerya et al., 2009; Skinner and Clayton, 2013), possibly because the plateau is relatively small

and therefore the high density of the surrounding oceanic plate continues to cause the slab to sink. In order for slab flattening to occur, the oceanic plateau must be large enough to exert a buoyant force and this may require that the basaltic crust remains metastable so that the phase change from basalt to high-density eclogite is inhibited (e.g van Hunen et al., 2002; Espurt et al., 2008; Arrial and Billen, 2013).

The descent of an oceanic plate into the mantle induces flow in the overlying mantle wedge; this causes low dynamic pressures above the slab that has the tendency to lift the slab up and can affect the subduction angle (Stevenson and Turner, 1977; Tovish et al., 1978). The magnitude of corner flow is affected by the subducting velocity and mantle corner viscosity (Hager and O'Connell, 1978). A lower wedge viscosity results in higher suction force (e.g., Manea and Gurnis, 2007; Manea et al., 2012). Additionally, the presence of a thick cratonic root in the upper plate will also increase the suction force, especially with a high trenchward motion of the craton (e.g., O'Driscoll et al., 2009; Rodriguez-Fernandez et al., 2012; Manea et al., 2012; Taramón et al., 2015).

Trenchward motion of the upper plate appears to be a critical requirement for the formation of a flat slab. When the upper plate overrides the subducting plate at a rate greater than slab rollback, there can be a decrease in the dip angle of the slab (e.g., Vlaar, 1983; van Hunen et al., 2000, 2004; Espurt et al., 2008; Schepers et al. 2017). The higher overriding velocity also increases the scale of corner flow that creates a lower mantle wedge pressure that tends to lift the slab.

### **1.3 Research objectives**

Research on flat-slab subduction has been conducted for decades, and recent studies have made significant progress in imaging the subducting plate and understanding how a

flat slab develops (e.g. van Hunen et al., 2004; Kim et al., 2012; Liu and Currie, 2016; Scire et al., 2016; Portner et al., 2017). However, there are many fundamental processes associated with flat slabs that are still not well understood. My Ph.D. research focuses on subduction dynamics, especially flat-slab subduction, with emphasis on some of the poorly understood topics, such as the controls on flat-slab geometry and the continental lithosphere response to the development of a flat slab. To study flat-slab subduction dynamics, I use two-dimensional (2D) numerical geodynamic models that provide quantitative information about the subsurface flat slab evolution and the associated surface responses. The fundamental questions to be addressed in this thesis are:

(1) what are the mechanisms that lead to the development of a flat slab and what are the factors that affect the depth at which a flat slab forms?

(2) why is the surface heat flow above a flat slab lower than that of regions with normal angle subduction; does the emplacement of a cool oceanic plate below the continental lithosphere refrigerate the continental lithosphere and over what timescale does the flat slab cool the continent?

(3) how does the development of a flat slab trigger continental deformation; what are the causes of thick-skinned deformation in the continental interior, as seen in the Sierras Pampeanas in South America and the Laramide Orogeny in the western United States?

#### **1.4 Thesis outline**

To address the above questions, this dissertation is organized as follows:

Chapter 2 provides a description of the numerical modelling method used in this research. It summarizes the governing equations, material properties, boundary conditions and modelling phases.

Chapter 3 investigates mechanisms that affect the development of a flat slab and the factors that control the depth at which a flat slab forms. This includes systematic numerical modelling tests to examine the effects of the structure of the overriding continental plate, oceanic plate age, and plate convergence rate on the slab dynamics.

Chapter 4 examines the cooling effect of a flat slab on the overlying continental lithosphere. The timescale of continental cooling is calculated and this chapter provides explanations for why the observed surface heat flow in flat-slab regions is lower than that of normal-angle subduction regions.

Chapter 5 presents models that examine Pampean flat-slab subduction in South America. The causes of the thick-skinned deformation in the Sierras Pampeanas, which is inboard of the Pampean subduction zone, are analyzed.

Chapter 6 expands the study in Chapter 5 to a broader perspective of inboard crustal deformation. Systematic model tests examine the role of a number of factors, including pre-existing weak zone properties (weak zone length and strength) within the continental plate, convergence rate, and the age of oceanic plate. These models provide insights into the origin of large-scale deformation within the continental interior.

Chapter 7 summarizes the main findings of this research, the significance of this work, and the broader impact of the results. It also outlines potential future research directions and possible research projects.

---

## Chapter 2 Numerical modelling method

---

The two-dimensional (2D) numerical models in this study use the finite-element computer code SOPALE (Fullsack, 1995). This code uses the arbitrary Eulerian-Lagrangian (ALE) formulation to calculate viscous-plastic creeping flows in the upper mantle domain, including a free surface and deformation within the domain. The ALE formulation combines the two classical descriptions of motion, Lagrangian (L) and Eulerian (E) formulations, and it uses regriding algorithm to couple the L motions with the E field calculation (Fullsack, 1995; Hirt et al., 1974). The SOPALE has been widely used to study the thermal-mechanical behaviour of the lithosphere and upper mantle on geological timescales (e.g., Fullsack, 1995; Beaumont et al., 2006; Currie and Beaumont, 2011). In this study, we use the 2D thermal-mechanical models to study flat-slab subduction dynamics.

In this chapter, the general methods used in SOPALE are described, including the governing equations, material properties, boundary conditions, and model phases. Model parameters vary between each study. Therefore, the detailed parameters will be given in each subsequent chapter.

### 2.1 Governing equations

The models in this study represent a two-dimensional vertical cross-section along the direction of subduction. The 2D SOPALE code assumes plane strain, with no deformation perpendicular to the model plane. The upper mantle is considered as an incompressible fluid and inertial forces had been neglected (Reynolds number=0) (Fullsack,

1995). These assumptions allow for the simplification of numerical models, such that volume does not change with pressure and temperature; these are common assumptions for models in which materials undergo highly viscous flow (Gerya, 2019). Therefore, the deformation of the system is controlled by the simplified equations of conservation of mass, momentum and energy.

The equation of conservation of mass for an incompressible material is:

$$\frac{\partial v_j}{\partial x_j} = 0 \quad (2.1)$$

and the conservation of momentum is described as:

$$\frac{\partial \sigma_{ij}}{\partial x_j} + \rho g = 0; \quad i, j = 1, 2 \quad (2.2)$$

where  $v$  and  $x$  are vectors for the velocity and spatial coordinates,  $\sigma_{ij}$  is the component of the Cauchy stress tensor,  $\rho$  is the density of the material and  $g$  is the acceleration due to gravity. The stress tensor associated with deformation is:

$$\sigma_{ij} = -P\delta_{ij} + 2\eta_{eff}\dot{\epsilon}_{ij}, \quad (2.3)$$

in which

$$\dot{\epsilon}_{ij} = \frac{1}{2} \left( \frac{\partial v_i}{\partial x_j} + \frac{\partial v_j}{\partial x_i} \right), \quad (2.4)$$

where  $P$  is pressure ( $P = -(\sigma_{11} + \sigma_{22} + \sigma_{33})/3$ ),  $\delta_{ij}$  is the Kronecker delta (1 for  $i=j$ ; 0 otherwise),  $\eta_{eff}$  is the effective viscosity and  $\dot{\epsilon}_{ij}$  is the component of the strain rate tensor.

The energy balance equation used to calculate the thermal evolution is described by:

$$\rho c_p \left( \frac{\partial T_K}{\partial t} + v_i \frac{\partial T_K}{\partial x_i} \right) = k \frac{\partial}{\partial x_i} \frac{\partial T_K}{\partial x_i} + A + \sigma'_{ij} \dot{\epsilon}_{ij} + v_2 \alpha g T_K \rho, \quad (2.5)$$

where  $c_p$  is the specific heat,  $T_K$  is absolute temperature,  $t$  is time,  $k$  is thermal conductivity,  $A$  is radiogenic heat production per unit volume,  $\alpha$  is volumetric thermal expansion coefficient, and  $v_2$  is the vertical velocity. On the left side of Equation 2.5 is time dependent temperature ( $\frac{\partial T_K}{\partial t}$ ) and the advection term due to velocity ( $v_i \frac{\partial T_K}{\partial x_i}$ ). The first two terms on the right side of Equation 2.5 are heat conduction and heat production due to radioactivity of the materials. The last two terms on the right-hand side are the strain heating which accounts for conversion of mechanical energy to heat and correction of temperature for adiabatic heating due to vertical velocity (Currie and Beaumont, 2011).

The above equations are solved to determine the coupled thermal-mechanical evolution of the system. The mechanical and thermal fields are coupled through the temperature-dependent density and viscous rheology of model materials, and inclusion of strain heating and adiabatic heating (e.g. Beaumont et al., 2006; Currie and Beaumont, 2011). In addition, material flow leads to the redistribution of the materials that have heat production (Currie and Beaumont, 2011).

The governing equations are solved based on the given boundary conditions using the SOPALE code (Fullsack, 1995). In the ALE formulation, these calculations are carried out on the Eulerian mesh with a fixed horizontal node spacing. The vertical spacing of the nodes varies with depth, in order to allow a higher resolution in the lithosphere. In addition, the model has a free surface, and the mesh can stretch vertically to allow topography to develop. The thermal and mechanical properties are assigned on the Eulerian mesh and then interpolated onto the Lagrangian mesh which acts as tracer particles (Fullsack, 1995). After the equations are solved on the Eulerian mesh, the incremental displacement of each Lagrangian particle is calculated by multiplying the velocity by the time step length. This

advects and redistributes the Lagrangian particles. These particles carry the material properties (e.g. density, rheology, pressure, and temperature) to the new location, and then the Eulerian mesh is updated at the beginning of the next step. The same processes is repeated for the next time interval. Through this approach, the ALE method allows for large-scale deformation to be modelled in a short computational time. Therefore, it is suitable for my research that examines the upper mantle scale subduction zone processes.

## 2.2 Material properties

In the models, all materials have a viscous-plastic rheology. Frictional-plastic deformation is determined by the Drucker-Prager yield criterion:

$$J'_2 = P \sin \phi_{eff} + C_0 \cos \phi_{eff}, \quad (2.6)$$

in which

$$J'_2{}^2 = \frac{1}{2} \sigma'_{ij} \sigma'_{ij}, \quad (2.7)$$

$$\sin(\phi_{eff}) = (1 - \lambda) \sin \phi, \quad (2.8)$$

where  $J'_2$  is the square root of the second invariant of the deviatoric stress tensor,  $P$  is pressure,  $\phi_{eff}$  is the effective internal angle of friction that depends on pore fluid pressure ratio ( $\lambda$ ) and the dry internal angle of friction ( $\phi$ ) through Equation 2.8, and  $C_0$  is cohesion. The cohesion and effective angle of friction may vary with cumulative strain due to pore fluid pressure change, which causes strain softening or strain hardening (e.g. Fullsack, 1995; Beaumont et al., 2006; Huisman and Beaumont, 2003; Warren et al., 2008). In SOPALE, deformation is modelled as viscous creep by defining an effective viscosity for frictional-plastic behaviour that places the state of stress on yield (Fullsack, 1995; Willett, 1999; Beaumont et al., 2006).

Viscous deformation occurs at stresses below frictional-plastic yield, with an effective viscosity of:

$$\eta_{eff} = f(B^*) \dot{\epsilon}'_2^{\frac{1-n}{n}} \exp \left[ \frac{Q+PV^*}{nRT} \right], \quad (2.9)$$

in which

$$\dot{\epsilon}'_2^2 = \frac{1}{2} \dot{\epsilon}_{ij} \dot{\epsilon}_{ij}, \quad (2.10)$$

where  $\dot{\epsilon}'_2$  is the square root of the second invariant of the strain rate tensor,  $f$  is a scaling factor,  $R$  is the gas constant, and  $B^*$ ,  $n$ ,  $Q$  and  $V^*$  are the pre-exponential viscosity parameter, stress exponent, activation energy and activation volume, respectively. For material properties, we use well-constrained rock rheologies with parameters that have been determined through laboratory measurements of rock deformation ( $B^*$ ,  $n$ ,  $Q$  and  $V^*$ ). The scaling factor  $f$  is used to linearly scale the effective viscosity relative to the base values in order to account for variations in composition and water content; this also provides a way to assess the effects of reasonable variations in material rheology due to uncertainties in the laboratory values (e.g. Beaumont et al., 2006; Warren et al., 2008). Strain weakening is included in most of the models through a decrease in the scaling factor  $f$  with cumulative strain, in account for grain size reduction and other factors (Beaumont et al., 2006; Warren et al., 2008).

All the materials in the model have a temperature-dependent density

$$\rho(T) = \rho_0 [1 - \alpha(T - T_0)], \quad (2.11)$$

where  $\rho_0$  is the reference (compositional) density at temperature  $T_0$  and  $\alpha$  is the volumetric thermal expansion coefficient.

### 2.3 Boundary conditions

Figure 2.1 shows the basic subduction model setup, with an oceanic plate on the left-hand side, continental plate on the right-hand side and sublithospheric mantle beneath both plates. During the model run, the top boundary is a stress-free surface that allows vertical movement and development of topography. The bottom boundary is a closed free-slip surface. Velocities are prescribed to the side boundaries to induce plate convergence. Plate velocities are assigned to the oceanic ( $v_0$ ) and continental ( $v_c$ ) lithospheres to model convergence at a total rate of  $v_0 + v_c$ . Below the lithosphere, a small outflux velocity ( $v_b$ ) is assigned to maintain mass balance within the model domain. The outflux  $v_b$  is calculated using:

$$h_0(v_0 + v_c) = (h_l + h_r)v_b, \quad (2.12)$$

where  $h_0$  is the oceanic lithosphere thickness,  $h_l$  and  $h_r$  are the thickness of the outflow region on the bottom left and bottom right boundaries. In between the influx and outflux region, there is 10 km transition region, where the velocities are interpolated linearly. Models are run in the continent reference frame by adding  $-v_c$  to all side boundaries (Fig. 2.1).

The thermal boundary conditions are as follows. The top surface has a fixed temperature of  $0^\circ\text{C}$  and the temperature of the bottom boundary is consistent with an adiabatic mantle with a potential temperature of  $1300^\circ\text{C}$  and vertical gradient of  $0.4^\circ\text{C}/\text{km}$  (Fig. 2.1). For side boundaries where material enters the model domain, a fixed temperature is assigned based on the one-dimensional steady-state conductive heating condition:

$$T(z) = -\frac{A(z)}{2k(z)}z^2 + \frac{q_s}{k(z)}z + T_0, \quad (2.13)$$

where  $z$  is the depth,  $A$  is radiogenic heat production,  $k$  is thermal conductivity,  $q_s$  is surface heat flow, and  $T_0$  is surface temperature. The conductive geotherm is determined based on the continental lithospheric thickness and oceanic lithospheric thickness (depends on oceanic plate age), such that the temperature at the lithosphere-asthenosphere boundary (LAB) is equal to the mantle adiabat. The other parts of the side boundaries have no horizontal heat flux (i.e., insulating conditions).

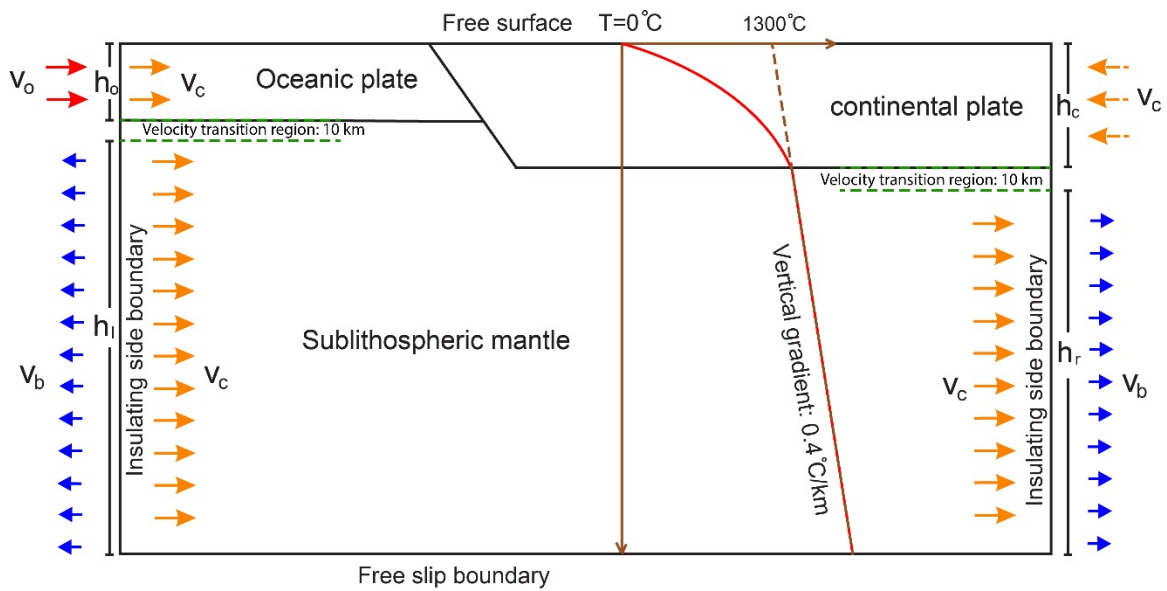


Figure 2.1. General geometry and thermal and mechanical boundary conditions of the numerical models in this thesis.

## 2.4 Modelling phases

The subduction models in my study are run in three model phases. In Phase 1, the initial 2D thermal structure of the model domain is calculated based on the initial geometry, material thermal properties and boundary conditions. The model also undergoes isostatic adjustment where all materials are able to move vertically depending on the densities of

the oceanic plate and the continental plate, in order to create a constant lateral pressure within the sublithospheric mantle. The dense oceanic plate normally subsides by ~4 km relative to the continent. There is no plate convergence in this phase.

In Phase 2, a prescribed convergence velocity of 5 cm/yr is applied to the oceanic side boundary to initiate subduction. Subduction is facilitated with a weak seed at the ocean-continent boundary that has a wet quartzite rheology and mantle density (Fig. 3.2a). The weak seed is subducted with the oceanic plate and does not affect later model evolution. In most of my models, Phase 2 is runs to 500 km convergence (10 million years), and this results in a well-defined steep-angle subduction zone (Fig. 3.2c).

Phase 3 starts from the end of Phase 2 and is the phase in which the numerical model experiments are conducted. The plate velocities are modified to match the real convergence rate for the study area. Different model parameters are tested to investigate their effects on the model dynamics and evolution. In most models, the model time is reported as the time since the start of Phase 3, and the distance is reported as the distance from the trench.

---

## Chapter 3 Influence of upper plate structure on flat-slab depth: Numerical modelling of subduction dynamics

---

### Abstract

Western North and South America have been affected by flat-slab subduction where a segment of the subducting plate becomes horizontal below the overlying continent. Modern observations and constraints on past geometries show that the depth of the flat slab varies from just below the continental Moho to  $>100$  km depth. Thus, in some areas, there is little to no continental mantle lithosphere (CML) above the flat slab, whereas other flat-slab areas are overlain by CML thicknesses  $>50$  km. The mechanisms causing different slab depths are unclear. We examine flat-slab subduction dynamics and slab depth through 2D thermal-mechanical modelling. The models investigate plate structures and velocities similar to those of the Cretaceous western United States and present-day South America. Models show that flat-slab depth is primarily determined by continental structure. A deep flat slab occurs if the continent is initially thick, as its mantle lithosphere is cool and thus too strong to be displaced by the flat slab. The CML rheology plays a secondary role. A weak, hydrated lithosphere is easily displaced, leading to a shallower slab. The flat slab can displace up to 50% of the thickness of the CML, and no model exhibits displacement of the full CML thickness. This suggests that shallow flat slabs below Mexico and Peru require a thin continent prior to slab flattening. The models also show that a flat slab is deflected downward when it encounters thick craton lithosphere, with a larger depth for a

chemically depleted craton. This has implications for modification of the Wyoming craton during Farallon flat-slab subduction.

### **3.1 Introduction**

Subduction is driven by the negative buoyancy of the downgoing oceanic plate, resulting in a steep descent angle into the mantle at most subduction zones (e.g., Hayes et al., 2012). However, in approximately 10% of modern subduction zones, low-angle to flat-slab subduction occurs (Gutscher et al., 2000a). In these places, the oceanic plate bends downward to enter the trench and then unbends to become sub-horizontal underplating the continental plate for several hundred kilometers inboard of the plate margin. Here, we use the term “flat slab” to refer to the horizontal portion of the subducting plate that underlies the continental mantle lithosphere (CML). Modern flat slabs can be recognized through a sub-horizontal distribution of Wadati-Benioff earthquakes and the presence of a flat-lying segment of oceanic lithosphere from seismic and other geophysical imaging methods (e.g., Gutscher et al., 2000b). Flat slabs may also create gaps in arc magmatism, possibly high stresses in the upper plate that may cause deformation inboard of the plate margin, and alter mantle wedge flow patterns that may lead to topography changes (e.g., Coney and Reynolds, 1977; Dickinson and Snyder, 1978; Gérard et al., 2015; Cramer et al., 2017; Axen et al., 2018), allowing ancient flat slabs to be identified in the geological record.

Geodynamic studies show that flat-slab subduction can be induced by several factors. Trenchward motion of the upper plate appears to be a critical requirement, whereby the upper plate overrides the subducting plate at a rate greater than slab rollback (e.g., van Hunen et al., 2004; Schepers et al. 2017). Additionally, flattening appears to be more likely for regions with a relatively buoyant oceanic plate, due to a young plate age (e.g., Skinner

and Clayton, 2011) or the presence of a low-density aseismic ridge (i.e., oceanic plateau) (e.g., Livaccari et al., 1981; van Hunen et al., 2002; Liu and Currie, 2016). Flattening is further aided by low pressures in mantle wedge that create an upward hydrodynamic force on the slab (Stevenson and Turner, 1977), especially in regions with craton in the upper plate (e.g., O'Driscoll et al., 2009; Rodriguez-Fernandez et al., 2012; Manea et al., 2012; Taramón et al., 2015). However, if the mantle wedge viscosity is too high or the craton root is close to trench, slab-flattening is inhibited (e.g., Manea and Gurnis, 2007; Manea et al., 2012).

In western North and South America, several low-angle and flat-slab segments occur at present-day or are postulated to have existed in the past (Fig. 3.1; Gutscher et al., 2000b; Romas and Folguera, 2009). Three well-studied modern flat slabs are found below Mexico, Peru and Chile. These are relatively recent flat slabs, with the onset of slab flattening at 15 to 10 Ma (Manea et al., 2017 and references therein). The current flat-slab segments start 100-200 km from the trench and extend an additional 200-300 km inland (Manea et al., 2017). Intriguingly, the flat segments are observed to be at a range of depths. The top of the flat slab below central Mexico is at ~45 km depth, placing it immediately below the continental Moho (Kim et al., 2012). The Peruvian flat-slab depth is ~50-70 km (Bishop et al., 2017). As the continental crust is relatively thick (~65 km), there is little CML above the flat slab. The Pampean flat slab is the deepest, with its surface at 100-110 km depth (Manea et al., 2017). In this region, the continental crust is ~60 km thick, meaning that there is ~50 km of CML above the flat slab.

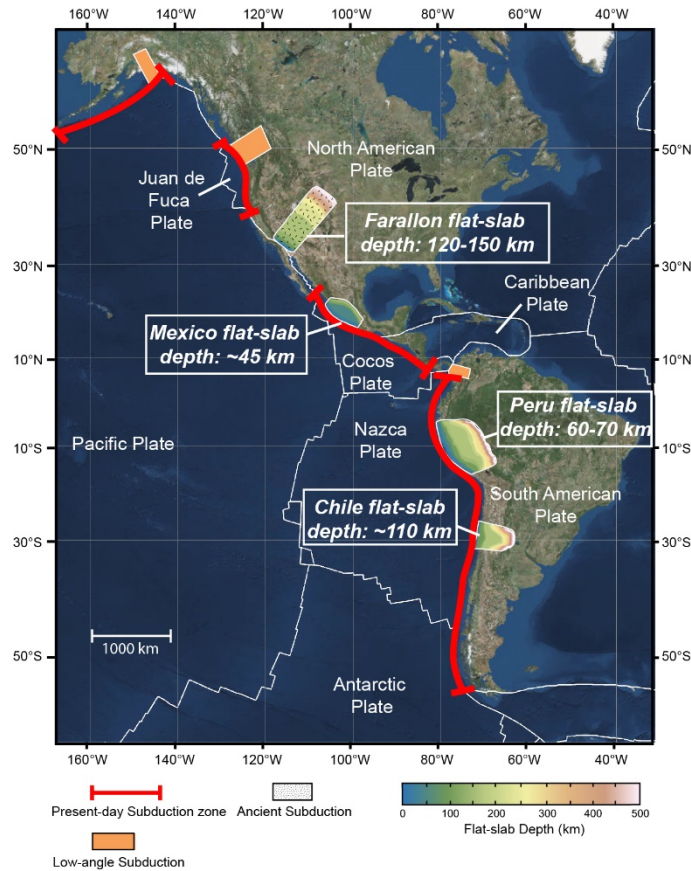


Figure 3.1. Distribution of flat-slab subduction in North and South America. Red solid lines are modern subduction zones. Orange boxes indicate areas with low-angle subduction: South Alaska, Cascadia, and Colombia (north to south). Colored areas show the contours of the top of the oceanic plate (modified from Hayes et al., 2012; Farallon depth from Liu et al., 2008).

An area of past flat-slab subduction is the western United States, where geological evidence suggests that the Farallon Plate developed a flat geometry from the Late Cretaceous to early Paleogene (e.g. Coney and Reynolds, 1977). The flat slab is proposed to have triggered the Laramide orogeny that included basement-involved crustal deformation in the continental interior (Dickinson and Snyder, 1978; Bird, 1988). This has been compared to the modern Sierras Pampeanas deformation above the Pampean flat slab (Jordan and Allmendinger, 1986). Based on the patterns of magmatism, deformation and

topography, the Farallon flat slab is inferred to have had a large inland width, reaching as much as 2000 km from the trench (Copeland et al., 2017). Some evidence for the depth of the top of the flat slab comes from xenolith studies that indicate a depth of 120-150 km (Usui et al., 2003; Liu et al., 2008). The continental crustal thickness is inferred to have been ~30 to ~50 km (Bahadori et al., 2018), which places the flat slab at least 70 km below the continental Moho.

The mechanisms for creating a flat slab in the regions shown in Figure 3.1 have been examined in a number of geodynamic studies using plate reconstructions and/or numerical models (e.g., van Hunen et al., 2002; 2004; Skinner and Clayton, 2011; Manea et al., 2012; Liu and Currie, 2016; Cramer et al., 2017; Schepers et al. 2017). However, these studies do not fully address the observed variability in flat-slab depth. It has been proposed that strong coupling along the top of the flat slab and extensive hydration of the overlying continental plate could lead to the development of a shallow slab owing to removal of CML (Skinner and Clayton, 2011; Bishop et al., 2018). As noted above, only some flat slabs lie just below the continental Moho (e.g., Mexico, Peru); others are found below 100 km depth. In this chapter, we present numerical models to systematically investigate factors that affect the development and the depth of a flat slab, including the structure of the upper plate, oceanic plate age, and plate convergence rate.

## **3.2 Materials and methods**

### **3.2.1 Model geometry**

We use two-dimensional thermal-mechanical models to investigate flat-slab subduction. The models are oriented in the direction of plate convergence, and the model domain is 3000 km wide and 660 km deep (Fig. 3.2). The initial set of models is based on

Farallon Plate subduction below the western United States. The oceanic plate consists of 8 km thick crust, underlain by an 16 km thick harzburgite layer, representing melt-depleted mantle (van Hunen et al., 2004). Below this is the oceanic mantle lithosphere, with a thickness that depends on plate age. Most models use an age >100 Ma, giving a total lithosphere thickness of 90 km, consistent with the Farallon Plate age during the Late Cretaceous (Usui et al., 2003). Later models (Section 3.5.2) use a young (~30 Ma) subducting plate representing the present-day Nazca Plate. Subduction of the Conjugate Shatsky Rise (CSR) oceanic plateau is believed to have triggered the Farallon flat slab (e.g., Liu et al., 2010). Thus, in our models, the oceanic plate contains a 600 km wide oceanic plateau with 18 km thick crust, 36 km harzburgite layer and 36 km mantle lithosphere. The thicker harzburgite layer represents greater partial melting during creation of the plateau crust (e.g. van Hunen et al., 2004). The size of the oceanic plateau is based on the Shatsky Rise plateau offshore Japan (Korenaga and Sager, 2012).

The models have a relatively simple continental structure (Fig. 3.2). We first consider models with no lateral variations. The continent has a 24 km thick upper crust and 12 km thick lower crust overlying mantle lithosphere. The reference model (Fig. 3.4b) has a total lithosphere thickness of 120 km. As described below, we vary the thickness and rheology of the mantle lithosphere to examine the effect on the flat slab. In later models (Section 3.4.3), we add a thick continental craton to the continental interior.

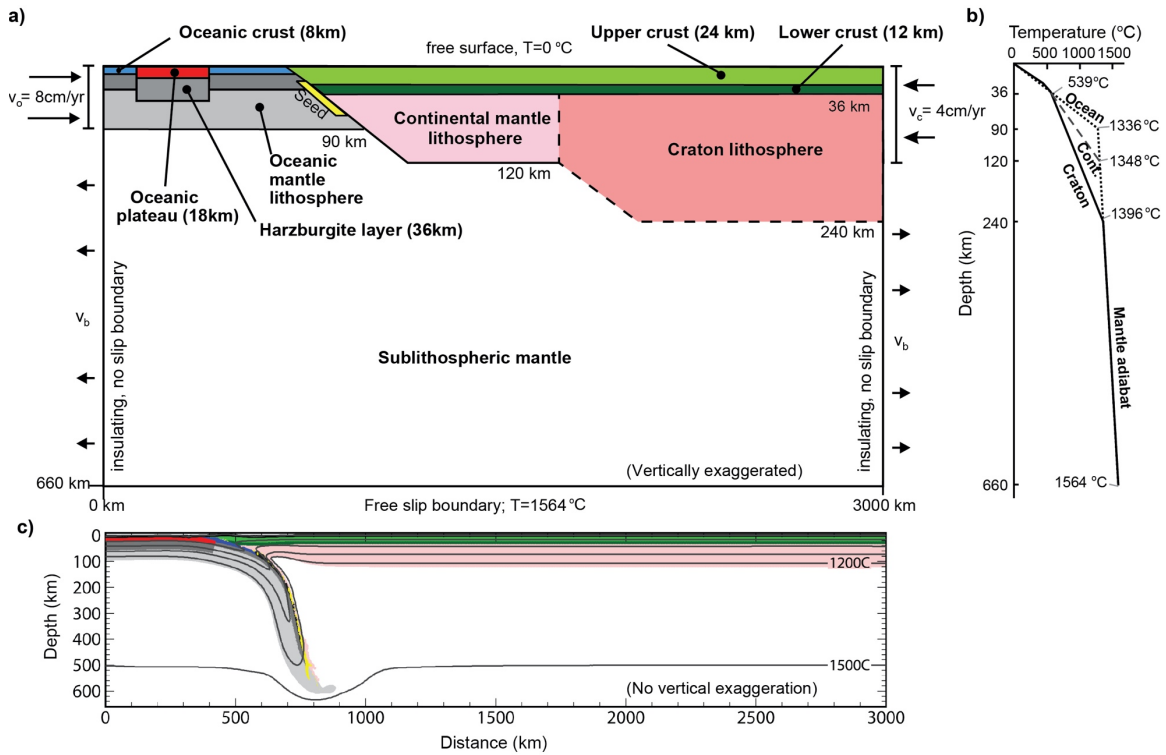


Figure 3.2. (a) Initial geometry and boundary conditions of the Farallon subduction models. The first set of models has a uniformly thick continent (reference 120 km thick lithosphere shown here); later models include a 240 km thick craton lithosphere at varying distances from the trench (dark pink region). (b) The initial geotherms for the oceanic plate, reference continental plate (120 km thick), and craton (240 km thick). (c) Model geometry at the beginning of Phase 3 with material colors as in (a); black lines are isotherms every  $300^\circ\text{C}$ .

### 3.2.2 Material properties

We follow Beaumont et al. (2006) in choosing a base set of laboratory-derived rheology parameters and using the factor  $f$  to linearly scale the effective viscosity relative to the base values. This allows us to test the effects of strength variations associated with minor changes in composition or water content. The continental upper crust has a wet quartzite rheology (Gleason and Tullis, 1995) with  $f=50$ . The oceanic crust and continental lower crust use a dry Maryland diabase rheology (Mackwell et al., 1998) with  $f=0.1$  for

oceanic crust and  $f=1$  for continental lower crust. The high scaling factors for continental crust enable continuous flat-slab subduction with little continental deformation, as our focus is on subducting plate dynamics. The oceanic harzburgite layer and oceanic mantle lithosphere have the rheology of wet olivine (WO) (Karato and Wu, 1993) with  $f=10$ . In the reference model (Fig. 3.4b), the CML has  $f=10$ , approximating relatively dry conditions. Later models test values from  $f=1$  to  $f=50$ , representing conditions from very weak (i.e. hydrated) to very strong (dry) CML.

The thermal and density parameters are given in Table 3.1. The upper and lower continental crusts have radiogenic heat production of 1.0 and 0.4  $\mu\text{W}/\text{m}^3$ , respectively (Jaupart and Mareschal, 2014). There is no heat production for other materials. All materials have a temperature-dependent density. The basaltic oceanic crust undergoes a metamorphic phase change as it reaches temperature and pressure conditions in the eclogite stability field (Hacker et al., 2003). At this point, its density is increased (Warren et al., 2008); no other material properties are changed. For the normal thickness oceanic crust, the density increases by 550  $\text{kg}/\text{m}^3$ , assuming 100% eclogitization (Table 3.1). In section 3.3, we examine variable amounts of eclogitization for the CSR crust.

Table 3.1. Material properties and model parameters

	Oceanic crust	Oceanic mantle lithosphere	Cont. upper crust	Cont. lower crust	Cont. mantle lithosphere	Sub-lithospheric mantle
<b>Plastic rheology</b>						
$C_0$ (MPa)	0	0	20	0	0	0
$\phi_{\text{eff}}^*$	$15^\circ\text{-}2^\circ$	$15^\circ\text{-}15^\circ$	$15^\circ\text{-}2^\circ$	$15^\circ\text{-}2^\circ$	$15^\circ\text{-}2^\circ$	$15^\circ\text{-}2^\circ$
<b>Viscous rheology</b>						
<b>Material</b>	dry Maryland diabase	Wet Olivine	Wet Quartzite	dry Maryland diabase	Wet Olivine	Wet Olivine
$F^\dagger$	0.1-0.01	10-10	50-5	1-0.1	10-1	1-1
$A_{\text{ps}} (\text{Pa}^{-n} \text{s}^{-1})^\S$	$5.78 \times 10^{-27}$	$1.76 \times 10^{-14}$	$8.57 \times 10^{-28}$	$5.78 \times 10^{-27}$	$1.76 \times 10^{-14}$	$1.76 \times 10^{-14}$
$B^* (\text{Pa}^{-n} \text{s}^{-1})^\S$	$1.91 \times 10^5$	$1.92 \times 10^4$	$2.92 \times 10^6$	$1.91 \times 10^5$	$1.92 \times 10^4$	$1.92 \times 10^4$
$n$	4.7	3.0	4.0	4.7	3.0	3.0
$Q$ (kJ mol $^{-1}$ )	485	430	223	485	430	430
$V^*$ (cm $^3$ mol $^{-1}$ )	0	10	0	0	10	10
<b>Thermal parameters</b>						
$k$ (Wm $^{-1}$ K $^{-1}$ ) $^\#$	2.25	2.25	2.25	2.25	2.25	2.25
$A$ ( $\mu\text{Wm}^{-3}$ )	0	0	1.0	0.4	0	0
$c_p$ (J kg $^{-1}$ K $^{-1}$ )	750	1250	750	750	1250	1250
<b>Density<math>^{**}</math></b>						
$\rho_0$ (kg m $^{-3}$ )	2950	3250	2800	2900	3250	3250
$T_0$ (°C)	0	1344	200	500	1344	1344
<b>Eclogite <math>\rho_0</math> (kg m<math>^{-3}</math>)</b>	3500	—	—	—	—	—
<b>Eclogite <math>T_0</math> (°C)</b>	0	—	—	—	—	—
$\alpha$ (K $^{-1}$ )	$3.0 \times 10^{-5}$	$3.0 \times 10^{-5}$	$3.0 \times 10^{-5}$	$3.0 \times 10^{-5}$	$3.0 \times 10^{-5}$	$3.0 \times 10^{-5}$
* Softens through a decrease in $\phi_{\text{eff}}$ over accumulated strain of 0.5 to 1.5 (Beaumont et al., 2006).						
† Weakens through a decrease in $f$ over accumulated strain of 2.0 to 5.0 (Warren et al., 2008).						
§ $B^* = \frac{1}{2} A_{\text{ps}}^{-1/n}$ . $A_{\text{ps}}$ is the plane strain pre-exponential factor that converted from uniaxial laboratory experimented pre-exponential viscosity parameter ( $A_{\text{uni}}$ ). $A_{\text{ps}} = \frac{1}{2} (3^{(n+1)/2}) A_{\text{uni}}$ .						
# Thermal conductivity at temperatures less than 1396°C; above this, thermal conductivity increases linearly to 54.25 Wm $^{-1}$ K $^{-1}$ at 1436°C (Pysklywec and Beaumont, 2004).						
** Temperature dependent density: $\rho(T) = \rho_0 [1 - \alpha(T - T_0)]$ , where $\rho_0$ is the reference (compositional) density at temperature $T_0$ and $\alpha$ is the volumetric thermal expansion coefficient.						

### 3.2.3 Boundary conditions

Figure 3.2 shows the model boundary conditions. The top boundary is a stress-free surface, the bottom boundary is a closed free-slip surface, and the no-slip side boundaries have prescribed horizontal velocities to induce plate convergence. The top surface is 0°C and the bottom boundary is 1564°C, consistent with an adiabatic mantle with a potential temperature of 1300°C (Fig. 3.2b). The side boundaries have no horizontal heat flux, except on the oceanic lithosphere boundary where a geotherm is prescribed based on plate age (Fig. 3.2b).

### 3.2.4 Modelling phases

Models are run in three phases as described in Chapter 2 (section 2.4). The numerical model experiments (Phase 3) start from this point. At this time, the plate velocities are modified. The first set of models use the average Farallon and North America plate velocities at 90-60 Ma ( $V_o=8$  cm/yr;  $V_c=4$  cm/yr; Torsvik et al., 2008), giving a convergence rate of 12 cm/yr. Lower rates are investigated in Section 3.5.2. Models are run for 30 Myr in this phase, and model times are reported relative to the start of Phase 3, i.e., the elapsed time since initiation of oceanic plateau subduction. A full list of models is given in Tables 3.2 and 3.3.

### 3.2.5 Flat-slab depth

Flat-slab depth is defined as the depth from the surface of the continent to the boundary between CML and the flat portion of the oceanic plate. To compare the models, we report the flat-slab depth at 800 km from the trench at 14 Myr for models without a craton. For craton models, we measure the flat-slab depth in the craton area at 1400 km

from the trench at 18 Myr so that the slab is located below the craton. After the development of the flat slab, its depth does not vary significantly with time.

### **3.3 Factors affecting the creation of a flat slab**

We first present models to demonstrate the formation of a flat slab for an old oceanic plate (>100 Ma), using the reference geometry (i.e., 120 km thick continent; parameters in Table 3.1). These models have trenchward motion of the continent ( $V_c=4$  cm/yr), which has been shown to be essential for creation of a flat slab (e.g. van Hunen et al., 2000, 2004; Liu and Currie, 2016).

Figure 3.3a shows a model with a uniform oceanic plate (no oceanic plateau). After subduction initiation, the oceanic plate continues subducting at a relatively steep angle ( $\sim 40^\circ$  at 100-200 km depth). Figure 3.3b shows a model with an oceanic plateau (the CSR), where both the normal oceanic crust and plateau crust undergo a transformation to high-density eclogite at the appropriate pressure-temperature conditions. With the oceanic plateau, the slab geometry is somewhat shallower ( $\sim 30^\circ$  dip) compared to the model with no plateau, due to a decrease in angle as the buoyant plateau first enters the trench and the low-density harzburgite layer. However, there is no propensity for the slab to flatten immediately below the continent.

The next two models consider reduced eclogitization of the oceanic plateau crust, motivated by observations that basalt can remain metastable, especially under dry conditions (e.g. Austrheim et al., 1991). This may be the case near an oceanic plateau, as the large degree of partial melting during plateau formation may dehydrate the underlying mantle (Arrial and Billen, 2013 and references therein).

Figures 3.3d and 3.3e shows the end-member case in which there is no oceanic plateau eclogitization (i.e. no density change). As the plateau subducts, it remains buoyant, resulting in a break-off at the leading edge of the plateau at  $\sim 5$  Myr (Fig. 3.4b). The removal of the dense frontal slab and the presence of the buoyant plateau enable a flat-slab geometry to develop (e.g. Liu and Currie, 2016). As the oceanic plateau migrates inland, it displaces the lower 20-25 km CML. The displaced CML fills the mantle wedge in front of the flat slab (Axen et al., 2018). We refer to this model as the reference model. Fig. 3.3c shows a model with  $\sim 30\%$  eclogitization (density increase of  $170 \text{ kg/m}^3$ ). This model also undergoes a break-off of the dense frontal slab, leading to the development of the flat slab. To find the threshold buoyancy for creating a flat slab, additional tests were done and show that a 18 km thick oceanic plateau with  $>50\%$  plateau eclogitization (density increase of  $>270 \text{ kg/m}^3$ ) does not develop a flat geometry.

From this, we conclude that creation of a flat slab requires that the oceanic plateau undergoes only minimal eclogitization, consistent with the results of Arrial and Billen (2013). For both 0% and 30% plateau eclogitization, the flat slabs have a depth of  $\sim 95$ -100 km at 800 km from the trench at 14 Myr, indicating that the slab depth is not strongly affected by the density, as long as the plateau remains buoyant enough to trigger flattening (Figs. 3.3c and 3.3d). We have also tested the effects of other oceanic plateau properties, e.g. plateau width and crustal thickness. Figure 3.11 shows that the oceanic plateau must be  $>200$  km wide and the plateau crust must be  $>10$  km thick to be buoyant enough to develop a flat slab for the conditions in our models. Once a flat slab develops, it has a depth of 95-100 km (Fig. 3.11). In summary, our models show that the oceanic plateau properties

affect the buoyancy of the subducting plate and thus determine whether a flat slab can develop, but there is minimal effect on the flat-slab depth.

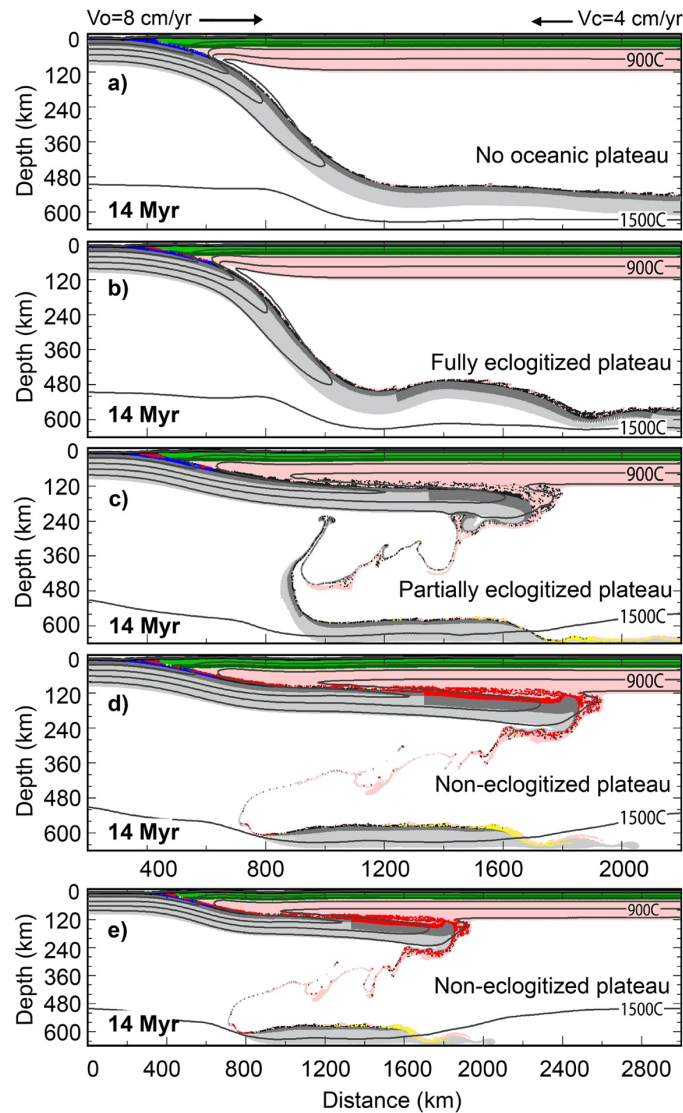


Figure 3.3. Models that investigate the creation of a flat slab, showing the geometry at 14 Myr: (a) without oceanic plateau; (b) fully eclogitized plateau crust ( $3450 \text{ kg/m}^3$ ); (c) partially eclogitized (30%;  $3075 \text{ kg/m}^3$ ) plateau crust; (d) non-eclogitized (metastable) plateau crust (reference model;  $2950 \text{ kg/m}^3$ ); (e) the full width of the model domain for the reference model. Material colors as in Figure 3.2a; black lines are isotherms every  $300^\circ\text{C}$ .

### 3.4 Effect of continental mantle lithosphere on flat-slab depth

This section investigates how variations in continental lithosphere properties affect flat-slab depth. The models are based on the reference model, using a non-eclogitized (metastable) oceanic plateau crust (Fig. 3.3d). We examine variations in lithosphere thickness, lithosphere rheology and the presence of a thick continental craton.

#### 3.4.1 Continental lithosphere thickness

The thickness of continental lithosphere is dependent on its age and the surrounding mantle processes. Continental lithosphere thickens through thermal cooling and accretion of the depleted mantle materials (e.g. Oxburgh and Parmentier, 1978). It can be thinned through gravitational instability and slab truncation (e.g. Krystopowicz and Currie, 2013; Humphreys et al., 2015). Continental lithosphere thickness varies from <60 km in tectonically active areas (e.g. North American Cordillera, East African Rift) to >200 km in cratons (e.g., Artemieva and Mooney, 2001; Pasyanos et al., 2014).

Here, we test different continental thicknesses (60, 120, 180, and 240 km), keeping all other parameters the same. To ensure compatibility between lithosphere thickness and thermal structure, in Phase 1, we use thermal conductivities of 0.66, 3.75, and 5.16 W/(m·K) for the CML of models with continent thicknesses of 60, 180, and 240 km, respectively. This ensures that the conductive lithosphere geotherm intersects the mantle adiabat at the CML base. In Phases 2 and 3, the CML thermal conductivity is set to the standard value (Table 3.1). Figure 3.4b is the reference model with a 120 km. As discussed above, the flat slab develops following a slab-break off after the buoyant plateau enters the subduction zone, and the flat slab is at 95-100 km depth at 14 Myr.

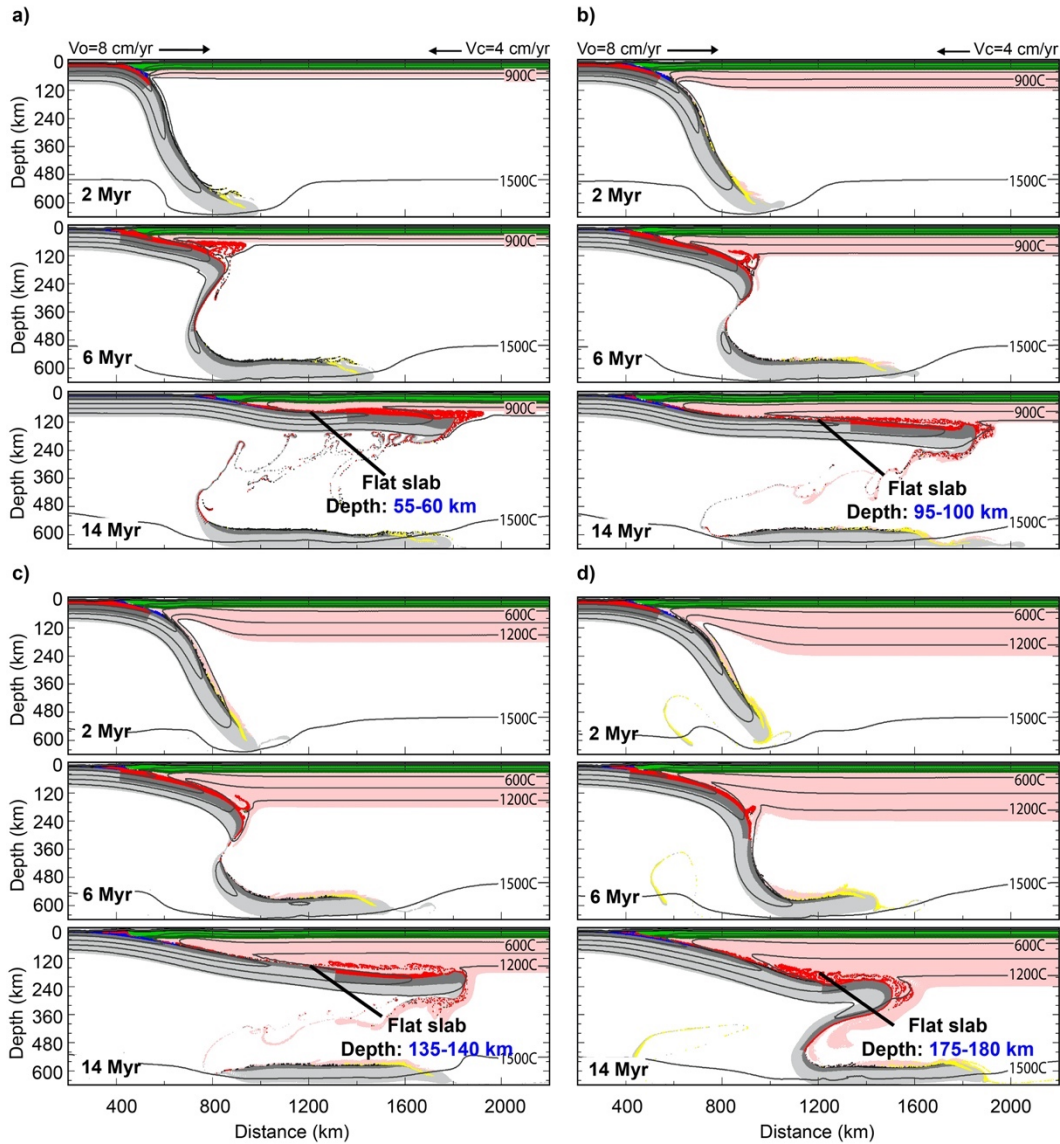


Figure 3.4. Models with initial continental thicknesses of: (a) 60 km, (b) 120 km, (c) 180 km, and (d) 240 km. The strength of the continental mantle lithosphere is  $WO \times 10$ . Material colors as in Fig. 3.2a; black lines are isotherms every  $300^{\circ}\text{C}$ .

Figure 3.4a shows a model in which the continental lithosphere thickness is 60 km. As in the reference model, the slab undergoes a break-off and a flat slab develops. The top of the flat slab is at 55-60 km depth at 14 Myr and thus has displaced only a small thickness of CML. There is some inland migration of the trench in the later stages, as the crust near

the landward boundary of the model undergoes failure (Fig. 3.12). In Figure 3.4c, the model has a 180 km thick continental lithosphere. It follows a similar evolution, creating a flat slab at 140-150 km depth. The flat slab displaces and mixes with the lower 40-50 km of CML. In Figure 3.4d, the continental lithosphere thickness is 240 km. This model does not have a complete slab break-off because the thicker CML causes the oceanic plate to descend at a relatively steep geometry, such that the dense material ahead of the plateau does not sink at a significantly faster rate; its descent is also hindered as it reaches the closed bottom boundary of the model. At a depth of ~175-180 km, the buoyant oceanic plateau enables the slab to deflect to a subhorizontal trajectory where it displaces the lower ~60 km CML (Fig. 3.4c). This material accumulates in front of the flat slab and causes the leading edge of the flat slab to bend downward.

Overall, these models show the clear development of flat slab, where the flat slab is deeper for thicker continental plates. In all models, there is thinning of the CML in the wedge corner above the slab by mantle flow during steep-angle subduction. This space is filled by the slab as it deflects to form a flat geometry. As the flat slab advances inboard, the lowermost CML is displaced, with a greater amount of displaced CML for thicker upper plate.

### 3.4.2 The strength of continental mantle lithosphere

We next investigate variations in the rheological strength of the CML. The previous models use  $WO \times 10$ , reflecting relatively dry CML. However, variations in water content and composition will alter the strength (e.g. Karato and Wu, 1993; Beaumont et al., 2006). To examine this, we vary the scaling factor  $f$  of the wet olivine rheology (Eqn. 2.9) to test models with CML rheologies of  $WO \times 1$ ,  $WO \times 2$ ,  $WO \times 30$ , and  $WO \times 50$ . In Fig. 3.5, we

show models with variations in CML strength for a lithosphere thickness of 180 km. We have also tested variations in CML strength for other thicknesses and find that the general trends are similar (Section 3.5.1).

In Figure 3.5a, the model has a CML rheology of  $WO \times 1$ , representing hydrated lithosphere. Following subduction of the oceanic plateau and slab break-off, the slab deflects to a flat geometry. The flat slab intrudes and displaces the lower  $\sim 80$  km of CML, creating a flat slab at 100-105 km depth. If the CML has slightly stronger rheology ( $WO \times 2$ ; Fig. 3.5b), there is a similar behavior, but with a 5-10 km deeper flat slab. The slab in the previous two models is shallower than that in the model with a CML rheology of  $WO \times 10$  (flat-slab depth of 135-140 km; Fig. 3.4c). In Figure 3.5c, the model has a CML strength of  $WO \times 30$ , and the flat slab forms at a larger depth. The slab is at 155-165 km depth at 800 km from the trench. Further inboard, the slab is slightly deeper ( $\sim 175$ -180 km), as some of the displaced CML accumulates above the slab and mixes with the plateau crust. For an even stronger CML ( $WO \times 50$ ; Fig. 3.5d), the CML does not significantly deform and the flat slab is at a depth of 175-180 km. In the last two models, there is little accumulation of CML material in front of the flat slab, owing to the high effective viscosity of CML. These models show that a shallower flat slab tends to occur when the overriding continental plate is weak, as the slab can displace a greater thickness of CML.

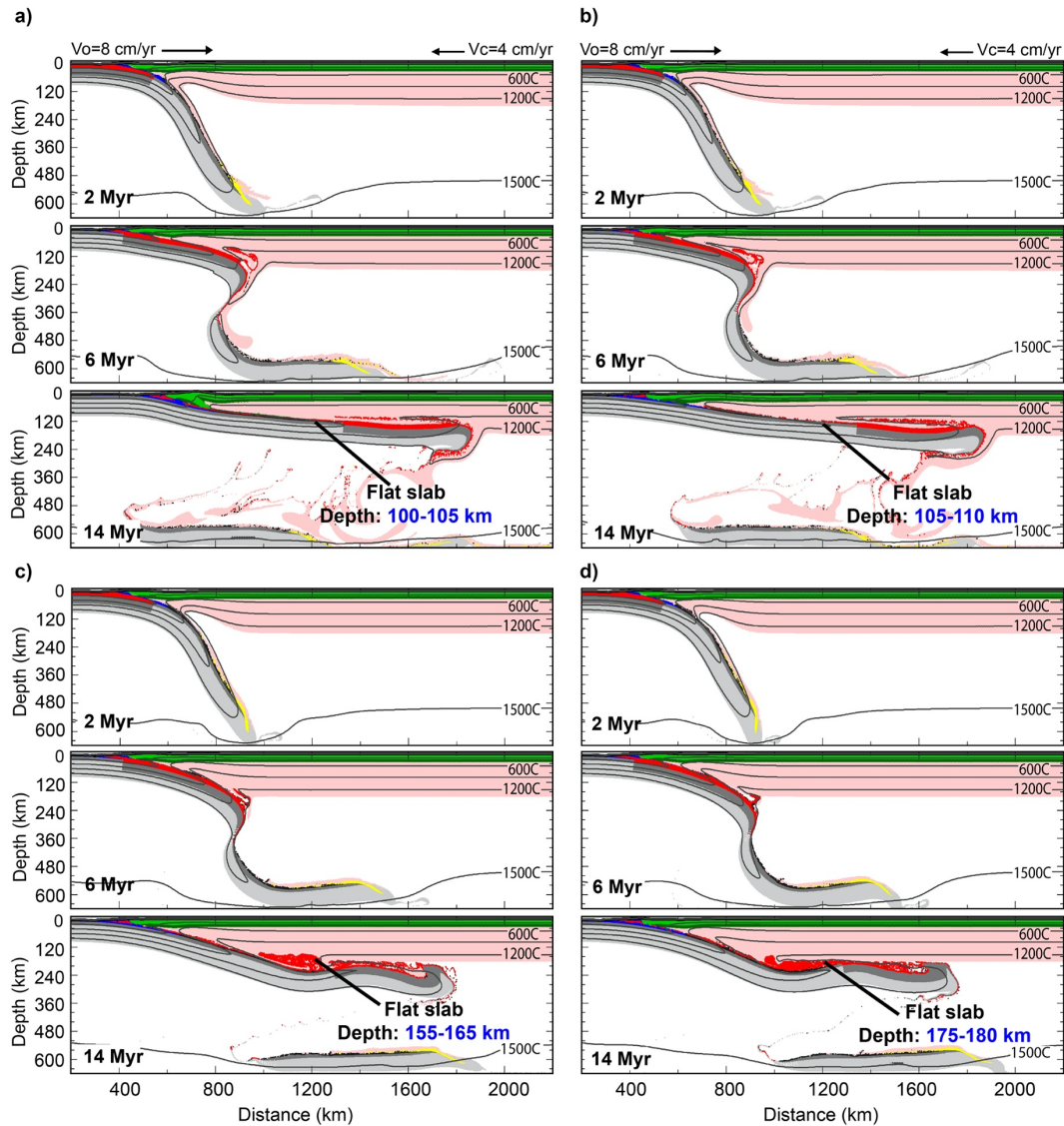


Figure 3.5. Models with different CML strengths for a lithosphere thickness of 180 km, corresponding to rheologies of (a)  $WO \times 1$ , (b)  $WO \times 2$ , (c)  $WO \times 30$ , and (d)  $WO \times 50$ . The reference value for CML is  $WO \times 10$  (see Fig. 3.4c). Material colors as in Figure 3.2a; black lines are isotherms every 300 °C.

### 3.4.3 Distance between craton and trench

The models above assume a uniformly thick continental lithosphere. However, in several places, flat slabs interact with thick cratonic lithosphere (e.g. O’Driscoll et al., 2009; Manea et al., 2012; Humphreys et al., 2015). One area is the western US, where geological

data suggests that the Farallon flat slab truncated the lower part of Wyoming craton lithosphere (Humphreys et al., 2015). In modern flat-slab areas (e.g. Peru and Chile), the flat slab is currently west of the craton and may collide with the craton root in the future. To examine the effect of a craton, we introduce a 240 km thick craton region to the continental plate. The craton thickness is consistent with that of the Wyoming Craton in North America (Humphreys et al., 2015) and Rio de la Plata Craton in South America (Manea et al., 2012). The craton mantle lithosphere has the reference CML rheology of  $WO \times 10$ , reflecting relatively dry conditions. The continental region between the trench and craton has a thickness of 120 km, with a CML rheology of  $WO \times 2$  to represent lithosphere that has been hydrated by the adjacent subduction zone (Liu and Currie, 2016).

We first vary the location of the craton, assuming that both the cratonic and non-cratonic CML have a reference (compositional) density of  $3250 \text{ kg/m}^3$ . Figure 3.6 shows models with the craton margin located 600, 950 and 1300 km from the trench. In all cases, the slab initially flattens below the thin non-cratonic lithosphere at a depth of  $\sim 85$  km. As it encounters the craton edge, the slab is deflected downward and displaces the lower corner of the craton. With continued convergence, the flat slab forms at a depth of 170-180 km below the craton area. For comparison, the model with a uniform 240 km thick continent has a flat-slab depth of 175-180 km (Fig. 3.4d). This suggests that the location of the craton does not strongly affect the depth of the flat slab below the craton area. Even if a shallow flat slab develops below non-cratonic lithosphere near the trench, the slab is deflected to a greater depth as it encounters the thick, strong craton (e.g. Fig. 3.6c).

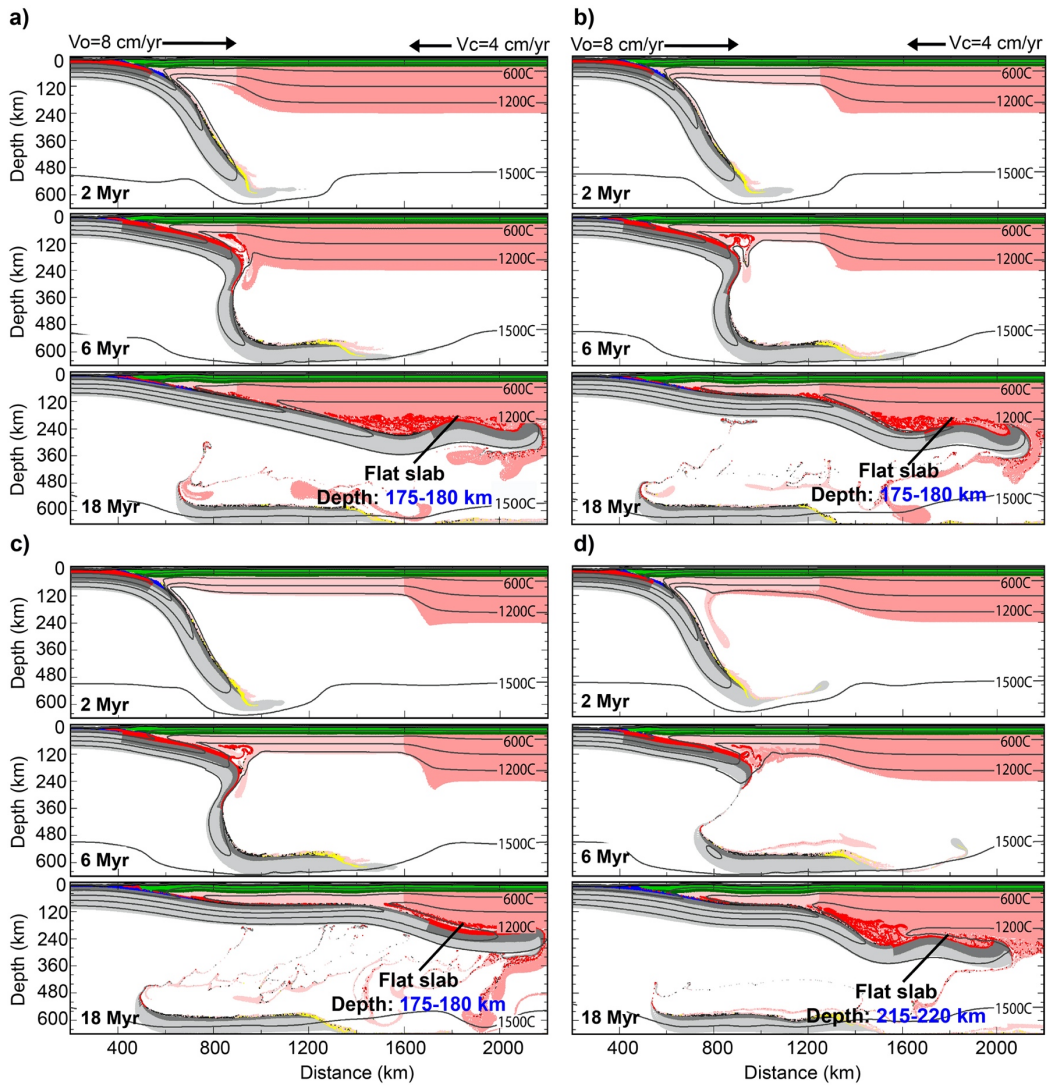


Figure 3.6. Models with a 240 km thick craton located: (a) 600 km, (b) 950 km, and (c) 1300 km from the trench; the continent between the trench and craton is 120 km thick. The craton mantle lithosphere has a reference density of  $3250 \text{ kg/m}^3$ . (d) Model with a craton 950 km from the trench that has a reference density of  $3210 \text{ kg/m}^3$ . Material colors as in Figure 3.2a; black lines are isotherms every  $300^\circ\text{C}$ .

Previous studies have noted that the presence of a craton root can result in an enhanced nonhydrostatic pressure force above the subducting slab, increasing the upward suction force on the slab (O’Driscoll et al., 2009; Manea et al., 2012). In our models, we do not observe a significant difference in the rate of slab flattening with the presence of a

craton. This may be due to the relatively low viscosity of the sublithospheric mantle of our models ( $\sim 10^{19}$  Pa·s; Liu and Currie, 2016). However, we find that a strong craton close to the trench inhibits the development of a flat slab. Figure 3.7a has a 240 km thick craton that is located at the trench (i.e., uniform continental thickness), with a CML rheology of  $WO \times 30$ . During steep-angle subduction, there is little thinning of the CML in the wedge corner, owing to its strong rheology. Figure 3.7b has a 240 km craton that is 600 km away from the trench, with a rheology of  $WO \times 50$ . In this model, the slab develops a flat geometry below the thin lithosphere adjacent to the trench. As it encounters the thick, strong craton root, it is deflected downward at a steep angle. In both models, the oceanic plateau subducts steeply along the edge of the strong craton, as it is unable to significantly displace this material. The buoyant slab does bend upward when reaching the bottom of the craton, primarily due to the buoyancy of the plateau harzburgite layer. This leads to a short-lived flat slab that includes a kink at its seaward end. With continued plate convergence, the negative buoyancy of this kink causes the transient flat slab to be removed.

We find that if the craton has a rheology of  $WO \times 10$  or weaker, a clear flat slab develops regardless of the location of the craton (Figs. 3.6 and 3.14). If the craton is stronger than this and is located within 600 km of the trench, the descending slab maintains a steep angle before it reaches the bottom of the craton (Fig. 3.7). These results are consistent with Manea et al. (2012) who found that a thick craton close to the trench inhibits flattening.

Craton mantle lithosphere may also be compositionally depleted related to the sublithospheric mantle, resulting in lower density at the same temperature (Griffin et al., 2003). Fig. 3.6d shows a model in which the craton CML has a compositional density of

3210 kg/m<sup>3</sup> (40 kg/m<sup>3</sup> lower than the reference value) and the craton is located at 950 km from the trench. Compared to the model with the standard density (Fig. 3.6b), a lower density results in a ~40 km deeper flat slab. With the lower density, it is more difficult for the flattening slab to displace the craton CML. The more buoyant craton also causes the weak oceanic plateau crust to be scraped from the top of the slab, causing a greater accumulation of buoyant plateau crust at the seaward side of the craton. The flat slab only displaces the lower ~20 km of the craton CML, and owing to its low density, this material forms a keel ahead of the flat slab, as described by Axen et al. (2018).

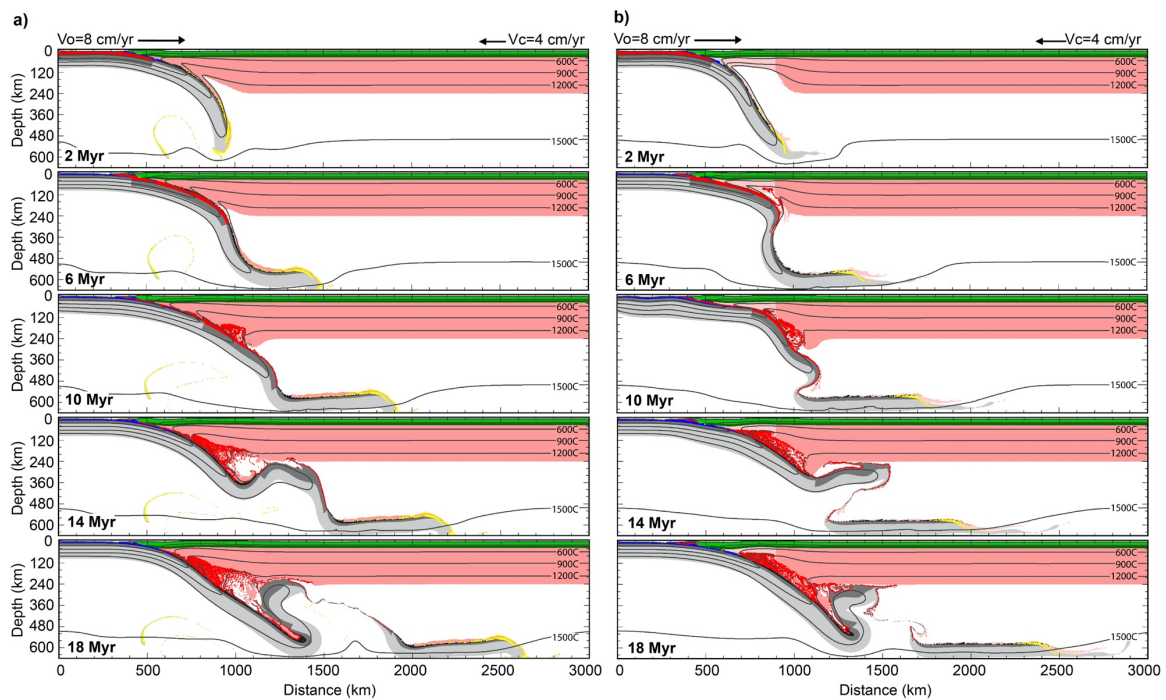


Figure 3.7. Numerical models for strong cratons that are: (a) located at trench with CML of WO x 30 and (b) 600 km from trench with CML of WO x 50. Neither model develops a long-lived flat slab. Material colors as in Figure 3.2a; black lines are isotherms every 300°C. The full model domain is shown.

## 3.5 Controls on flat-slab geometry

### 3.5.1 Effects of CML on flat-slab depth

Figure 3.8a summarizes the flat-slab depth observed in our models for different combinations of initial continental thickness and CML rheology for a uniform continent (Section 3.4.1 and 3.4.2). We find that most models develop a long-lived flat slab. This is induced by the combination of trenchward upper plate motion (e.g. Gutscher et al., 2000b; van Hunen et al., 2004), a buoyant (metastable) oceanic plateau (van Hunen et al., 2002; Arrial and Billen, 2013), and break-off of the deeper high-density slab (Liu and Currie., 2016). In all models, the CML close to the plate margin is ablated by mantle wedge corner flow during steep-angle subduction (Pope and Willett, 1998). This allows the buoyant oceanic plateau to enter the subduction zone at a relatively shallow angle, promoting the development of a flat slab (e.g. Fig. 3.4). The two exceptions are where the initial thickness is 240 km and the CML strength is very high (WO x 30 and WO x 50); i.e., where a strong craton is located adjacent to the trench (c.f. Manea et al., 2012). In these cases, the thick and strong CML causes the buoyant plateau to descend at a relatively steep angle, with only a transient flat slab (Fig. 3.7a).

The flat slabs in our models have depths of 45 to 180 km, with larger depths for cases where the continent is thick and strong (Fig. 3.8a). The shallowest flat slab occurs for the model in which the overriding plate is 60 km thick and a CML rheology of WO x 1; this slab has a depth of 45-50 km (Fig. 3.13). The main control on the flat-slab depth is the initial thickness of the continental plate. This is because the mantle has temperature-dependent viscous rheology, such that the shallow CML is relatively cool and strong. As a result, the flattening slab is deflected below the strong portion of the continent as it

advances, leading to a deeper flat slab for cooler, thicker continents (Fig. 3.4). The strength of the CML is a secondary control on flat-slab depth. For an extremely strong rheology (WO x 50; i.e., dry conditions), the flat-slab depth is approximately the initial continental thickness (Fig. 3.8a). For a weaker CML, the flat-slab depth is shallower, as the lowermost CML is weak enough to be displaced by the flat slab. Figure 3.8b shows the thickness of CML removed by the flat slab. There is more displacement for an initially thicker and weaker continent, as there is a greater thickness of mantle lithosphere that is hot and weak enough to be removed.

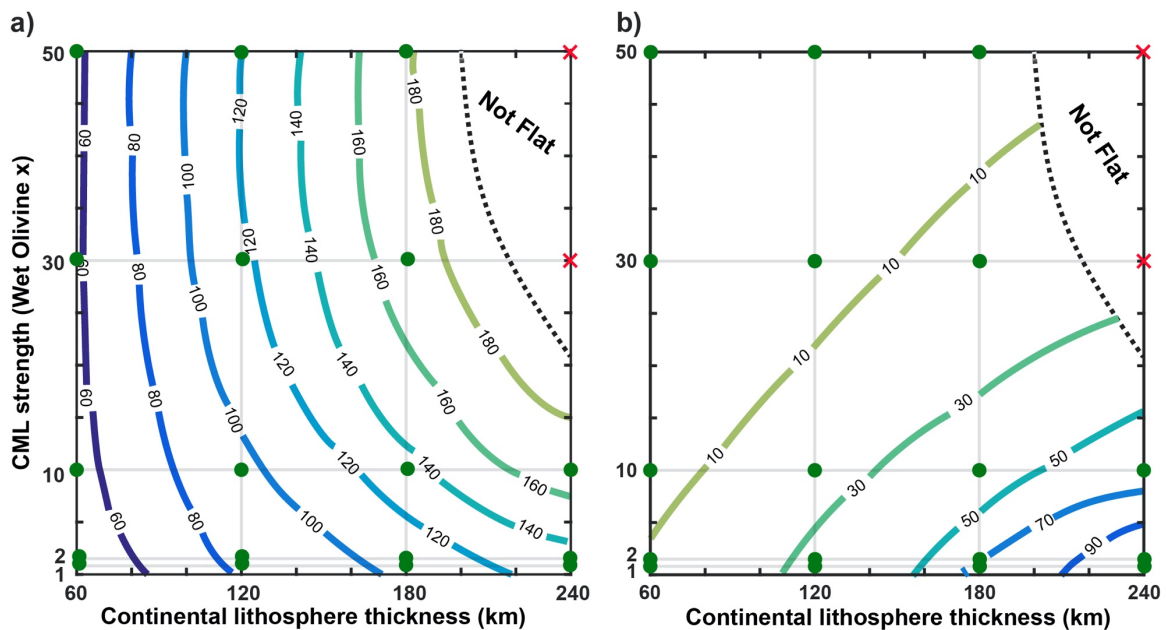


Figure 3.8. Contour plots of models with a uniform continental plate: (a) Flat-slab depth and (b) CML thickness displaced by flat slab. The vertical axis gives the viscous scaling factor ( $f$ ) relative to a wet olivine rheology (Eqn. 2.9). The green dots are models with a flat slab. Red crosses indicate models that did not develop a long-lived flat slab. Black dashed line is the predicted boundary for conditions for flat-slab creation.

To demonstrate the effect of continental structure on flat-slab depth, we plot effective viscosity profiles of the continent in our models (Fig. 3.9). The effective viscosity

depends on composition, temperature and strain rate (Eqn. 2.9). Here, the temperature structure is given by the continental thickness and we use a strain rate of  $10^{-16} \text{ s}^{-1}$ , which is comparable to the strain rate within the CML near the slab surface in the models (Fig. 3.16b). Figure 3.9a shows viscosity and temperature profiles for different initial thicknesses, using the reference  $\text{WO} \times 10$  rheology. The horizontal red dashed lines show the observed flat-slab depths of the models in Figure 3.4. At these depths, the viscosity of CML is  $10^{21}$  to  $2 \times 10^{21} \text{ Pa}\cdot\text{s}$ , corresponding to temperatures of  $\sim 1100^\circ\text{C}$ . This is consistent with the viscosity plot where the flat slab removes CML that has a viscosity  $< 10^{21} \text{ Pa}\cdot\text{s}$  (Fig. 3.16a). In Figure 3.9b, we plot the viscosity profiles for models with a 180 km lithosphere and different CML strengths for the models in Figure 3.6. The flat-slab depth corresponds an effective viscosity of  $2 \times 10^{21}$  to  $3 \times 10^{21} \text{ Pa}\cdot\text{s}$ , and temperature of  $880^\circ\text{C}$  (weakest model) to  $1360^\circ\text{C}$  (strongest model).

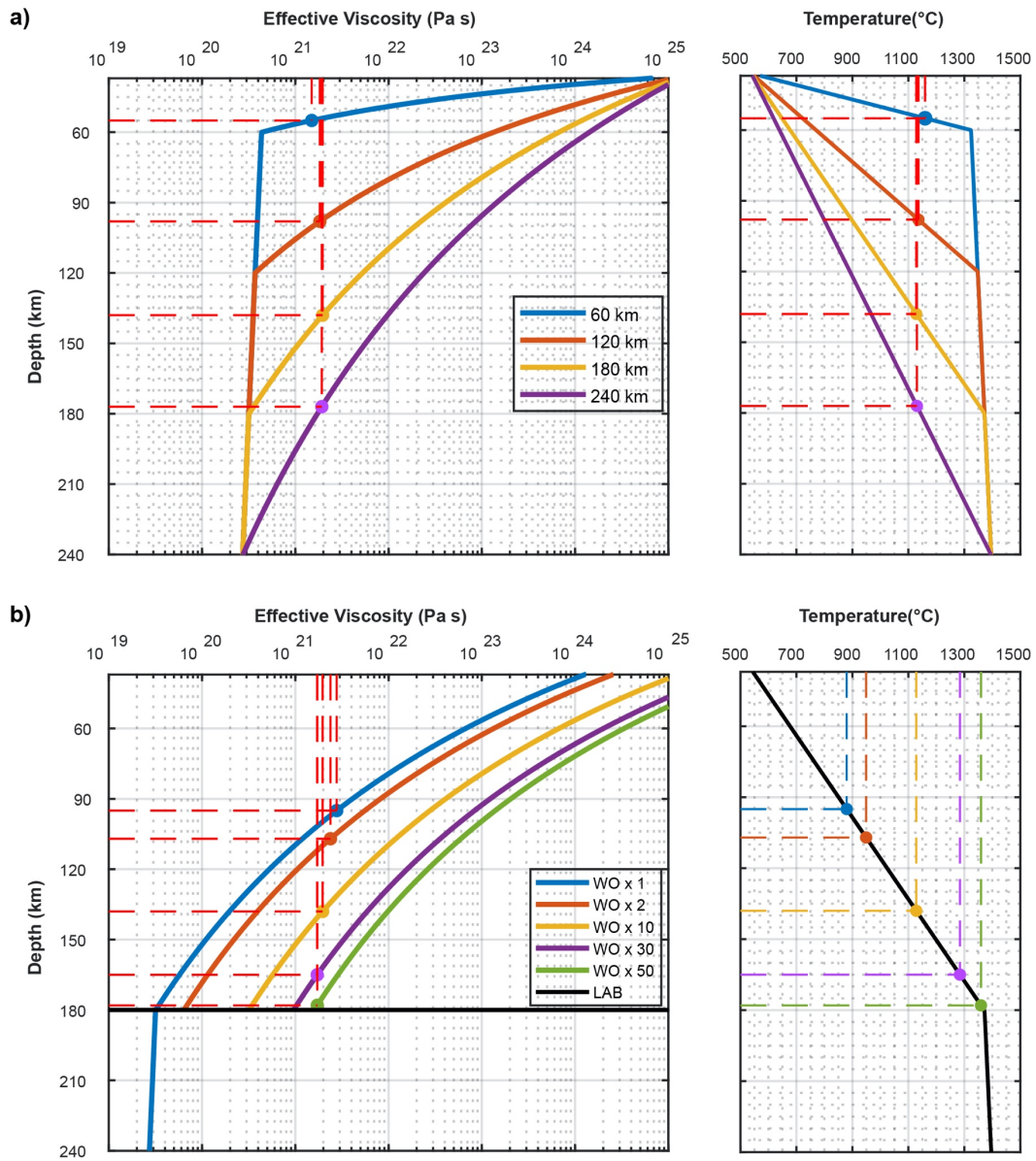


Figure 3.9. Viscosity (left) and temperature (right) profiles of the CML for a strain rate of  $10^{-16} \text{ s}^{-1}$ . (a) CML with a strength of WO x 10 that has different initial thicknesses. (b) 180 km thick continent with different CML strengths; black solid line is the base of the CML. The dashed lines indicate the flat-slab depth in numerical models.

Thermal structure of the continental plate plays an important role in slab dynamics (Rodríguez-González et al., 2012). Our results show that the thermal state of the overriding

plate controls the flat-slab depth, with a secondary control from the CML rheology, which is likely determined by the state of hydration. The oceanic plate in our models is able to displace CML that has an effective viscosity less than  $\sim 3 \times 10^{21}$  Pa·s. The fate of the displaced CML depends on its density. In most models, the CML has the same compositional density as the underlying mantle, and it tends to sink as it is cooler and thus denser. In contrast, compositionally buoyant CML accumulates in front of the flat slab, creating a thick keel (Fig. 3.6d; Axen et al., 2018). We note that none of our models exhibit displacement of the full thickness of CML; the uppermost mantle lithosphere is relatively cool and thus is too strong to be displaced.

The models with a uniform continent show that the flat-slab depth is primarily determined by the viscous strength of the CML, which depends on its initial thickness (temperature) and rheology. If the continental plate includes an area of thick cratonic lithosphere, the flat-slab dynamics in this region depend on the craton structure (Fig. 3.6). As the slab encounters the craton, it is deflected downward due to the presence of the thick, cool lithosphere. The location of the craton does not affect the flat-slab depth. However, the depth is greater for a craton that is rheologically strong and/or compositionally buoyant (Fig. 3.6d and 3.15; Axen et al., 2018). In these cases, the flat slab displaces less CML, leading to a deeper flat slab.

### 3.5.2 Variations in oceanic plate age and convergence rate

The previous models are based on subduction of an old oceanic plate ( $>100$  Ma) at a relatively high convergence rate (12 cm/yr), motivated by Farallon Plate subduction below the western US in the Late Cretaceous (e.g. Torsvik et al., 2008). Modern flat-slab regions in Mexico and South America have younger oceanic plates and lower convergence

rates (e.g. Manea et al., 2017). Figure 3.10 shows models with a convergence rate of 7 cm/yr ( $V_o=5$  cm/yr;  $V_c=2$  cm/yr), compatible with values for present-day South America. Owing to the lower velocities, these models have less convergence over the same time period than the reference model. Thus, we compare the results at the same amount convergence (1680 km), corresponding to a time of 24 Myr in these models and 14 Myr in the reference model.

Figure 3.10a is a model with an old oceanic plate (~100 Ma), and Figure 3.10b is a model with a younger oceanic plate (~30 Ma), that has a warmer lithosphere with a thickness of 70 km. All other parameters (e.g., oceanic plateau size and material properties) are the same as in the reference model (Table 3.1). The overall behavior of these models is similar to that of the reference model with an old plate and fast convergence rate (Fig. 3.4b). Following plateau subduction, all models develop a flat slab with a depth of 95-100 km. We also note that this depth is similar to that in the model with partial eclogitization (Fig. 3.3c) and with variable plateau widths and crustal thicknesses (Fig. 3.11). These results suggest that convergence rate (including the magnitude of continental trenchward motion), oceanic plate age, and oceanic plateau density and structure do not significantly affect the flat-slab depth. Rodríguez-González et al. (2012) also show that the oceanic plate age does not significantly affect slab geometry. The plate velocities (especially continental motion) and oceanic plate structure do play a key role in the development of a flat slab (e.g., Gutscher et al., 2000a; van Hunen et al., 2002; Arrial and Billen, 2013; Liu and Currie, 2016). However, once a flat slab develops, its depth is primarily controlled by the overlying continental structure.

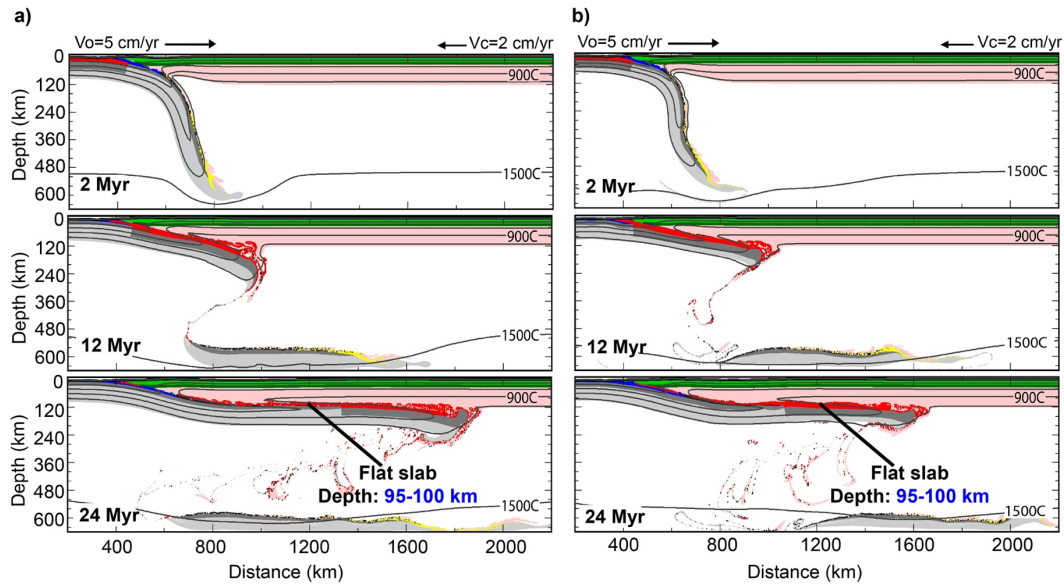


Figure 3.10. Numerical models with a convergence rate of 7 cm/yr: (a) 100 Ma oceanic plate and (b) 30 Ma oceanic plate. Material colors as in Figure 3.2a; black lines are isotherms every 300°C.

### 3.5.3 Implications for ancient and modern flat slabs

Our models provide insights into the range of flat-slab depths observed in nature (Fig. 3.1). One example is the proposed Farallon flat slab event that affected a wide region of the western United States in the Late Cretaceous (e.g. Coney and Reynolds, 1977). This event is inferred to have induced compression of the upper plate, resulting in the Laramide orogeny >1000 km inboard of the subduction margin (e.g. Copeland et al., 2017). Bird (1988) argued that the flat Farallon plate pushed the entire thickness of North America mantle lithosphere to the northeast, such that the flat slab was immediately below the crust, enabling the transfer of compressive stresses into the Laramide region through basal traction. However, none of our models shows the displacement of the full thickness of CML. Instead, we find that the flattening slab displaces the lowermost CML, but the shallow CML remains in place as it is cool and strong, even for a very weak rheology. This

contradicts the idea that hydration of the mantle lithosphere enables a flat slab immediately below the continental Moho (Skinner and Clayton, 2011; Bishop et al., 2018). Further, the temperature-dependent non-Newtonian CML rheology prevents stresses along the top of the flat slab from being transmitted into the shallower lithosphere, further inhibiting removal of the full CML (Axen et al., 2018). Our results are consistent with xenolith data that indicate that the Farallon flat slab was at depths from ~120 km below California to >150 km below Wyoming Craton (Livaccari and Perry, 1993; Usui et al., 2003). The continental lithosphere is inferred to have been ~125 to 250 km thick before the flat slab (Humphreys et al., 2003 and references therein), and thus the Farallon slab likely only displaced the lowermost CML.

Reconstructions of the Farallon flat slab show that it extended more than 1000 km inboard of the trench and interacted with the thick (200-250 km) lithospheres of the Colorado Plateau and Wyoming Craton (e.g. Humphreys et al., 2015). Seismic and xenolith evidence from the Wyoming Craton suggest that the craton mantle lithosphere below 140-150 km was removed by the Farallon flat slab (Humphreys et al., 2015). This is compatible with our models that show that a flat slab is deflected to depths of 130-170 km depth below cratonic lithosphere, such that it displaces the lower 50-90 km (Fig. 3.6). Humphreys et al. (2015) argue that the material at depths greater than ~140 km in the present-day craton is depleted Farallon lithosphere that was emplaced beneath the craton. However, there is no evidence of an oceanic crust layer, leading Humphreys et al. (2015) to propose that the eclogitized crust escaped through a tear in the slab at ~75 Ma. Based on our models, we suggest that another possible explanation is that the oceanic crust was scraped by the craton root and accumulated at the seaward craton boundary and never reached to the craton area

(Fig. 3.15b). Additional work is needed to examine the fate of the crustal material and whether oceanic lithosphere could persist below the Wyoming craton since the Late Cretaceous.

Modern flat slabs below South America and Mexico show a range of depths (Fig. 3.1). The Pampean flat slab is at a depth of  $\sim 110$  km,  $>50$  km below the continental Moho (Manea et al., 2017). This is consistent with our models that show the development of a flat slab below an area of continental lithosphere that was initially 120-180 km thick (Fig. 3.9a). In other places, the flat slab is close to the continental Moho. For Peru, there is less than 3 km CML between the flat slab and overlying continental Moho (Bishop et al., 2017). Our models suggest that this region may have had thin CML prior to the flat-slab emplacement. Alternately, Bishop et al. (2017) note that the Peru flat slab coincides with a region of locally thinned crust and propose that the flat slab may have displaced the lower  $\sim 10$  km of crust and presumably the underlying mantle lithosphere. Although our models (with a 36 km thick crust) show that the shallow CML is too cool and strong to be displaced, a region with 50-60 km thick crust may have a weak lower crust that enhances the mobility of the lower lithosphere, enabling its displacement. Further work is needed to examine this. A shallow flat slab is also found at the Mexico subduction zone ( $\sim 45$  km depth; Kim et al., 2012), and there are low-angle slabs with little overlying CML in northern Colombia and eastern Alaska (e.g. Gutscher et al., 2000a). In these regions, the continental crust thickness is similar to that in our models, and we conclude that the observed shallow flat slab indicates a thin upper plate prior to flat-slab development.

#### 3.5.4 Model limitations

All models presented in this work are 2D numerical models, assuming plane strain. The 2D models provide insights into how a subducting slab evolves into a flat geometry and the interactions with the overlying plate. An implicit assumption is that the slab pull that drives continued subductions comes from adjacent regions with a negatively buoyant oceanic plate (e.g. van Hunen et al., 2002). However, these models cannot be used to assess how along-strike factors, such as variations in oceanic and continental structure and along-strike mantle flow, may affect the dynamics (e.g. Martinod et al., 2005; Hu and Liu, 2016; Taramón et al., 2015). The flat-slab segments in nature have a limited along-strike extent. A key question is what happens at the edge of the flat-slab segments; does slab flattening create a tear at the edge of the flat segment (e.g. Hu and Liu, 2016) or is there a more gradual along-strike change in slab dip (e.g. Bishop et al., 2017). These questions should be addressed using full 3D model.

Our models also assume a model domain that extends to 660 km depth, with a closed bottom boundary. This boundary does not significantly affect the flat slab, owing to the detachment of the slab ahead of the flat segment. However, in 25% subduction zones, the descending slab penetrates into the lower mantle (Lallemand et al., 2005). This may change the negative buoyancy of the descending oceanic plate in steep-angle regions, which may affect adjacent flat-slab areas. Further, in Peru and Chile, there does not appear to have been a slab break-off at the leading edge of the flat slab (e.g. Manea et al., 2017), and thus the dynamics of the deep slab segment and the strength of the slab may be important (e.g. van Hunen and Allen, 2011). We also note that our models use a proxy approach for mantle convection, with a high mantle thermal conductivity in Phase 1 to

generate an adiabatic mantle with a potential temperature of 1300°C. A higher or lower potential temperature will influence the mantle rheology and density, and thus the propensity for flat-slab subduction (van Hunen et al., 2004). In future modelling studies, these factors need to be investigated.

### 3.6 Conclusions

Geological and geophysical observations indicate regions of modern and ancient flat-slab subduction, where the subducting oceanic plate has a sub-horizontal geometry at depths ranging from just below continental Moho to >100 km (Fig. 3.1). Our numerical models show that an old oceanic plate develops a flat geometry with the combination of trenchward motion of the overriding continent and subduction of an oceanic plateau, where the plateau crust remains at least partially metastable, consistent with earlier studies (e.g., van Hunen et al., 2002; Arrial and Billen, 2013). The models also demonstrate that a thick, strong craton close to the trench can prevent the development of a flat slab (Manea et al., 2012). The main focus of our work is the depth at which the flat slab occurs. We find that the initial thickness of the overlying continental lithosphere is the key control on flat-slab depth, with CML rheology being a secondary control. Other factors, such as the age (or density) of the oceanic plate and the location of a thick craton, have little effect. The flat-slab depth increases with increasing upper plate thickness because the flat slab cannot displace the shallow cool and strong continental lithosphere due to the temperature-dependent CML rheology. The top of flat slab coincides with the depth at which the lithosphere temperature is ~1100°C for a relatively dry rheology. For a weaker (more hydrated) rheology, the flat slab can displace a greater thickness (up to 50%) of the deep CML, corresponding to temperatures as low as ~900°C.

Our models provide insight into the observed variations in flat-slab depth (Fig. 3.1). None of our models show displacement of the full thickness of continental mantle lithosphere. Therefore, the regions where the flat slab is located close to the continental Moho (e.g. Mexico and Peru) must have had an anomalously thin continent prior to flat-slab development. In addition, the models show that a flat slab can displace the lower ~100 km of a continental craton. This has implications for modification of Wyoming craton where Humphreys et al. (2015) argue that >50 km of the deep craton root was removed by the Farallon flat-slab subduction.

### **3.7 Supporting information**

#### 3.7.1 Introduction

The numerical models presented in this Chapter are listed in Table 3.2 and 3.3. The tables list the key parameter variations (e.g., oceanic plate age, continental thickness, CML strength, and the presence of craton). All other parameters are the same as shown in Table 3.1. Figures shown here are used to support the main article.

Table 3.2. Subduction numerical models to examine flat-slab development using an old oceanic plate (100 Ma).

Figure #	Oceanic plateau	Eclogitization percentage of oceanic plateau crust (density)	Plateau thickness (km)	Plateau width (km)
3.3a	none	n/a	n/a	n/a
3.3b	✓	100% (3450 kg/m <sup>3</sup> )	18	600
3.3c	✓	30% (3075 kg/m <sup>3</sup> )	18	600
3.3d: Reference Model	✓	0% (2950 kg/m <sup>3</sup> )	18	600
3.11-1	✓	0% (2950 kg/m <sup>3</sup> )	10	600
3.11-2	✓	0% (2950 kg/m <sup>3</sup> )	14	600
3.11-3	✓	0% (2950 kg/m <sup>3</sup> )	22	600
3.11-4	✓	0% (2950 kg/m <sup>3</sup> )	18	200
3.11-5	✓	0% (2950 kg/m <sup>3</sup> )	18	300

Table 3.3. Numerical models to examine flat-slab depth. Craton location indicates the distance between trench and left boundary of the craton.

Figure #	Continental plate		Craton location (km)	Craton CML density (kg/m <sup>3</sup> )	Convergence rate (cm/yr)	Oceanic plate age (Ma)		
	Thickness (km)	CML strength (W O x f)						
3.4a (3.12)	60	10	n/a	n/a	12	Old oceanic plate (100Ma)		
3.13	60	1						
3.3d, 3.4b: Reference model	120	10						
3.4c	180	10						
3.5a	180	1						
3.5b	180	2						
3.5c	180	30						
3.5d	180	50						
3.4d	240	10	Craton					
3.14a	240	2						
3.7a	240	30						
3.6a (3.15a)	240	10					600	3250
3.6b	240	10					950	3250
3.6c	240	10					1300	3250
3.6d (3.15b)	240	10					950	3210
3.14b	240	2					600	3250
3.7b	240	50					600	3250
							Continental plate	
3.10a	120	10	n/a	n/a	7	Old oceanic plate (100Ma)		
3.10b	120	10			7	Young oceanic plate (30Ma)		

### 3.7.2 Effect of oceanic plateau properties on flat-slab development

In Figure 3.11, we show models with different oceanic plateau properties. The first three models have oceanic plateau crust thicknesses of 10 km (Fig. 3.11-1), 14 km (Fig. 3.11-2), and 22 km (Fig. 3.11-3), where the plateau crust remains metastable during subduction. At 6 Myr (Fig. 3.11a), a thicker, thus more buoyant, plateau crusts result in an earlier break-off of the frontal dense oceanic plate, and there is no break-off for a plateau thickness of 10 km. Figure 3.11b shows these models at 14 Myr. We find that the buoyant oceanic plateau crust needs to be at least  $>10$  km thick to be able to generate a flat slab for the conditions in our models. By comparing the flat-slab depth at 14 Myr for the 14 km and 22 km thick plateau crust, we find that both models have a depth of 95-100 km. This is similar to that of the reference model with the 18 km thick crust (Fig. 3.4b). Therefore, the thickness of the oceanic plateau has little influence on flat-slab depth. We also assess variations in oceanic plateau width; the width in the reference model is 600 km. Figure 3.11-4 has a plateau width of 200 km and Figure 3.11-5 has a width of 300 km. These models show that the oceanic plateau width needs to be  $>200$  km to be buoyant enough to develop a flat slab. After the development of a flat slab, the width of the oceanic plateau does not affect the slab depth, where all the flat-slab models in Figure 3.11 and Section 3.3 have a flat-slab depth of 95-100 km. From this, we conclude that the properties of the oceanic plateau crust (i.e., thickness, width, density) control the buoyancy feature of the oceanic plate, which determines whether a flat geometry can develop. However, these properties have little effect on flat-slab depth.

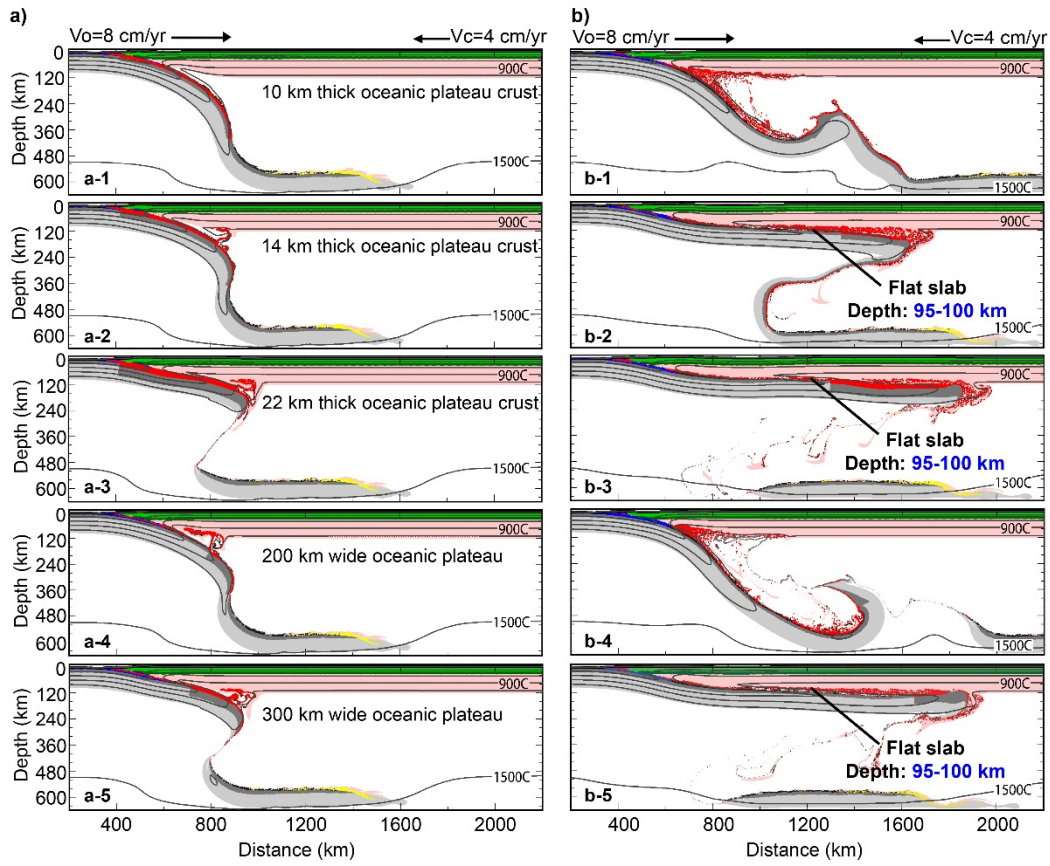


Figure 3.11. Models with different oceanic plateau crust thicknesses (10, 14, and 22 km) and plateau widths (200 and 300 km). Model geometry at (a) 6 Myr and (b) 14 Myr. Material colors as in Figure 3.2a; black lines are isotherms every 300°C.

### 3.7.3 Shallow flat slab

Figure 3.12 shows the full model domain of the model in Figure 3.4a at 14 Myr. The model has a 60 km continental lithosphere with a CML rheology of  $WO \times 10$ . In the late stages of the model, the continental lithosphere breaks near the right (landward) boundary of the model domain. This is because the upper plate is under compression by stresses created at the shallow plate boundary during flat-slab subduction (Axen et al., 2018). These are large enough to deform the thin, hot continental lithosphere in this model. This can be seen by the 300 km inland migration of the trench and thickened continental

crust at a horizontal distance of  $\sim 2800$  km. This occurs after the flat slab has developed and thus does not impact the key conclusions of this study which focuses on the flat-slab depth. Models with a thicker or stronger continental lithosphere do not undergo deformation.

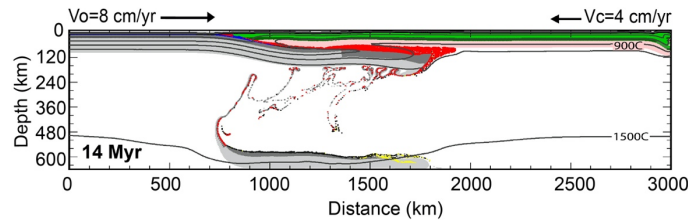


Figure 3.12. Full model domain for the model shown in Figure 3.4a at 14 Myr. Material colors as in Figure 3.2a; black lines are isotherms every  $300^{\circ}\text{C}$ .

In Figure 3.13, the model has a continental thickness of 60 km and a weak CML rheology of  $\text{WO} \times 1$ . This model has the shallowest flat-slab depth among our models. As in other models, the slab develops a flat geometry after a slab break-off as the buoyant oceanic plateau enters the subduction zone. Owing to thin and weak CML, the continental lithosphere near the landward boundary of the model deforms in the later stages (similar to that seen in Fig. 3.12), and thus we show the model evolution before 10 Myr. There is  $\sim 250$  km inland migration of the trench during this period. The top of the flat slab is at a depth of 45-50 km leaving a 10-15 km thick CML layer in between the continental crust and oceanic plate.

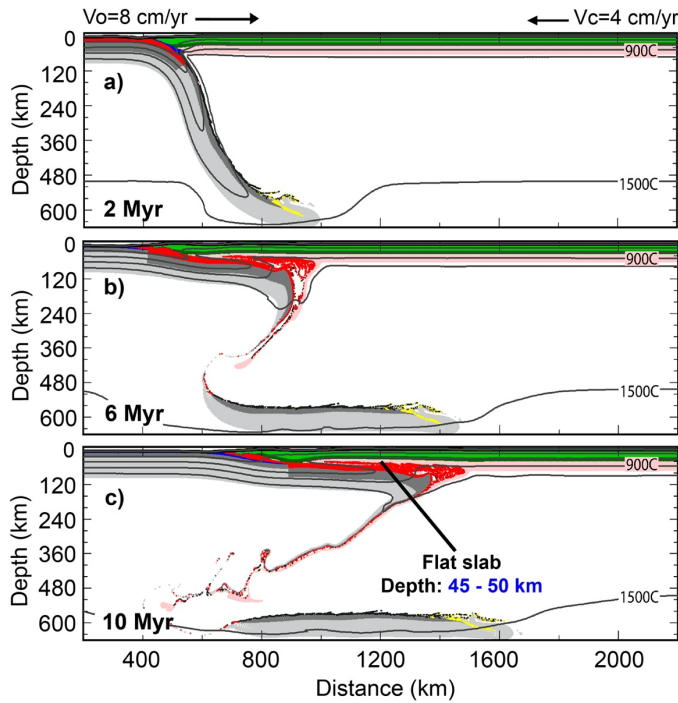


Figure 3.13. Model with 60 km continental lithosphere and weak CML rheology (WO x 1). Material colors as in Figure 3.2a; black lines are isotherms every 300°C.

#### 3.7.4 Models with weak craton CML

Figure 3.14a has a uniform 240 km thick continental lithosphere and a relatively weak rheology (WO x 2); this is equivalent to a craton being located adjacent to the trench. Prior to oceanic plateau subduction, the weak craton lithosphere close the margin is thinned by mantle wedge corner flow during steep-angle subduction. This allows the buoyant plateau to enter the subduction zone at a relatively shallow angle. It is then deflected to a sub-horizontal trajectory, forming a flat geometry at 135-140 km depth.

Figure 3.14b shows a model in which the weak craton is located 600 km from the trench. The oceanic slab first flattens beneath the 120 km thick normal lithosphere and is then deflected downward as it encounters the craton. Due to the weak craton rheology, the flat slab displaces the lower 100 km of the craton and has a depth of 135-145 km,

approximately 40 km shallower than the model with a stronger craton (WO x 10; Fig 3.6a). This depth is similar to the slab depth in Figure 3.14a, suggesting that the main control on slab depth is the craton structure, rather than its location.

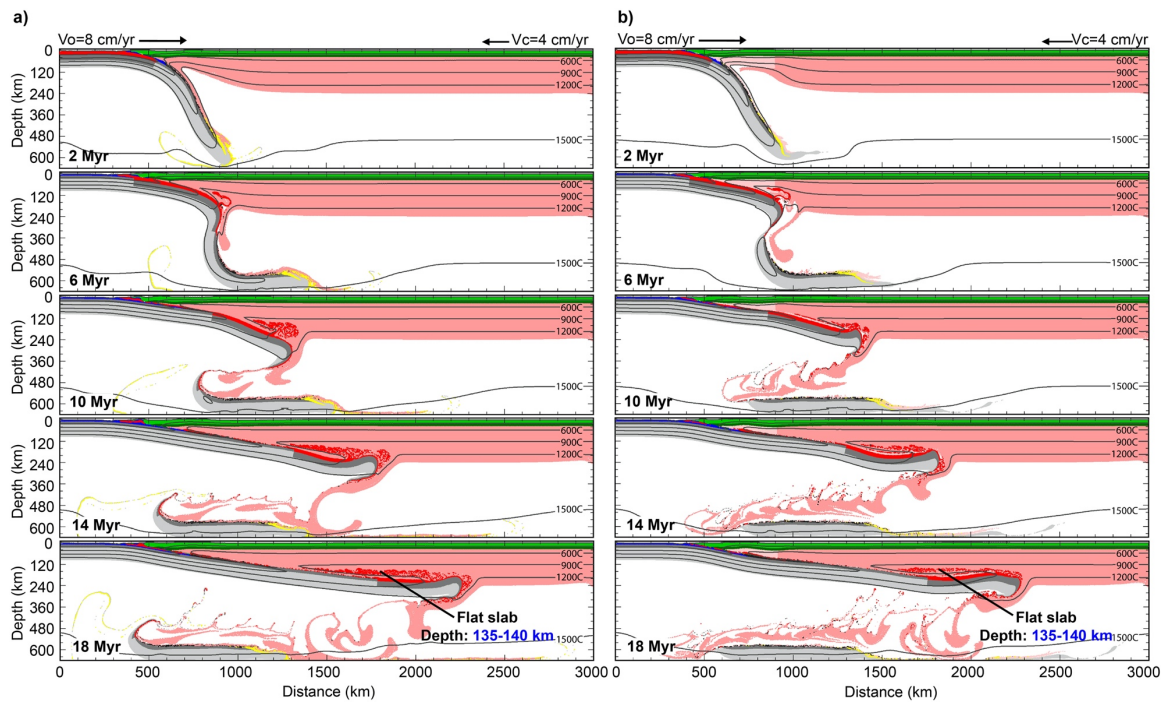


Figure 3.14. Models containing a weak craton (rheology of WO x 2) located: (a) at the trench, and (b) 600 km from the trench. Material colors as in Figure 3.2a; black lines are isotherms every 300°C.

### 3.7.5 Craton mantle lithosphere density

Figure 3.15 shows the full model domain for the models in Figures 3.6b and 3.6d. The compositional densities of craton CML are 3250 kg/m<sup>3</sup> (Fig. 3.15a) and 3210 kg/m<sup>3</sup> (Fig. 3.15b). Both models have a flat-slab geometry beneath the thick craton root. The model in Figure 3.14a has a flat-slab depth of 170-175 km, and the oceanic plateau crust is evenly distributed on the slab surface. The model in Figure 3.15c has a flat-slab depth of

215-220 km, and most of the oceanic plateau crust accumulates at the seaward side of the craton. As discussed in the main text, these differences occur because the more buoyant craton CML (Fig. 3.15b) resists displacement owing to its low density. In addition, the part of the buoyant CML that is displaced forms a keel ahead of the flat slab (Axen et al., 2018) as its low compositional density offsets the density increase associated with low temperatures. In contrast, when the compositional density of CML is the same as that of the sublithospheric mantle, the scraped CML material sinks into the mantle (Fig. 3.15a), as it is cooler, and thus denser, than the underlying material.

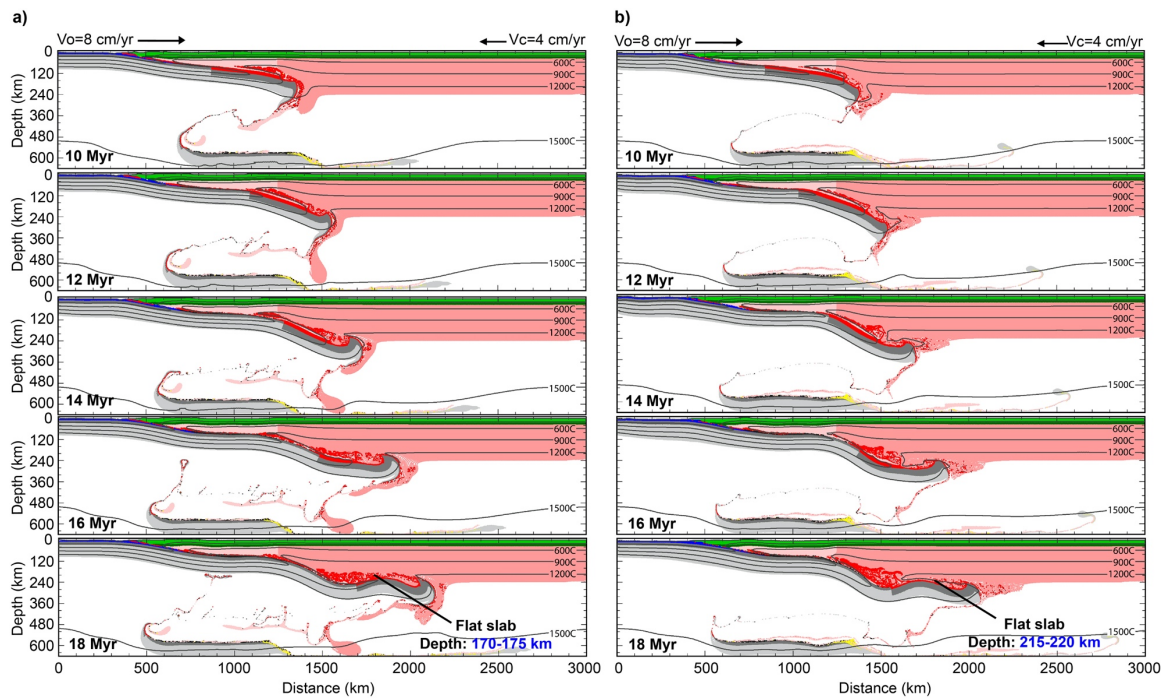


Figure 3.15. Numerical models with different craton mantle lithosphere density: (a)  $3250 \text{ kg/m}^3$  and (b)  $3210 \text{ kg/m}^3$ ; these are the reference densities at  $1344^\circ\text{C}$ . Material colors as in Figure 3.2a; black lines are isotherms every  $300^\circ\text{C}$ .

### 3.7.6 Viscosity and strain rate of the reference model

Figure 3.16 shows the velocity field, effective viscosity, and second invariant of the strain rate for the reference model (Fig. 3.4b). It also shows that flat slab develops through the horizontal convergence of the oceanic plateau which has a negative buoyancy; note that there is no significant upward velocity within the slab. The average viscosity of the sublithospheric mantle in our model is  $10^{19}$  Pa·s, with higher viscosities within the cool slab and cool CML that both have a stronger rheology. The reference model has a flat-slab depth of 95-100 km (black solid line in Fig. 3.16). At this depth, the viscosity of the continental mantle lithosphere is around  $10^{21}$  Pa·s, and the deeper materials are weak enough to be displaced by the flat slab. The strain rate in the sublithospheric mantle and in the shear zone near the surface of the subducting slab are  $10^{-16}$  s<sup>-1</sup>. These values of viscosity and strain rate are consistent with the calculations in Figure 3.9.

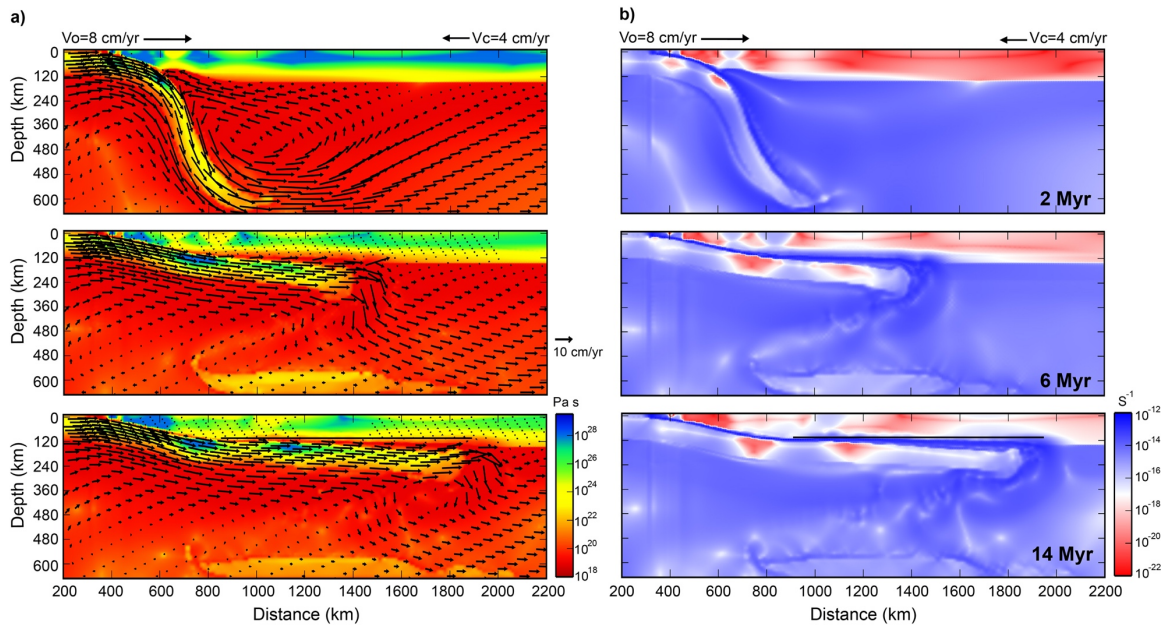


Figure 3.16. (a) Effective viscosity and velocity field of the reference model. (b) Second invariant of the strain rate of the reference model. The solid line shows the approximate location of the slab surface in flat-slab segment at 14 Myr.

---

## Chapter 4 Cooling of the continental plate

---

### Abstract

Most flat-slab subduction regions are marked by an absence of arc volcanism, consistent with closure of the hot mantle wedge as the subducting plate flattens below the continent. Farther inland, low surface heat flow is observed, which is generally attributed to cooling of the continent by the underlying flat slab. However, modern flat slabs have only been in place for <20 Ma, and it is unclear whether there has been sufficient time for cooling to occur. We use numerical models to assess temporal variations in continental thermal structure during flat-slab subduction. Models show that the flat slab leads to continental cooling on timescales of 10's of Myr. Cool slab temperatures must diffuse through the continental lithosphere, creating a delay between slab emplacement and surface cooling. Therefore, the timescales primarily depend on the flat-slab depth, with shorter timescales for a shallow slab. The magnitude of cooling increases for a shallow or long-lived flat slab, old subducting plate, and fast convergence rate. For regions with flat slabs at 45-70 km depth (e.g. Mexico and Peru), shallow continental cooling initiates 5-10 Ma after slab emplacement, and low surface heat flow in these regions is largely explained by the presence of the flat slab. However, for the Pampean region (Chile) with a ~100 km deep slab, our models predict that conductive cooling has not yet affected the surface heat flow. The observed low heat flow requires additional processes, such as fluids related thermal effects through dehydration of the flat slab.

## 4.1 Introduction

The thermal structure of continental lithosphere is significantly modified by a nearby subduction zone. In areas where the oceanic plate descends steeply into the mantle, partial melting in the mantle wedge generates a volcanic arc on the overlying continental plate, 150-300 km from the trench (Turcotte and Schubert, 2002; Syracuse and Abers, 2006). The volcanic arc divides the thermal regime of the continent into a cool forearc region and a hot back-arc region (Dumitru et al., 1991). The forearc temperatures are primarily controlled by conductive cooling by the underlying subducting plate (Wada and Wang, 2009). Conversely, in the arc and back-arc, the presence of a hot mantle wedge and the thermal effects of magmatism lead to high continental temperatures (e.g. Currie and Hyndman, 2006). As a result, back-arcs have a high surface heat flow of  $80\pm 20$  mW/m<sup>2</sup>; in contrast, most forearcs have heat flow of 30-50 mW/m<sup>2</sup> (Gutscher, 2002; Hyndman et al., 2005; Currie and Hyndman, 2006; Wada and Wang, 2009; Marot et al., 2014).

In some subduction zones, the subducting oceanic plate bends in the shallow mantle to become subhorizontal below the continental plate, instead of continuing to descend steeply into the mantle. In these regions, the flat slab is in contact with the overlying continental lithosphere, displacing the hot mantle wedge (Lipman et al., 1972; Dumitru et al., 1991; Humphreys et al., 2003; Axen et al., 2018). Flat-slab regions are generally characterized by the absence of an active volcanic arc (e.g. Kay and Abbruzzi, 1996; Gutscher et al., 2000a; Ramos et al., 2002) and relatively low surface heat flow (20-70 mW/m<sup>2</sup>; Henry and Pollack, 1988; Hamza and Muñoz, 1996; Marot et al., 2014; Sánchez et al., 2018). The low heat flow is usually explained by cooling of the continental plate by

the cool flat slab at its base (e.g. Dumitru et al., 1991; van Hunen et al., 2004; Currie and Hyndman, 2006; Manea et al., 2017).

Several episodes of flat-slab subduction have occurred for both North and South America since the Late Cretaceous (e.g. Lipman et al., 1972; Coney and Reynolds, 1977; Gutscher et al., 2000a; Ramos and Folguera, 2009). For the Pampean flat slab in central Chile (~27 to 33°S; Fig. 4.1), seismic data shows that the subducted Nazca plate becomes flat at a depth of 90-110 km at distances from 300 to 600 km from the trench before it bends downward into the mantle (Anderson et al., 2007; Gans et al., 2011; Porter et al., 2012; Marot et al., 2014). This area is marked by an absence of present-day arc magmatism (Kay and Abbruzzi, 1996). Based on the magmatic record, it is inferred that the onset of flat-slab formation at current latitudes began at ~11 Ma (Yáñez et al., 2001), and reached its current geometry by ~5 Ma (e.g. Gutscher et al., 2000a; Kay and Mpodozis, 2002; Löbens et al., 2011). The development of flat-slab subduction coincides with an eastward expansion of magmatism and the full cessation of volcanism in the last 5-2 Ma (e.g. Urbina et al., 1997; Kay and Mpodozis, 2002). The formation of the flat slab is partially attributed to the subduction of the Juan Fernandez Ridge (JFR), which is assumed to be buoyant due to its comparatively thick oceanic crust (von Huene et al., 1997; Ramos et al., 2002; Kopp et al., 2004). Trenchward motion of the continent and increasing suction force due to a thick cratonic root nearby likely also contribute to the formation of flat-slab subduction (e.g. O'Driscoll et al., 2009; Manea et al., 2012).

There is limited thermal data for the Pampean flat-slab region (Fig. 4.1). Surface heat flow has been determined directly through 32 borehole temperature measurements and indirectly through Curie depth estimates from magnetic data (e.g. Uyeda and Wantanabe,

1982, Hamza and Muñoz, 1996; Collo et al., 2018; Sánchez et al., 2018). Above the flat slab, surface heat flow is 40-60 mW/m<sup>2</sup> (Fig. 4.1b; e.g. Hamza and Muñoz, 1996; Collo et al., 2018), which is lower than the typical back-arc values of 60-100 mW/m<sup>2</sup> (e.g. Gutscher, 2002; Hyndman et al., 2005; Currie and Hyndman, 2006). The low heat flow suggests a cool Pampean lithosphere, but there is debate about the extent of cooling. Heat flow measurements have uncertainties of at least ±15% (Lewis et al., 2003). Further, basin thermochronology measurements by Stevens Goddard and Carrapa (2018) indicate that the region above the Pampean flat slab has a relatively high geothermal gradient that corresponds to a surface heat flow of 58-80 mW/m<sup>2</sup>, with little evidence for cooling since the Miocene. This is higher than the heat flow values of <60 mW/m<sup>2</sup> from Collo et al. (2011; 2017; 2018). Stevens Goddard and Carrapa (2018) propose that the lack of significant cooling is due to the short time since the formation of the flat slab.

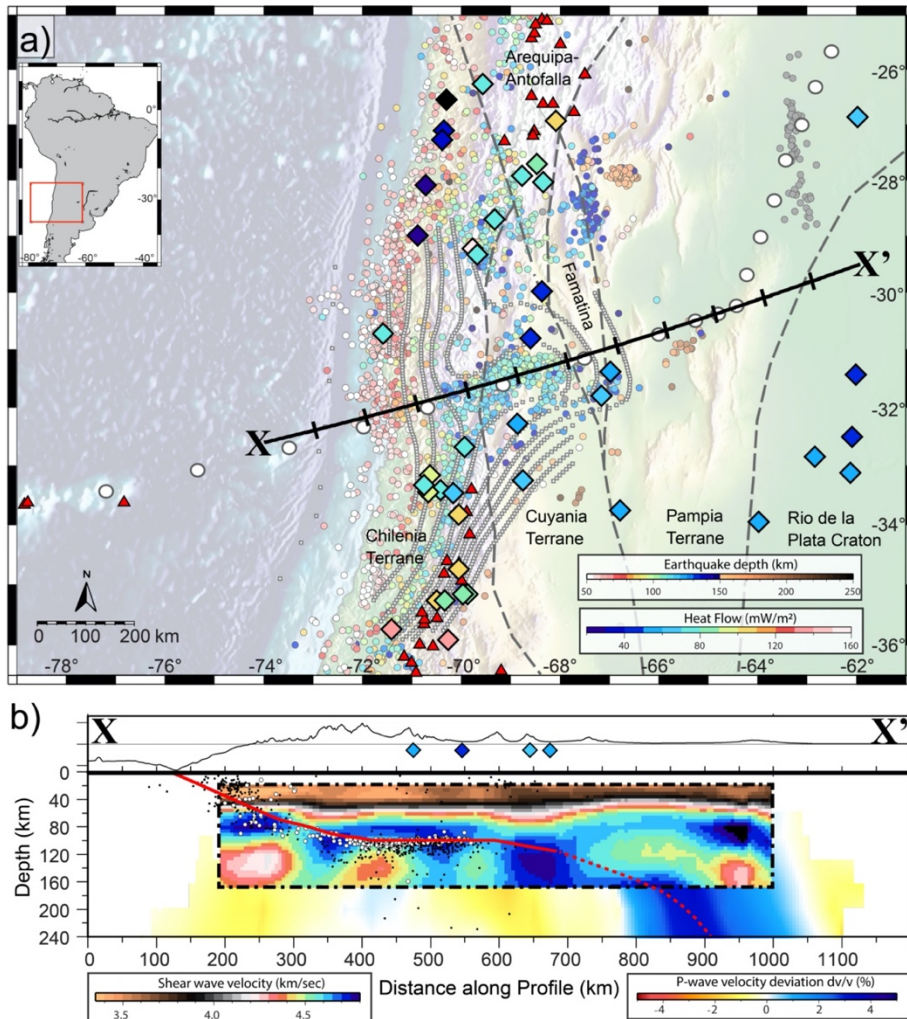


Figure 4.1. (a) The Pampean flat-slab area. Large diamonds are heat flow data points from Uyeda and Wantanabe (1982), Hamza and Muñoz (1996), and Collo et al. (2018). White circles are the projected Juan Fernandez Ridge track location following Yañez et al. (2001). Red triangles show Holocene volcanism. Solid black line (X-X') indicates location of cross section shown in (b), with tick marks every 100 km. Dashed grey lines show terrane boundaries following Ramos et al. (2010) and Martin et al. (2020). Small circles show earthquake locations from the Reviewed ISC catalog from 1990–2015 for events with depths  $>50$  km and  $M > 4$ . Dotted contours show slab depth at 20 km intervals from Anderson et al. (2007). (b) Cross section along X-X' profile. Black line at top shows topography/bathymetry. Diamonds on topography show heat flow measurements within 100 km of the profile projected to the closest point on the profile. Red solid line shows the slab surface from Anderson et al. (2007). Dashed red line is inferred slab continuation based on tomography and earthquake locations. Small black dots show the Reviewed ISC catalog locations within 20 km of the profile. White circles are projected earthquakes from Anderson et al. (2007) within 20 km of the profile. Colors within dash-dot outlined box are absolute shear wave velocities from the Rayleigh wave

tomography of Porter et al. (2012). Background colors are teleseismic P-wave velocity deviations from Portner et al. (2017).

Other flat-slab regions also appear to have relatively cool continental lithosphere. Two well-studied modern flat slabs are in central Mexico and Peru. In both places, the subducted plates are inferred to have developed flat geometries in the last 20 Ma, and the flat slabs are found at depths of ~45 km for Mexico and 60-70 km for Peru (e.g. Ferrari et al., 1999; Pérez-Campos et al., 2008; Hampel, 2002; Antonijevic et al., 2015; Kumar et al., 2016; Bishop et al., 2017). Neither area has an active volcanic arc above the flat portions (e.g. Ferrari, 2004; Rosenbaum et al., 2005). In central Mexico, the surface heat flow is 13-40 mW/m<sup>2</sup> between the trench and the Trans-Mexico Volcanic Belt (~350 km from the trench) where the slab resumes a steep angle (Ziagos et al., 1985). In Peru, the heat flow above the Peruvian flat slab is 20-60 mW/m<sup>2</sup>, which is lower than that of the back-arc regions above the steep-angle slabs to the north and south (80-120 mW/m<sup>2</sup>) (Henry and Pollack, 1988; Muñoz, 2005).

In the western US, Farallon flat-slab subduction is inferred to have induced widespread cooling of the continental lithosphere from the Late Cretaceous to Eocene (Dumitru et al., 1991; Smith, 2020). The subducted Farallon plate started to develop a flat geometry at ~90 Ma, eventually creating a flat-slab segment at 120-150 km depth that extended more than 1500 km from the plate margin and persisted until ~50 Ma (e.g. Coney and Reynolds, 1977; Copeland et al., 2017). Thermochronological data in the region of the volcanic arc shows that cooling started 5-10 Myr after the local cessation of magmatism (Dumitru et al., 1991). Fission-track data indicates that upper crust temperature decreased by ~200°C over 10 Myr after the onset of cooling (Dumitru, 1990). Farther into the

continental interior, thermochronology data also shows cooling of the shallow continent, but the magnitude is reduced (Dumitru et al., 1991). In addition, cooling in the continental interior started later and occurred more gradually than in the former arc region. This is interpreted to reflect both extra time it took for the Farallon flat slab to reach the continental interior, and the fact that flat slab was at a greater depth here, and therefore, it took longer for the thermal effects of the cool slab to reach the shallow crust (Bird, 1988; Dumitru et al., 1991).

The above observations support the idea that flat-slab subduction regions are associated with relatively cool lithosphere compared to normal-slab regions. This is consistent with the idea that the flat slab displaces the hot mantle wedge, leading to the cessation of arc volcanism and conductive cooling of the continental lithosphere by the presence of the cool oceanic plate (Dumitru et al., 1991; Wada and Wang, 2009; Currie and Hyndman, 2006). However, cooling through thermal conduction is a relatively slow process (Dumitru, 1990). The present-day flat slabs only achieved the horizontal geometries within the last 20 Ma (Ferrari et al., 1999; Yáñez et al., 2001; Hampel, 2002; Ramos et al., 2002; Rosenbaum et al., 2005). Therefore, it is unclear whether there has been sufficient time for the continent to cool. In this chapter, we use numerical models to assess temporal variations in the continental thermal structure during the development of a flat slab.

## **4.2 Methods**

The two-dimensional numerical models are based on Chapter 3. The thermal-mechanical evolution of the model is calculated using the finite-element code SOPALE

(Fallsack, 1995). It solves the equations of conservation of mass, force balance and energy balance, assuming plane strain and incompressibility (Fallsack, 1995).

The model domain is 3000 km wide and 660 km deep (Fig. 4.2), oriented parallel to the convergence direction. The Eulerian calculation mesh has elements with a horizontal width of 10 km and a height of 2 km for the top 90 km, 5 km for the middle 100 km, and 10 km for the bottom 470 km. Within the domain, we model subduction of an oceanic plate below a continental plate, where the trench position is located 400 km from the left boundary. Below, we report all distances with respect to the trench.

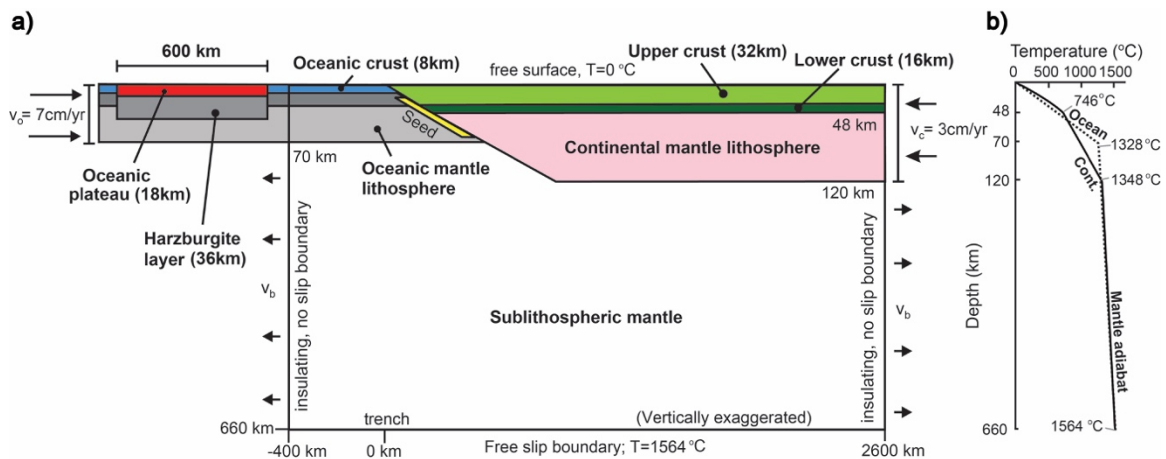


Figure 4.2. (a) Initial model geometry and boundary conditions. (b) Initial geotherms for the continental and the oceanic lithosphere.

The geometry of the reference model is based on the present-day subduction zones in South America. The oceanic plate has a 70 km thick lithosphere and a thermal structure consistent with a 30 Ma oceanic plate, which is based on the average oceanic plate age in the flat subduction regions in Mexico and South America (e.g. Müller et al., 2008; Quinteros and Sobolev, 2013). We include a 600 km wide oceanic plateau. Our modeled

plateau has an 18 km thick crust, corresponding to the average thicknesses of the ridges in Peruvian (the Nazca Ridge) and Pampean (the JFR) flat-slab regions (e.g., Woods and Okal, 1994; Yáñez et al., 2002; Gans et al., 2011). The adjacent normal oceanic crust is 8 km thick. Below the oceanic crust, there is a harzburgite layer that is twice the thickness of crust to represent melt-depleted mantle (van Hunen et al., 2004). For simplicity, we use a laterally uniform continental plate. In our reference model, we use a 48 km crustal thickness and a total lithosphere thickness of 120 km. In later models, we vary both the crustal and lithosphere thickness.

The material properties are given in Table 4.1, following values used in earlier studies (e.g., Beaumont et al., 2006; Liu and Currie, 2019). All materials undergo viscous-plastic deformation. The rheologies are based on laboratory experiments, and we apply a linear scaling factor ( $f$ ) to vary the effective viscosity in order to allow for strength variations relative to the laboratory materials (Beaumont et al., 2006). We also include frictional-plastic strain softening and viscous strain weakening to represent processes that cause a decrease in material strength during deformation, such as grain size changes (e.g. Beaumont et al., 2006). The exception is the continental crust which has a dry, strong continental crust without strain softening or weakening (Table 4.1), so that deformation is minimized, and the resulting thermal structure only depends on the effects of the flat slab. The continental upper crust has the viscous rheology of wet quartzite (Gleason and Tullis, 1995) with  $f=50$  and the lower crust has the viscous rheology of dry Maryland diabase (Mackwell et al., 1998) with  $f=1$ . The oceanic crust uses the dry Maryland diabase rheology with  $f=0.1$ . The oceanic and continental mantle lithosphere have the wet olivine rheology

(Karato and Wu, 1993) with  $f=10$  to approximate dry conditions. The sublithospheric mantle has the wet olivine rheology without any scaling ( $f=1$ ).

The thermal conductivity of all materials is  $2.25 \text{ W}/(\text{m}\cdot\text{K})$ , and the upper and lower continental crusts have radiogenic heat production of  $1.0$  and  $0.4 \mu\text{W}/\text{m}^3$ , respectively; there is no heat production for other materials (Jaupart and Mareschal, 2014). The density of all materials is temperature-dependent. The oceanic crust undergoes a phase change when the temperature and pressure conditions reach the eclogite stability field (Hacker et al., 2003). The phase change is included as an increase of the reference density from  $2950$  to  $3500 \text{ kg}/\text{m}^3$  with no other changes (e.g. rheology). Normal oceanic plate fully transforms to high-density eclogite, whereas the JFR oceanic plateau crust undergoes 30% eclogitization (reference density of  $3125 \text{ kg}/\text{m}^3$ ). This allows the plateau to remain buoyant enough to develop a flat slab; the assumption is that this region is relatively dry and therefore does not fully transform to eclogite (Liu and Currie, 2019). The amount of eclogitization does not change the flat-slab subduction dynamics as long as the plateau remains less dense than the shallow sublithospheric mantle (Liu and Currie, 2019).

Figure 4.2a shows the boundary conditions used in the models. The temperatures of the top and bottom boundaries are  $0$  and  $1564^\circ\text{C}$ , respectively. The bottom temperature is calculated based on a  $1300^\circ\text{C}$  mantle adiabat (vertical gradient of  $0.4^\circ\text{C}/\text{km}$ ). At the left boundary, the oceanic lithosphere has a geotherm that is consistent with a 30 Ma plate (Stein and Stein, 1992; Fig. 4.2b). The side boundaries are insulated boundaries with no horizontal heat flux. The initial structure of the model is calculated based on these boundary conditions and the thermal properties of each material. This results in a continental geotherm (Fig. 4.2b) that is consistent with its 120 km thickness, with a surface heat flow

of  $57.4 \text{ mW/m}^2$ . In later sections, we vary the thickness and the associated thermal structure of the continental lithosphere. The top surface is a stress-free boundary that allows for topography development. The bottom boundary is a closed, free-slip boundary. The side boundaries are no-slip boundaries, and they have prescribed horizontal velocities to generate plate convergence.

The average convergence rate between the Nazca and South America Plates over the last 15 Ma was  $\sim 10 \text{ cm/yr}$  (Norabuena et al., 1999). In the model, the oceanic plate enters the model domain through the left boundary at  $7 \text{ cm/yr}$  ( $V_o$  in Fig. 4.2a). The continent has a trenchward motion of  $3 \text{ cm/yr}$  ( $V_c$ ), consistent with motion of South America relative to the deep mantle (Quinteros and Sobolev, 2013). To maintain mass balance of the model, a small outflux velocity ( $V_b$ ) is assigned to the side boundaries of the sublithospheric mantle. Models are solved in the continental reference frame, and therefore  $V_c$  is added to all side boundaries (Liu and Currie, 2016).

Models are run in three phases as shown in Chapter 2. In the first two phases, the models undergo isostatic adjustment and subduction initiation for 500 km plate convergence. At the end of phase two, the oceanic plateau is located at the trench with a normal-angle subduction zone. Phase three starts at this point (the 0 Myr panel of Fig. 4.3) and all times are reported relative to this time. Models are run for 30 Myr in phase three to study flat-slab subduction over this timeframe, but we note that the Pampean flat slab at its current latitude only initiated in the last 11 Ma (Yáñez et al., 2001) and the development of Peruvian flat slab began  $\sim 11 \text{ Ma}$  (Hampel, 2002). In phase three, we examine different parameters to test their effects on the continental thermal structure. All models are listed in Table 4.2.

Table 4.1. Model parameters.

	Oceanic crust	Oceanic mantle lithosphere	Cont. upper crust	Cont. lower crust	Cont. mantle lithosphere	Sub-lithospheric mantle
<b>Plastic rheology *</b>						
<b>C<sub>0</sub> (MPa)</b>	0	0	20	0	0	0
<b>φ<sub>eff</sub></b>	15° †	15°	30°	30°	15° †	15° †
<b>Viscous rheology §</b>						
<b>Material</b>	Dry Maryland diabase	Wet olivine	Wet quartzite	Dry Maryland diabase	Wet olivine	Wet olivine
<b>f</b>	0.1 #	10	50	1	10 #	1 #
<b>A<sub>ps</sub> (Pa<sup>-n</sup> s<sup>-1</sup>) **</b>	5.78×10 <sup>-27</sup>	1.76×10 <sup>-14</sup>	8.57×10 <sup>-28</sup>	5.78×10 <sup>-27</sup>	1.76×10 <sup>-14</sup>	1.76×10 <sup>-14</sup>
<b>B*(Pa<sup>-n</sup> s<sup>-1</sup>) **</b>	1.91×10 <sup>5</sup>	1.92×10 <sup>4</sup>	2.92×10 <sup>6</sup>	1.91×10 <sup>5</sup>	1.92×10 <sup>4</sup>	1.92×10 <sup>4</sup>
<b>n</b>	4.7	3.0	4.0	4.7	3.0	3.0
<b>Q (kJ mol<sup>-1</sup>)</b>	485	430	223	485	430	430
<b>V* (cm<sup>3</sup> mol<sup>-1</sup>)</b>	0	10	0	0	10	10
<b>Thermal parameters</b>						
<b>k (Wm<sup>-1</sup> K<sup>-1</sup>) ††</b>	2.25	2.25	2.25	2.25	2.25	2.25
<b>Λ (μWm<sup>-3</sup>)</b>	0	0	1.0	0.4	0	0
<b>c<sub>p</sub> (J kg<sup>-1</sup> K<sup>-1</sup>)</b>	750	1250	750	750	1250	1250
<b>α (K<sup>-1</sup>)</b>	3.0×10 <sup>-5</sup>	3.0×10 <sup>-5</sup>	3.0×10 <sup>-5</sup>	3.0×10 <sup>-5</sup>	3.0×10 <sup>-5</sup>	3.0×10 <sup>-5</sup>
<b>Density §§</b>						
<b>ρ<sub>0</sub> (kg m<sup>-3</sup>)</b>	2950	3250	2800	2900	3250	3250
<b>T<sub>0</sub> (°C)</b>	0	1344	200	500	1344	1344
<b>Eclogite ρ<sub>0</sub> (kg m<sup>-3</sup>)</b>	3500	—	—	—	—	—
<b>Eclogite T<sub>0</sub> (°C)</b>	0	—	—	—	—	—
* Frictional-plastic deformation uses the Drucker-Prager yield criterion: $(J'_2)^{1/2} = P \sin \phi_{eff} + C_0 \cos \phi_{eff}$ , where $J'_2$ is second invariant of the deviatoric stress tensor, P is pressure, $\phi_{eff}$ is effective internal angle of friction, and $C_0$ is cohesion.						
† Softens through a decrease in $\phi_{eff}$ from 15° to 2° over accumulated strain of 0.5 to 1.5 (Beaumont et al., 2006).						
§ Effective viscosity: $\eta_{eff} = f(B^*) \dot{\gamma}'_2^{\frac{1-n}{2n}} \exp\left[\frac{Q+PV^*}{nRT}\right]$ , where $\dot{\gamma}'_2$ is the second invariant of the strain rate tensor, f is a scaling factor, R is the gas constant, and B*, n, Q and V* are the pre-exponential viscosity parameter, stress exponent, activation energy and activation volume, respectively.						
# Weakening through a decrease in f by a factor of 10 over accumulated strain of 2.0 to 5.0 (Warren et al., 2008).						
** $B^* = \frac{1}{2} A_{ps}^{-1/n}$ . $A_{ps}$ is the plane strain pre-exponential factor that converted from uniaxial laboratory experimented pre-exponential viscosity parameter ( $A_{uni}$ ). $A_{ps} = \frac{1}{2} (3^{(n+1)/2}) A_{uni}$ .						
†† Thermal conductivity at temperatures <1396°C; above this, thermal conductivity increases linearly to 54.25 Wm <sup>-1</sup> K <sup>-1</sup> at 1436°C (Pysklywec and Beaumont, 2004).						
§§ Temperature dependent density: $\rho(T) = \rho_0[1 - \alpha(T - T_0)]$ , where $\rho_0$ is the reference density at temperature $T_0$ and $\alpha$ is the volumetric thermal expansion coefficient.						

## 4.3 Results

### 4.3.1 Reference model

We first present the reference model, which has an initial continental lithosphere thickness of 120 km and continental crustal thickness of 48 km. Figure 4.3 shows the model evolution from 0 to 20 Myr. The models are run for an additional 10 Myr in which the slab maintains a flat geometry with the edge of the slab reaching  $\sim 2800$  km. At 0 Myr, the oceanic plateau enters the trench. At this time, the subduction zone has a normal-angle slab and a hot mantle wedge. We expect that this would lead to a volcanic arc  $\sim 200$  km from the trench (Fig. 4.4a), based on where the mantle wedge temperature is  $>1200^\circ\text{C}$  (e.g. Schmidt and Poli, 1998). The Moho temperature and surface heat flow are high near the putative arc due to mantle wedge corner flow (Fig. 4.4a). In the forearc region ( $<100$  km from trench), the cool oceanic plate is in contact with the continent at shallow depth ( $<50$  km), the surface heat flow is  $<40$  mW/m<sup>2</sup>, which is consistent with observations in forearc regions (e.g. Wada and Wang, 2009).

As the oceanic plateau enters the trench, it remains buoyant relative to the mantle. This causes a decrease in subduction angle. Owing to the density contrast between the oceanic plateau and the oceanic plate that has already subducted, the slab undergoes a break-off at  $\sim 5$  Myr. With continued plate convergence, the buoyant oceanic plateau causes the slab to form a flat-slab geometry beneath the continental lithosphere at 90-100 km depth.

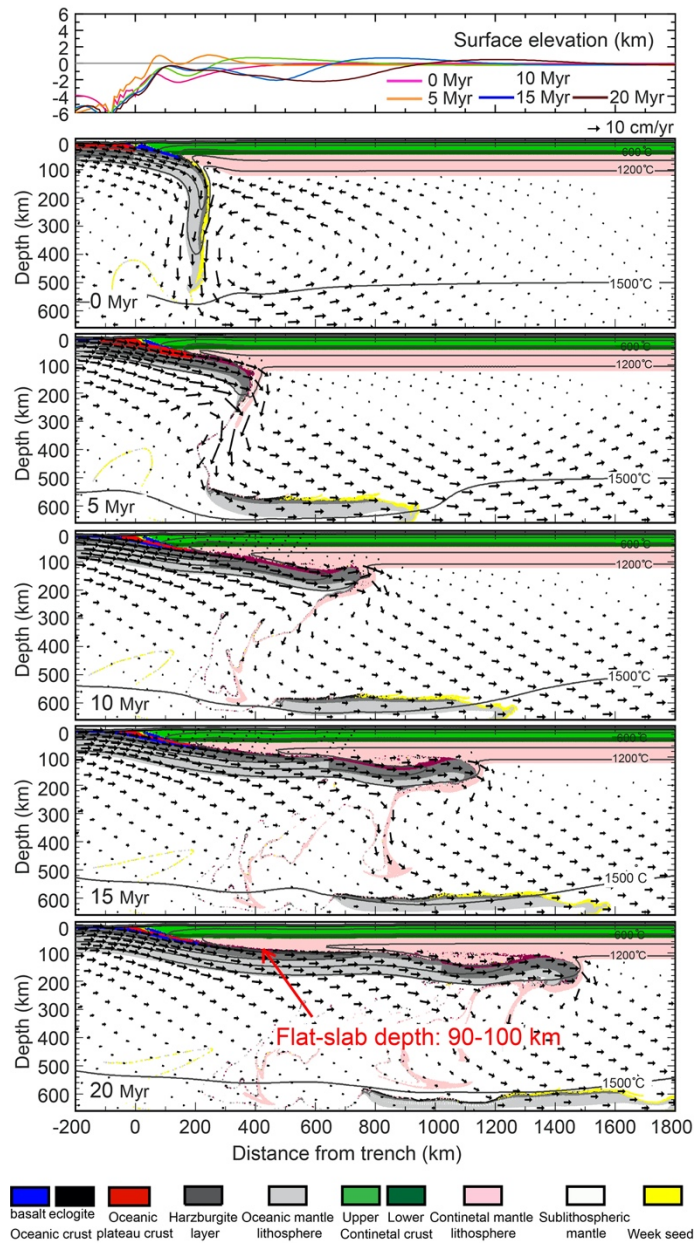


Figure 4.3. Reference model evolution from 0 to 20 Myr with surface elevation. Black arrows show the velocity field of the model. The material colors follow those in Figure 4.2a and eclogite is marked by the dark red color.

As the slab flattens, we expect a cessation of arc volcanism as the hot mantle wedge is displaced. The presence of the flat slab results in a rapid cooling in the regions near the predicted arc (~200 km from the trench). The Moho temperature decreases over 200°C and

the surface heat flow decrease over  $15 \text{ mW/m}^2$  by 20 Myr (Fig. 4.4a). The magnitude of cooling becomes smaller farther into the continental interior.

Figure 4.4b shows the vertical temperature profile at 400 km from the trench at 0, 10, 20, and 30 Myr. The flat slab reaches this location at  $\sim 5$  Myr and the slab depth is  $\sim 90$  km. After the slab is in contact with the continental lithosphere, the continent cools through thermal conduction. The lowermost continent cools first and has a greater amount of cooling during the model run compared to shallower regions. Figure 4.4c shows the geothermal gradient near the ground surface (upper 2 km). For the first 20 Myr, the surface geothermal gradient has a relatively constant value of  $24.1^\circ\text{C/km}$  and then decreases to  $\sim 23.5^\circ\text{C/km}$  over the next 10 Myr, with small fluctuations that appear to be due to minor crustal deformation and topographic changes. The near-surface thermal structure is not immediately affected by the presence of a flat slab and there is  $\sim 15$  Myr delay after the flat-slab emplacement at 5 Myr. This delay reflects the time needed for conductive cooling to propagate from the slab to the shallow crust.

To compare the lateral variations in continental thermal structure over time, we plot the Moho temperature (Fig. 4.4d) at three locations (400, 600, and 800 km from the trench). The flat slab reaches the three locations at 5, 8, and 11 Myr, and the Moho temperature starts to decrease from its initial value of  $745^\circ\text{C}$  at 13, 16, and 19 Myr, with later times for positions further from the trench. This shows that the onset of cooling at the Moho has a delay of  $\sim 8$  Myr following flat-slab emplacement. By the end of the 30 Myr model run, the Moho temperatures have decreased by approximately 77, 28, and  $15^\circ\text{C}$  at 400, 600, and 800 km, respectively. In all locations, the flat-slab depth is approximately the same and therefore the greater amount of cooling closer to the trench is primarily due to the earlier

flat-slab emplacement and, therefore longer cooling time. A secondary effect is that the slab temperature is lower below this region. The slab surface temperature increases by  $\sim 100^{\circ}\text{C}$  every 100 km inboard (Fig. 4.4a).

Figure 4.4e shows the temporal changes in surface heat flow at 400, 600, and 800 km from the trench. This is determined based on the near-surface thermal gradient and the thermal conductivity ( $2.25 \text{ W}/(\text{m}\cdot\text{K})$ ). The initial surface heat flow is  $57.4 \text{ mW}/\text{m}^2$  and the decreases of surface heat flow are 1.5, 0.4,  $0.2 \text{ mW}/\text{m}^2$  over 30 Myr at 400, 600, and 800 km from the trench, respectively (Fig. 4.4e). This change in heat flow is well below the uncertainties in heat flow measurements (Lewis et al., 2003), and it is unlikely that this could be resolved in observations.

In the following sections, we vary model parameters to examine the effect on the continental thermal structure. To compare the results, we report the Moho temperature and surface heat flow at 400 km from the trench (blue dotted line in Fig. 4.4a), as this position is in the continental interior where observations show low surface heat flow (Fig. 4.1).

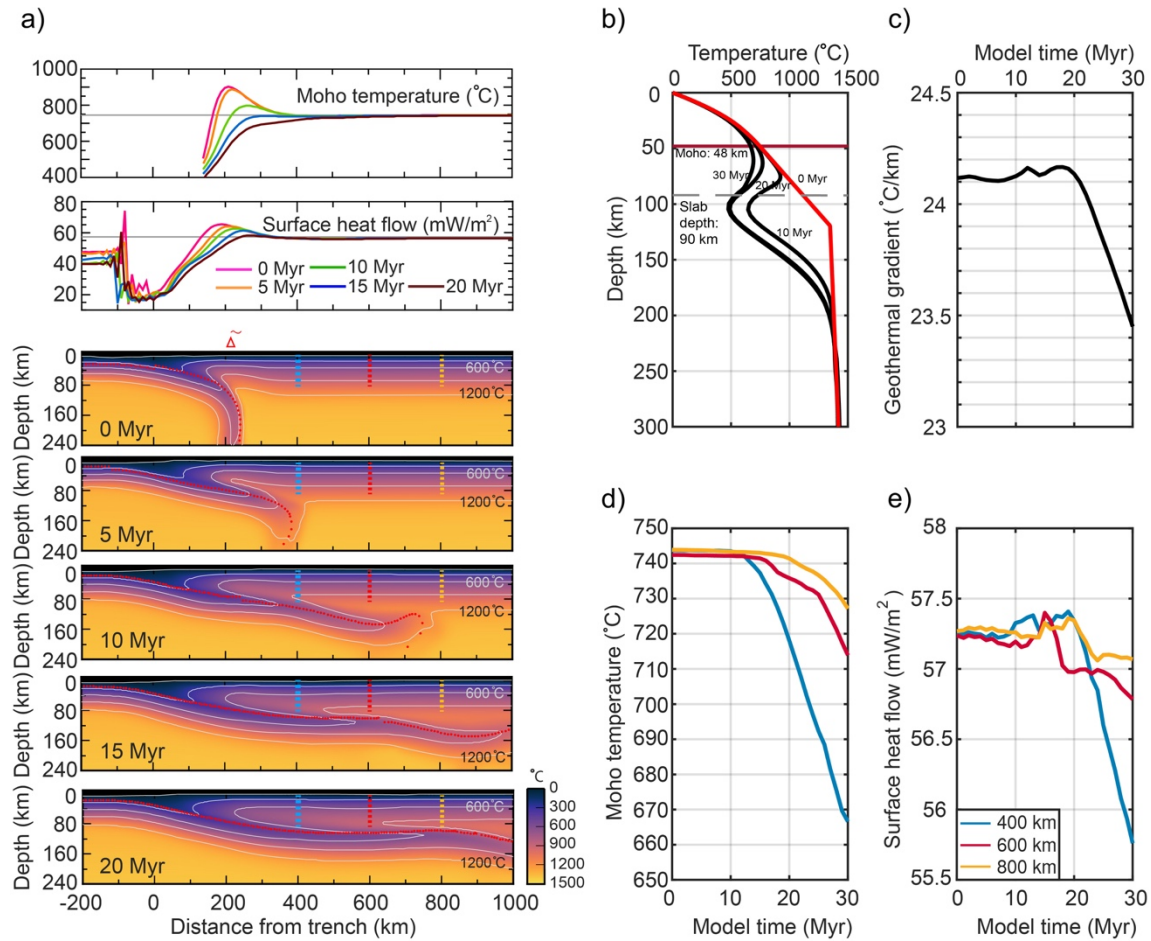


Figure 4.4. Thermal evolution of the reference model. (a) Model temperature field at given times with Moho temperature (top plot) and surface heat flow (second plot). Gray lines indicate the initial values for the continental region. In the model plots, white lines are isotherms every  $300^{\circ}\text{C}$  and red lines are the oceanic Moho. Blue, red, and yellow dotted lines are at 400, 600, and 800 km. (b) Vertical temperature profile at 400 km from the trench; the red line is the initial continental geotherm. (c) Surface geothermal gradient at 400 km. (d) Moho temperature and (e) surface heat flow over time at three positions from the trench (400, 600, and 800 km).

### 4.3.2 Effect of subduction angle

To demonstrate the effect of subduction geometry on continental thermal structure, we present a model that maintains a normal (steep) subduction angle throughout the 30 Myr model run. This model uses the same parameters as the reference model except that

the oceanic plateau crust undergoes 100% eclogitization, such that it becomes negatively buoyant and no flat slab develops.

Figure 4.5a shows the model evolution. The normal-angle slab results in the persistent presence of mantle wedge with a temperature  $>1200^{\circ}\text{C}$  above a slab depth of 100 km. Thus, we expect that there would be a continuous magmatic arc  $\sim 200$  km from the trench. In the forearc ( $<150$  km), the Moho temperature and surface heat flow are below the initial values due to cooling from the subducting plate. At distances of 150 to 350 km, the continent is heated by mantle wedge flow, and the Moho temperature and surface heat are higher than the initial values, with the peaks at 200 km ( $950^{\circ}\text{C}$  Moho and  $\sim 65$   $\text{mW}/\text{m}^2$  heat flow).

Figures 4.5b and 4.5c compare the models with normal-angle and reference flat-slab subduction at 400 km. The normal-angle subduction model has negligible changes in the continental Moho temperature and surface heat flow during the 30 Myr model run. This contrasts with the flat-slab model in which the Moho temperature decreases by  $77^{\circ}\text{C}$  and surface heat flow decreases by  $1.5$   $\text{mW}/\text{m}^2$ . This shows that the continental cooling in the reference model results from the presence of the flat slab.

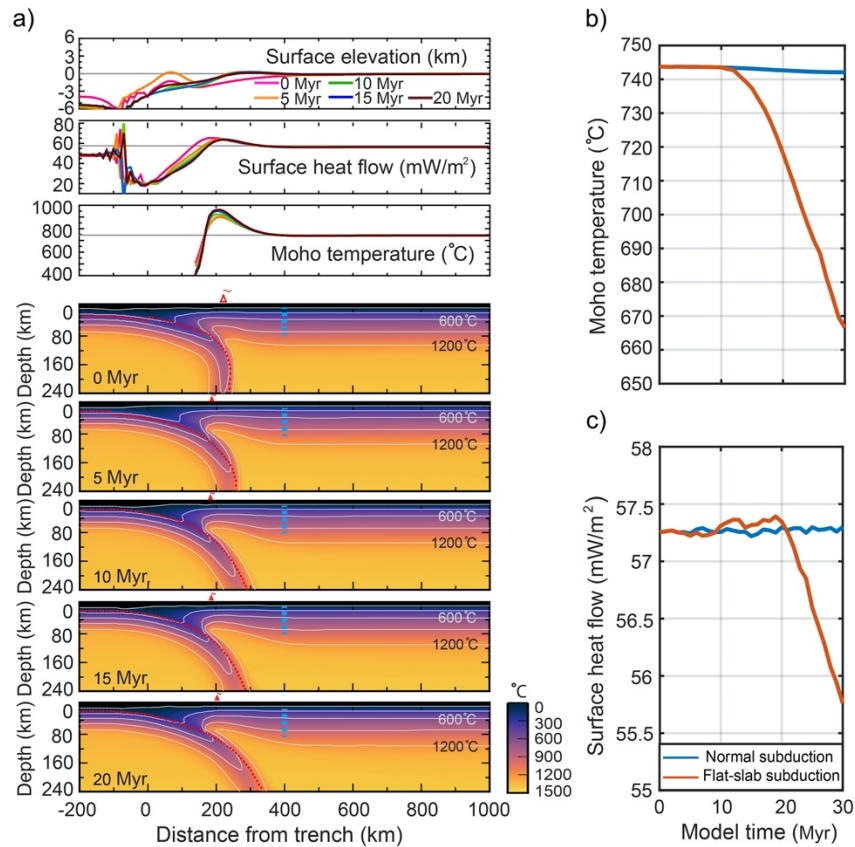


Figure 4.5. Normal-angle subduction model. (a) Model temperature field evolution with surface topography, surface heat flow, and Moho temperature; white lines are isotherms every 300°C; red lines are the oceanic Moho. Temporal changes in (b) Moho temperature and (c) surface heat flow of the normal subduction model (blue line) and flat-slab subduction model (Fig. 4.4a; orange line) at 400 km from the trench.

### 4.3.3 Variations in thickness of initial continental lithosphere and flat-slab depth

In this section, we examine variations in initial continental thickness. As we showed in Chapter 3, the flat-slab depth is primarily controlled by the initial continental thermal structures, owing to the temperature-dependent rheology of mantle lithosphere. As a slab flattens, it is able to displace the lowermost continental mantle lithosphere with temperatures >900°C. The flat-slab depth increases for thicker continents, as these regions

are cool and thus there is a thicker portion of the lithosphere that is too strong to be displaced.

We present models with initial continental thicknesses of 80 km, 120 km (reference model), and 160 km. These variations result in differences in the initial thermal structure, with Moho temperatures of 930, 745, and 680°C and surface heat flows of 65, 57.4, and 54.1 mW/m<sup>2</sup> for models with 80, 120 and 160 km thick continent, respectively. The general evolution of all models is the same, with slab flattening induced by subduction of the oceanic plateau. The main difference is the flat-slab depth. At 400 km from the trench, the flat slabs are at depths of 60, 90, 115 km, with a deeper slab for a thicker continental plate (Fig. 4.6a). Figure 4.6b shows the geotherms of the three models at 400 km over the 30 Myr model run.

To compare the three models, we plot the Moho temperature change and surface heat flow change at 400 km (Figs. 4.6c and 4.6d), relative to the initial values for each model. The flat slab reaches this position at 5 Myr in all models. For the thinnest continent (80 km thick), the Moho temperature starts to decrease at ~8 Myr and drops by ~450°C by 30 Myr. In contrast, the 120 and 160 km continents experience a Moho temperature decrease of 77°C and 31°C starting at 13 and 16 Myr, respectively. Therefore, the times between flat slab emplacement (5 Myr) and onsets of cooling are 3, 8, and 11 Myr for the three models, with the shortest time for thinnest continent (shallowest flat slab). For the 80 km continent, the surface heat decreases by ~18 mW/m<sup>2</sup> by 30 Myr, starting at ~12 Myr (7 Myr after flat-slab emplacement), whereas the surface heat flow drops by 1.5 and 0.5 mW/m<sup>2</sup> for the 120 km and 160 km continents, respectively, starting at >20 Myr.

These models demonstrate that the flat-slab depth strongly affects the continental cooling. A shallower flat slab leads to both an earlier onset and a greater amount of cooling of the overlying continent because conductive cooling due to the slab transfers through a thinner layer of lithosphere (Dumitru et al., 1991).

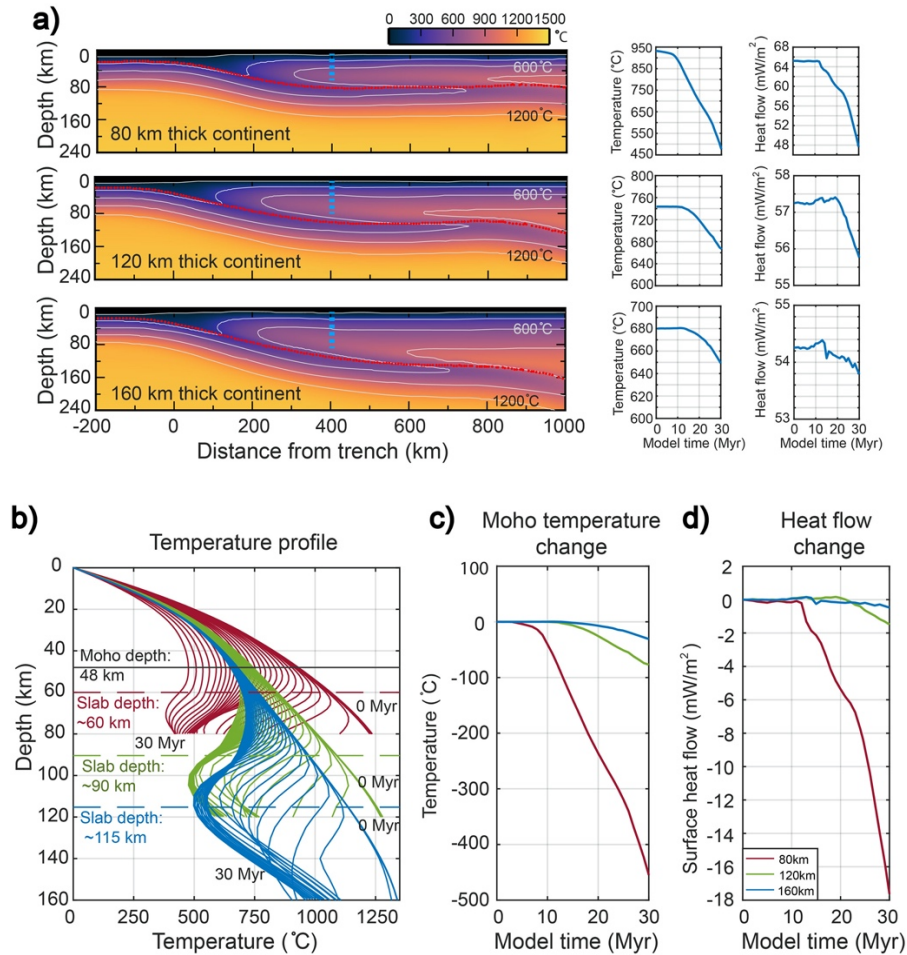


Figure 4.6. (a) Temperature fields at 20 Myr for models with 80, 120, and 160 km thick continents. Note that the flat-slab depth increases with increasing initial continental thickness. The plots on the right show the temporal changes in Moho temperature and surface heat flow of the corresponding model. (b) Geotherm profiles from 0 Myr to 30 Myr with an interval of 1 Myr; red line, green line, and blue lines represent models with 80, 120, and 160 km thick continents, respectively. Temporal changes in (c) Moho temperature and (d) surface heat flow relative to the initial values for the three models at 400 km from the trench.

#### 4.3.4 Effects of other factors

This section presents models that examine variations in thermal conductivity, continental crustal thickness, convergence rate, and oceanic plate age. The models are based on the reference model, and only the tested parameter is different from the reference value. In all models, the development of a flat slab is similar to the evolution of the reference model (Fig. 4.3).

##### **4.3.4.1 Thermal conductivity**

Thermal conductivity controls the rate of conductive heat transfer (Turcotte and Schubert, 2002). The thermal conductivity of lithosphere rocks ranges from 1.5 to 7 W/(m·K) depending on the rock composition and temperature, with higher values for cool and mafic rocks (Clauser and Huenges, 1995). We have tested thermal conductivities of 2.25 (reference value), 3.25, 4.25, and 5.25 W/(m·K), where this value is applied to the entire continental lithosphere (crust and mantle). All models have the same lithosphere thickness (120 km), but the variation in conductivity results in different initial thermal structure (Fig. 4.7). Models with higher thermal conductivity have lower lithospheric temperatures so that all models have the same temperature at 120 km depth (i.e., 1348°C, the mantle adiabat at this depth). As a result, these models have different flat-slab depths. The slab depths are 90, 97, 105, and 110 km, with deeper slabs for a higher thermal conductivity due to the lower temperature and thus stronger lithosphere.

Figure 4.7a shows the temporal variation in absolute Moho temperature at 400 km from the trench, as well as the difference relative to the initial value. The initial slab emplacement at this location is the same (5 Myr). The model with highest thermal conductivity has a Moho temperature decrease of 103°C by 30 Myr, compared to a decrease

of  $77^{\circ}\text{C}$  for the reference model with the lowest conductivity. The onset of Moho cooling occurs up to 5 Myr earlier as the thermal conductivity increases. Figure 4.7b shows that the surface heat flow changes of the four models decreases by as much as  $3.5\text{ mW/m}^2$ , with the largest decrease for models with higher thermal conductivity. These results show that continental cooling is enhanced by a higher thermal conductivity, as the cool slab temperatures are more efficiently transferred through the continent, even though the slab is at a larger depth.

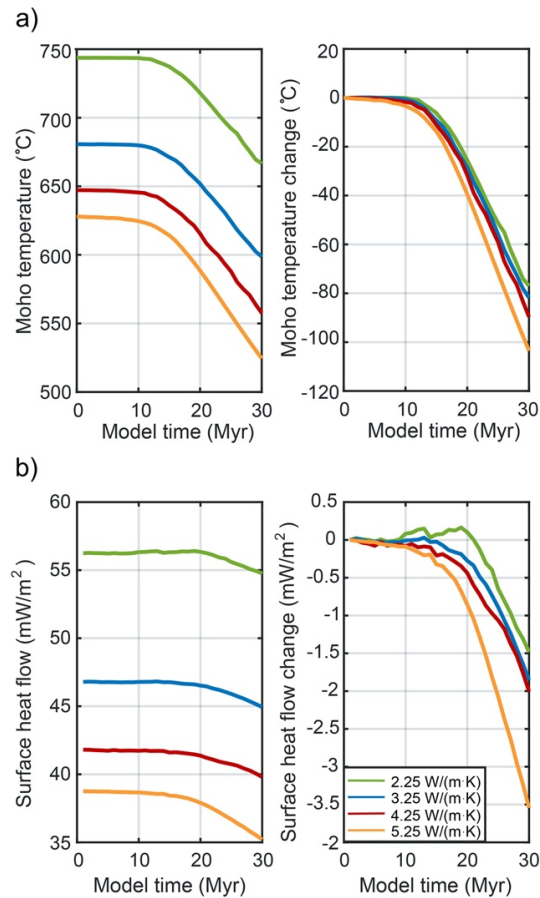


Figure 4.7. Numerical model results with different thermal conductivities. The green line, blue line, red line, and yellow line represent models with conductivities of 2.25 (reference model), 3.25, 4.25, and 5.25  $\text{W}/(\text{m}\cdot\text{K})$ , respectively. (a) Moho temperature and Moho temperature change relative to the initial value. (b) Surface heat flow and heat flow change relative to the initial value.

#### 4.3.4.2 *Continental crust thickness*

We test models with continental crustal thicknesses of 36, 42, and 48 km (reference model), where the upper crust thickness is twice that of the lower crust. The radiogenic heat productions are 1.0 and 0.4  $\mu\text{W}/\text{m}^3$  for the upper crust and lower crust, respectively. All models have the same continental lithosphere thickness of 120 km. Figure 4.8a shows the Moho temperature and temperature changes over the 30 Myr model run at 400 km from the trench. The model with the thinnest crust (36 km) has the coolest initial Moho temperature (538°C), and the flat slab causes the Moho temperature to decrease starting at 17 Myr (12 Myr after slab emplacement), with an overall decrease of  $\sim 13^\circ\text{C}$  by 30 Myr. In contrast the reference models with a 48 km crust, experiences Moho cooling starting at 13 Myr (8 Myr after slab emplacement), reaching  $77^\circ\text{C}$  by 30 Myr. The earlier onset and greater magnitude of cooling for a thicker crust occur because the Moho is closer to the cool flat slab. The surface heat flow decrease for all crustal thicknesses is similar to that seen in the reference model ( $\sim 1.5 \text{ mW}/\text{m}^2$ ) and therefore we do not show it here.

#### 4.3.4.3 *Convergence rate*

In the Pampean flat-slab region, the convergence rate between the Nazca Plate and South America plate has slowed from 10 to 7 cm/yr in the Neogene (Quinteros and Sobolev, 2013). Here, we present a model with a convergence rate of 7 cm/yr, for comparison to the reference model (10 cm/yr). With the slower convergence rate, the flat slab reaches 400 km from the trench at  $\sim 7$  Myr, compared to 5 Myr for the reference model, but the overall slab dynamics are similar. Figure 4.8b shows the temporal changes in Moho temperature

of the two models at 400 km from the trench. Both models experience Moho cooling, starting  $\sim 8$  Myr after flat-slab emplacement. By 30 Myr, the model with slower convergence has a Moho temperature decrease of  $50^{\circ}\text{C}$  and a surface heat flow decrease of  $0.7 \text{ mW/m}^2$ . These changes are lower than those in the reference model ( $77^{\circ}\text{C}$  and  $1.5 \text{ mW/m}^2$ ), showing that the cooling rate is enhanced when the convergence rate is higher. As both models have a similar flat-slab depth (90 km), the cooling appears to be caused by the fact that the faster slab is cooler.

#### **4.3.4.4 Oceanic plate age**

The age of the oceanic plate controls the thermal state of the oceanic lithosphere, with a cool and thick lithosphere for an older plate (e.g. Stein and Stein, 1992). The previous models use a young oceanic plate (30 Ma) that represents the young flat-subducting plates in Mexico and South America (e.g. Müller et al., 2008). The Farallon flat slab in the Cretaceous western US had a 100 Ma oceanic plate (Usui et al., 2003). To show the effect of subducting plate age on the continental thermal structure, we test a model with an oceanic plate age of 100 Ma. This oceanic plate has a thickness of 90 km, based on the GDH1 plate cooling model (Stein and Stein, 1992). Figure 4.8c shows the continental Moho temperature over the 30 Myr model run for these models. In both models, the Moho temperature starts to decrease  $\sim 8$  Myr after flat slab emplacement. With an old oceanic plate, the Moho temperature decreases by  $105^{\circ}\text{C}$  at 30 Myr, which is larger than that for the young oceanic plate ( $77^{\circ}\text{C}$ ). Both models have the same convergence rate and flat-slab depth, and therefore the difference is due to the oceanic plate temperatures. With an older

plate, the flat slab is cooler, and this results in a higher cooling rate, as seen with the greater slope on Figure 4.8c.

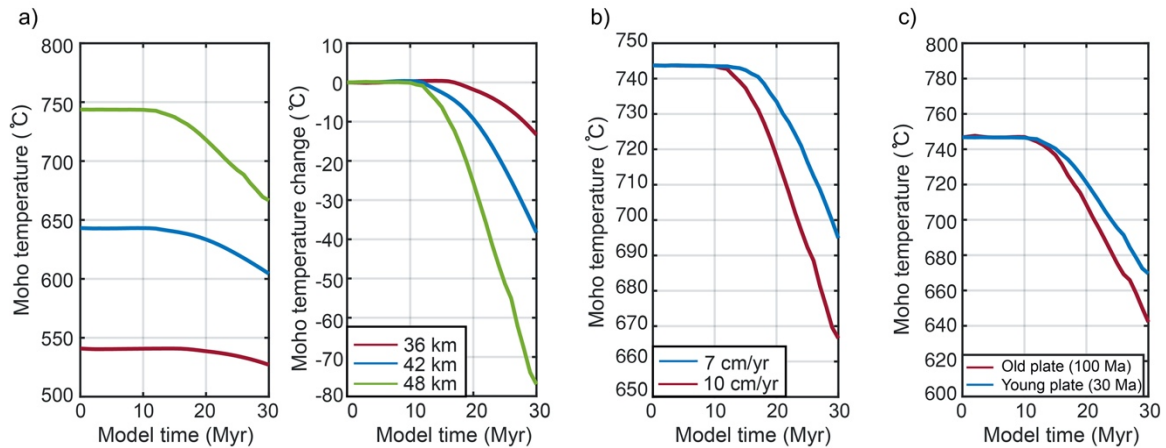


Figure 4.8. (a) Moho temperature and temperature change relative to the initial value for models with continental crustal thicknesses of 36, 42, and 48 km. (b) Moho temperature of models with fast (10 cm/yr) and slow (7 cm/yr) convergence rates. (c) Moho temperature of models with old (100 Ma) and young (30 Ma) oceanic plates.

## 4.4 Discussion

### 4.4.1 Summary of numerical models

The thermal-mechanical models allow us to examine the temporal changes in continental thermal structure during flat-slab subduction. Table 4.2 summarizes the results. The model with normal-angle subduction does not show a significant change in back-arc thermal structure over the 30 Myr model run. All models with a flat slab show some continental cooling over time. In these models, the emplacement of a cool flat slab beneath the continent displaces the hot mantle wedge. The cold slab is in contact with the continent and cools the overlying lithosphere through thermal conduction. The cooling has a greater impact on areas closer to the trench (Figs. 4.4 and 4.5), as the flat slab reaches these areas

earlier, and therefore there is a longer cooling time. A secondary effect is that the slab has lower temperature in this region. The bottom of the continental lithosphere is most affected by the flat slab because it is closest to the cool slab surface and cools first. Similarly, the continental Moho temperature starts to decrease before near-surface temperatures, and the overall magnitude of cooling is larger at the Moho, especially for models with a thick crust (Fig. 4.8a).

The main factor that controls the cooling of the continent is the flat-slab depth (Fig. 4.6). With a shallower flat slab, the continental crust experiences an earlier onset and greater magnitude of cooling compared to deeper slabs. Thus, less time is needed for reduced temperatures to be observed at the surface (Dumitru et al., 1991). Other parameters have a second-order influence on the continental thermal structure. Higher thermal conductivity, faster convergence rates, and older oceanic lithosphere result in slightly greater cooling by either increasing the heat transfer rate or decreasing the slab temperature.

Table 4.2. List of models and the change in Moho temperature and surface heat flow.

Model feature	Moho temperature decrease (°C)	Onset of Moho cooling after flat-slab emplacement (Myr)	Surface heat flow decrease (mW/m <sup>2</sup> )	Flat-slab depth (km)	Figure #
<b>Location from the trench (400 km)</b>				90	4.4
400 km ( <i>reference model</i> )	77	~8	1.5		
600 km	28	~8	0.4		
800 km	15	~8	0.15		
<b>Geometry of slab (flat slab)</b>				N/A	4.5
Normal angle	~0	N/A	~0		
<b>Continental thickness (120 km)</b>					4.6
80 km	450	~3	18	60	
160 km	31	~11	0.5	115	
<b>Thermal conductivity (2.25 Wm<sup>-1</sup>K<sup>-1</sup>)</b>					4.7
3.25 Wm <sup>-1</sup> K <sup>-1</sup>	81	~6	1.8	97	
4.25 Wm <sup>-1</sup> K <sup>-1</sup>	89	~5	2	105	
5.25 Wm <sup>-1</sup> K <sup>-1</sup>	103	~3	3.5	110	
<b>Continental crust thickness (48 km)</b>					
36 km	13	~12	0.3	90	4.8a
42 km	39	~9	0.8	90	4.8a
<b>Convergence rate (10 cm/yr)</b>					
7 cm/yr	48	~8	0.7	90	4.8b
<b>Oceanic plate age (30 Ma)</b>					
100 Ma	106	~8	0.8	90	4.8c

*Note:* The measurements are taken at 400 km from the trench at 30 Myr. The reference model parameters are shown in brackets.

#### 4.4.2 Limitation of the numerical models

All the models presented in this work are in 2D, and therefore they do not allow an assessment of along strike variation in slab dip and thermal structure. In a 3D flat-slab subduction setup, if a tear occurs at the edge of the flat segments, mantle flow around the slab edge may bring hot asthenosphere into contact with the continent, leading to heating (e.g., Hu and Liu, 2016; Martinod et al., 2005). The heat may also conductively transfer

laterally into the flat-slab region and may slow the cooling process of this region by the flat slab.

We also note that in our models, a flat slab develops after the break-off of the dense slab in front of the oceanic plateau (Fig. 4.3). Other models of flat-slab subduction show that a flat slab can develop without a break-off, such that there is a continuous slab with a steep section ahead of the flat segment (e.g. van Hunen et al., 2004; Liu and Currie, 2016). Seismic tomography studies of modern flat-slab regions (Mexico, Peru, and Pampea) show that the geometry may be continuous (Kim et al., 2012; Scire et al., 2016; Portner et al., 2017), although a slab gap is observed below the southern part of the Pampean flat slab (Portner et al., 2017). With a continuous slab, slab flattening is accompanied by an inboard migration of the hot mantle wedge corner. This may result in a migration of the volcanic arc, where magmatism could cause enhanced heating of the shallow continent for a few Myr following flat-slab emplacement. This would make the continent hotter than we have assumed here, delaying slab cooling. Alternately, as the flat slab advances, the mantle wedge may be filled by continental mantle lithosphere that is displaced by the flat slab, fully terminating magmatism (Axen et al., 2018). Future models that include magmatism are needed to assess these effects.

#### 4.4.3 Timescale for continental cooling

To assess the timescale for continental cooling and to explore a greater range of parameters, we present 1D temperature calculations. These solve the time-dependent heat conduction equation using the conservative finite difference method (Gerya, 2019). The initial 1D temperature structure of the continent is given by a geotherm based on the

assumed continental thickness, using the same thermal parameters as the numerical models (Table 4.1). A cool flat slab is emplaced at a prescribed depth and with a constant temperature. The resulting thermal structure for the overlying material is then calculated for a longer time of 60 Myr compared to the 30 Myr in the 2D numerical models. This encompasses the long-lived flat slabs below the Late Cretaceous-Eocene western United States (40 Ma; e.g., Copeland et al., 2017) and Mesozoic South China (60 Ma; e.g. Li and Li, 2007).

Figure 4.9a shows the evolving 1D thermal structure for a 120 km thick continent with a 600°C slab at 90 km depth, based on the reference numerical model at 400 km from the trench (Fig. 4.3). Owing to the low-temperature slab, the continent starts to cool, with the greatest cooling in the deep lithosphere. Figures 4.9b and 4.9c show the temporal changes in surface heat flow and Moho temperature. The Moho temperature starts to decrease 8 Myr after emplacement of the flat slab, and cools by 200°C at 60 Myr. In contrast, the surface heat flow starts to decrease at 17 Myr and drops by ~10 mW/m<sup>2</sup> at 60 Myr. The Moho temperature and surface heat flow variations from the 1D calculations agree well with those of the reference numerical model. If the 1D calculations were run for longer, the geotherm would reach steady-state conditions (dashed lines on Fig. 4.9), with surface heat flow and Moho temperature of 45 mW/m<sup>2</sup> and 479°C, respectively.

Based on Fig. 4.9, continental cooling can be divided into three stages that are defined by two critical times,  $\tau_1$  (the lag time) and  $\tau_c$  (the cooling time or thermal time constant). In the early stages of the flat slab (at times less than  $\tau_1$ ) the thermal structure of the continent retains its initial values. At time  $\tau_1$ , conductive cooling starts to decrease the temperature. This marks the start of the second stage, where temperatures are determined

by both the initial continental structure and the flat-slab depth and temperature. In the third stage (at times greater than  $\tau_c$ ), the continental cooling approaches the steady-state values, and the temperatures are dominated by the effect of the flat slab.

The critical times indicate when the thermal effects of the flat slab should be first observed ( $\tau_l$ ) and the timeframe needed for significant cooling to occur ( $\tau_c$ ). We can quantitatively determine  $\tau_l$  and  $\tau_c$  based on the variations in thermal structure relative to the initial and final conditions. The relative change (R) in thermal structure as a function of time is given by:

$$R(t) = \frac{X(t) - X_0}{X_S - X_0}, \quad (4.1)$$

where X is the measured thermal parameter (Moho temperature or surface heat flow),  $X_0$  is the initial value, and  $X_S$  is the final (steady-state) value. The lag time ( $\tau_l$ ) is defined as the time at which the temperature field has changed by e% (e = Euler's number):

$$R(\tau_l) = 2.7\%. \quad (4.2)$$

Following Turcotte and Schubert (2002), the thermal time constant ( $\tau_c$ ) is the time at which:

$$R(\tau_c) = 1 - \frac{1}{e} = 63.2\%. \quad (4.3)$$

For the reference model (Fig. 4.9), the lag time ( $\tau_l$ ) occurs at 8.3 Myr for the Moho temperature and 16.7 Myr for the surface heat flow. The thermal time constant ( $\tau_c$ ) is 46.8 Myr for the Moho temperature, and 59.3 Myr for the surface heat flow. The longer timescales for the surface heat flow are due to the fact that the ground surface is further from the slab.

For comparison, we show the thermal evolution for a 90 km-deep slab with slab temperatures of 400°C and 800°C (blue and green dotted lines in Figs. 4.9b and 4.9c). Note that  $\tau_l$  and  $\tau_c$  are the same as the model with a 600°C slab because the slab is at the same depth in all models. However, at times greater than  $\tau_l$ , the temperatures depend on the slab temperature. When the slab is 400°C, the Moho cools by an extra ~80°C and the surface heat flow decreases by an extra 3 mW/m<sup>2</sup> over 60 Myr compared to the reference 600°C slab. This is consistent with the greater cooling observed in models that had an older oceanic plate or faster convergence rate (Table 4.2).

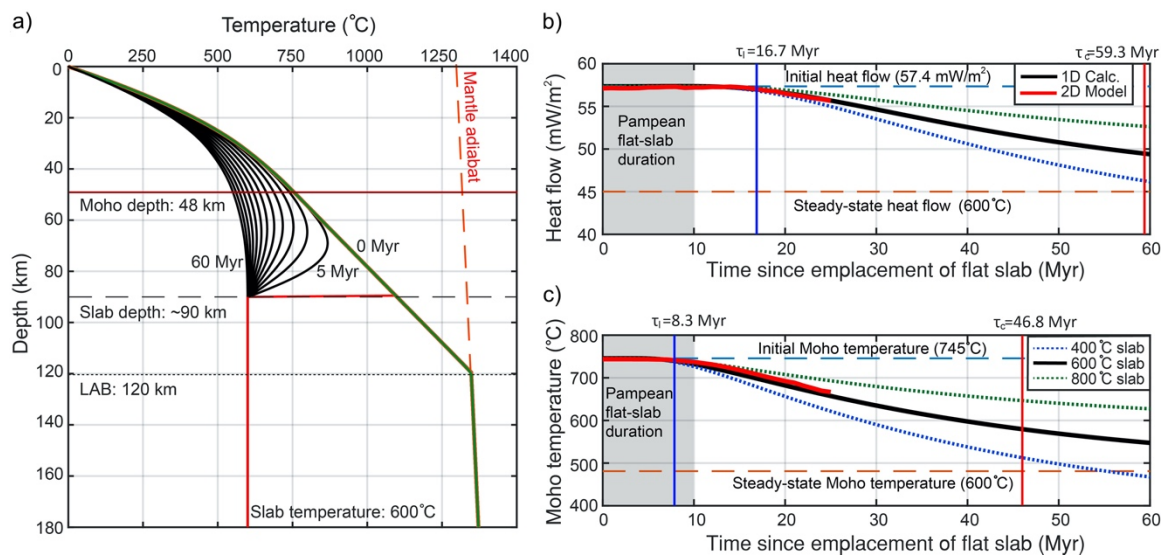


Figure 4.9. 1D time-dependent temperature calculations for a 120 km thick continent that is cooled by a flat slab at a depth of 90 km. (a) Vertical temperature profiles after the emplacement of a 600°C flat slab from 0 to 60 Myr; profiles are taken every 5 Myr. The initial continental geotherm is shown in green. (b) Surface heat flow and (c) Moho temperature of the 1D model as a function of time after the emplacement of a flat slab with different temperatures (blue dotted line: 400°C; black line: 600°C; green dotted line: 800°C). The red line is the numerical model results for the reference model at 400 km from the trench. The blue and red vertical lines are the lag times and time constants.

We also examine the effects of different slab depths from 50 to 120 km, for a 120 km continental thickness and 600°C slab temperature. The presence of the cool slab causes the continent to cool from its initial conditions to steady-state values that depend on the slab depth (Fig. 4.10). The timescale for cooling also depends on the slab depth, with the surface heat flow lag time increasing from  $\tau_l = 4$  Myr (50 km slab) to  $\tau_l = 32$  Myr (120 km slab). Similarly, the thermal time constant ( $\tau_c$ ) increases with slab depth and where the slab is shallower than 60 km, the Moho temperature and surface heat flow reaches steady state within  $\sim 30$  Myr. Note that both  $\tau_l$  and  $\tau_c$  vary non-linearly with slab depth, as the timescales for thermal conduction are proportional to the square of the thickness of the lithosphere above the slab surface (Dimitru, 1990; Turcotte and Schubert, 2002).

In the final calculations, we demonstrate the effects of initial continental structure on the cooling when the slab is at a very shallow depth (short cooling timescale). We test two continental thicknesses of 60 km and 120 km, with a 600°C slab at a depth of 50 km (2 km below the Moho). The thinner continent has a hotter initial structure than the reference 120 km continent, with initial Moho temperature of 1129°C and surface heat flow of 75.3 mW/m<sup>2</sup>. The timescales for cooling are the same for the two models as they have the same slab depth (Fig. 4.11). At the Moho,  $\tau_l = 0.026$  Myr and  $\tau_c = 0.031$  Myr and in both models, the Moho temperature rapidly decreases to the steady-state value of 590°C (Fig. 4.11a). The surface heat flow starts to decrease at  $\tau_l = 4.1$  Myr (Fig. 4.11b). At times greater than  $\tau_l$ , the heat flow is larger for the 60 km continent owing to its initially hotter structure, but both models approach the steady-state value of 50 mW/m<sup>2</sup> within 30 Myr.

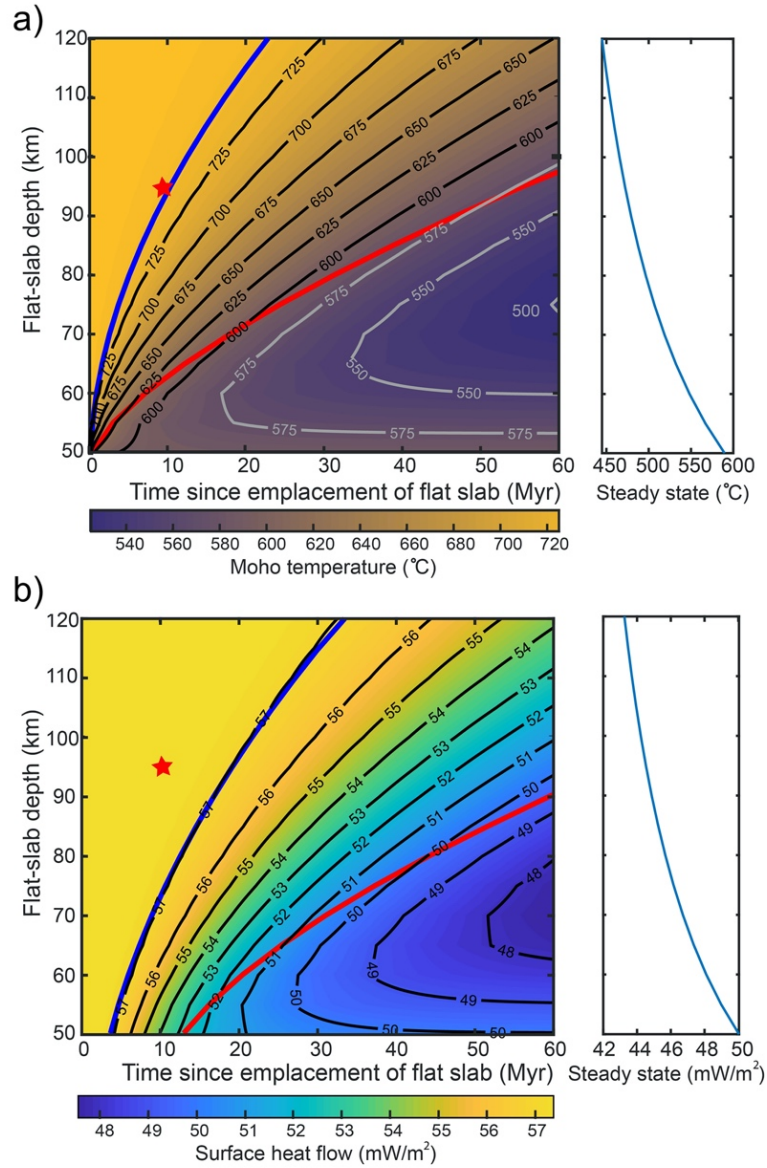


Figure 4.10. (a) Moho temperature and (b) surface heat flow contours for a 120 km thick continent and 600°C flat slab with various flat-slab depths and slab emplacement times. The blue line shows the lag time ( $\tau_l$ ), which is the time at which slab cooling initiates. The red line shows the time constant ( $\tau_c$ ) for cooling. The red star represents the Pampean flat-slab subduction condition. The plots on the right show the steady-state values of Moho temperature (a) and surface heat flow (b).

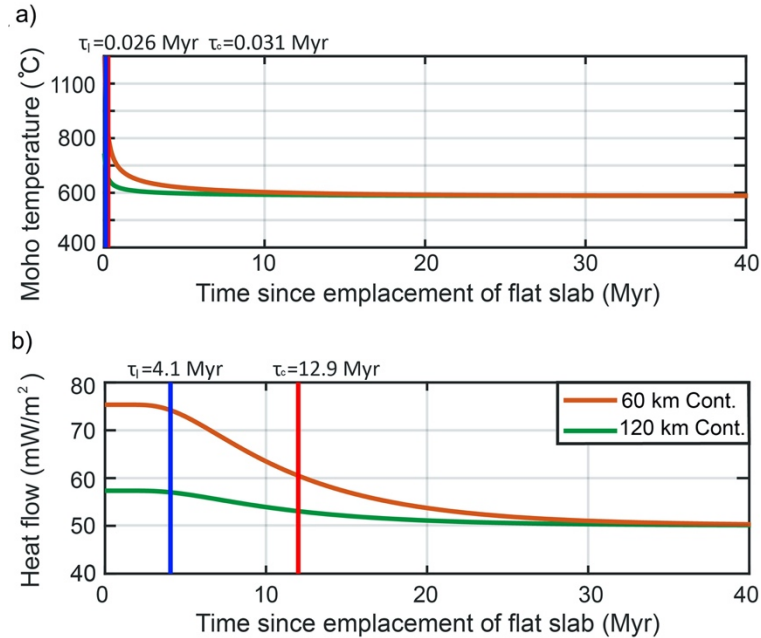


Figure 4.11. Comparison of (a) Moho temperatures and (b) surface heat flows between the 120 km and the 60 km thick continent for a 600°C flat slab at 50 km depth. The blue and red vertical lines are the lag times and time constants.

#### 4.4.4 Implications for modern and ancient flat-slab regions

Our numerical models provide insight into the interpretation of surface heat flow observations for modern flat-slab regions. The critical variables are 1) the flat-slab depth and 2) the length of time the flat slab has been emplaced below the heat flow measurement point. For shallow slabs like the Mexican and Peruvian flat slabs that have existed for <20 Ma, our results indicate that conductive cooling due to the underlying slab is expected to reduce surface heat flow measurements. In central Mexico, observations show very low surface heat flow (13-40 mW/m<sup>2</sup>; Ziagos et al., 1985) above a flat slab located at ~45 km depth (Manea et al., 2017). Our results indicate that a flat slab at ~50 km depth would reduce surface heat flow by over 20 mW/m<sup>2</sup> within 20 Myr through thermal conductive heat transfer (Fig. 4.11b). However, 20 mW/m<sup>2</sup> may be insufficient to explain the very

low heat flow measurements, even when error is considered. One possibility is that the flat slab is cooler than the 600°C assumed in our calculations, despite the young slab age and relatively slow convergence rate. Perry et al. (2016) suggest that the hydrothermal circulation within the oceanic crust of the Cocos plate could cool the subduction zone by up to 180°C which could account for this difference.

Similar to the Mexican flat slab, the flat slab in southern Peru also has a shallow slab depth of 60-70 km and is immediately beneath the continental Moho (Kumar et al., 2016; Bishop et al., 2017). Again, the shallow slab decreases the cooling lag time and increases the cooling magnitude. However, the Peruvian flat slab is migrating southward along the trench in addition to its trench-perpendicular growth direction (Hampel, 2002; Rosenbaum et al., 2005). This suggests that a thermal gradient north-to-south should be observable, with the continent above the older flat slab to the north being colder than the continent above the younger flat slab to the south. Unfortunately, there are insufficient heat flow measurements to fully explore this hypothesis. The existing heat flow measurements (20-60 mW/m<sup>2</sup>; Currie and Hyndman, 2006) are generally consistent with cooling that we predict, but more work is needed to fully incorporate the along-strike evolution of this complicated flat slab along with any other contributing factors to continental heat flow.

In contrast to shallow flat slab regions, low surface heat flow measurements above deeper flat slabs are not well explained with our models. In the Pampean flat-slab region, the flat slab lies at 90-110 km depth and was emplaced <11 Ma (e.g. Yanez et al., 2001; Kay and Mpodozis, 2002). Both our reference numerical model and our 1D calculations show that within the ~10 Myr existence time of the Pampean flat slab, the surface heat flow should not decrease through conductive heat transfer (Figs. 4.4, 4.9 and 4.10). However,

observed surface heat flow is 40-60 mW/m<sup>2</sup>, ~20 mW/m<sup>2</sup> less than typical back-arc values (e.g. Hamza and Muñoz, 1996; Collo et al., 2018; Fig. 4.1) despite the limited heat flow measurements. We suggest more heat flow measurements are needed in this region for future studies.

Some recent work suggests that heat flow measurements could be artificially suppressed using water during borehole drilling, and that a new assessment of thermochronological data suggests much more average heat flow above the Pampean flat slab (Stevens Goddard and Carrapa, 2018). If that is the case, this would be consistent with our results. However, the low heat flow measurements cited above are consistent with other previous studies using Curie point temperatures (Ruiz and Intracaso, 2004; Sanchez et al., 2018), crustal seismicity depths (Alvarado et al., 2009), and thermochronological data (e.g. Collo et al., 2011; 2017). Collectively these suggest relatively cool temperatures. One possibility is that these reflect processes beyond conductive cooling. For example, near surface hydrological processes such a changing groundwater flow pattern and local permeability could affect the surface heat flow significantly; low surface heat flow is observed in high recharge upland regions (Burns et al., 2015).

The surface heat flow is also affected by the initial continental structure prior to flat-slab subduction. Both initial thickness of the lithosphere and crustal radiogenic heat production affect the thermal structure. The low heat flow observations near the Pampean flat-slab (Fig. 4.1) are relatively uniform from the longitude of the paleo-arc to the east across the flat-slab region and into the Paleoproterozoic Rio de la Plata craton (Oyhantcabal et al., 2011). The flat slab traverses a series of north-south trending accreted terranes and associated arcs, including the Cuyania, Famatina, and Pampian terranes. The Cuyania

terrane is likely of Laurentian origin, and may have drifted from the Ouachita Embayment prior to its accretion to South America in the mid-Ordovician (Thomas and Astini, 1996; Ramos, 2004; Ramos et al., 2010). The Famatinian arc developed on continental crust during the early to mid-Ordovician with the accretion of the Cuyania terrane onto the Pampian basement (Pankhurst et al., 1998; Miller and Soellner, 2005, Ramos et al., 2010). The Pampian terrane is believed to have been part of Rodinia and likely accreted on to the western margin of the Rio de la Plata craton in the late Proterozoic (Ramos, 1988; Ramos et al., 2010). Given the diverse origins of these terranes, it is unlikely that the largely uniform heat flow observations is due solely to uniformly low radiogenic heat production. While a thick cratonic root may explain the low heat flow measurements, the ~100 km depth of the modern flat slab makes it unlikely that the overlying terranes had a much thicker lithosphere prior to flat-slab emplacement (Liu and Currie, 2019). We therefore do not ascribe the low heat flow measurements to pre-flat-slab tectonic structures.

Our models only consider conductive heat transfer from the cool flat slab. One possible additional cooling mechanism is flat-slab dehydration. Downgoing oceanic plates are believed to be extensively hydrated to depths of up to 30 km along outer-rise faults (Ranero et al., 2003; Fromm et al., 2006; Bloch et al., 2018; Cai et al., 2018; Grevemeyer et al., 2018; Wagner et al., 2020). The release of this water is believed to play a role in the generation of intermediate depth seismicity (e.g., Meade and Jeanloz, 1991; Ferrand et al., 2017) and in the generation of flux melting in normal subduction zones. The depth of this release in normal subduction zones depends dominantly on the temperature of the downgoing plate, which in turn depends on its age, convergence rate, and dip angle (e.g. Syracuse et al., 2010). In the case of flat slabs, a steady-state thermal profile is not achieved

within the lifetime of known flat slabs, and therefore we have the added variable of the duration of flat-slab subduction beneath a given portion of the overriding plate. In the case of the Pampean flat slab, there is copious intermediate depth seismicity along the shallowest portions of the flat slab (e.g. Anderson et al., 2007), suggesting that the horizontally lying slab is actively dehydrating. However, numerous tomographic studies (Wagner et al., 2005; 2006; 2008; Porter et al., 2012; Marot et al., 2014) have shown evidence of high shear wave velocities ( $>4.7$  km/s) above the seismically active portion of the flat slab. These high shear wave velocities are difficult to reconcile with the presence of any significant amount of serpentinite (Hacker and Abers, 2004; Abers and Hacker, 2016). This suggests that the mantle above the flat slab may be too hot for hydrous phases to be stable. In this case, the majority of the fluids are more likely to be transported up-dip along the slab surface (e.g. Cerpa et al., 2017). If fluids released from the flat slab penetrate to the above lithosphere, mantle melting occurs under high temperature and pressure conditions (Till et al., 2011). This flux of hydrous fluids may produce an additional mechanism for altering the thermal structure of the mantle lithosphere. The details of any such thermal effect due to dehydration would depend heavily on the rates of fluid migration, the fluid pathway, and mantle lithosphere composition, which are topics for future research.

In the western US, it is believed the Farallon plate developed a flat geometry in the Late Cretaceous (Coney and Reynolds, 1977; Copeland et al., 2017). Thermochronology data show there was a wide-spread cooling of the Cordilleran lithosphere during Farallon flat subduction (Dumitru et al., 1991). Within 200 km of the trench, thermochronology data indicates that the geothermal gradient decreased to one-fifth of the initial value of  $50^{\circ}\text{C}/\text{km}$  and cooling was delayed by 5-10 Myr after the cessation of arc magmatism (Dumitru,

1990). Dumitru's (1990) model shows that the delay time is dependent on the thickness of the continental mantle lithosphere above the slab surface and predicts that the slab here was at a depth of 35-50 km. This agrees with our results of significant surface cooling 5-10 Myr after flat-slab emplacement for a slab at ~50 km depth (Fig. 4.10). Thermochronology data also shows that the amount of cooling in the western US decreased from the trench to the continental interior, with a later onset of cooling further from the plate margin (Dumitru et al., 1991). Our model results are consistent with this observation that the region near the trench has the earliest and greatest amount of cooling and that the cooling decreases with distance landward from the trench (Fig. 4.3). The widespread cooling in the western US was likely caused by the long duration of the Farallon flat slab (~40 Myr), 20-30 Myr longer than present-day flat slabs. As shown in Figure 4.9, if a 90 km depth slab existed for 40 Myr, it could decrease the Moho temperature and surface heat flow by an extra ~130°C and 5 mW/m<sup>2</sup> compared to a slab with a 10 Myr duration. The cooling could also have been enhanced by the old (100 Ma) and cool Farallon plate that had a fast convergence rate (12 cm/yr). In addition, the old Farallon plate may also have allowed slab dehydration to occur further inboard (English et al., 2003; Humphreys et al., 2003; Currie and Beaumont, 2011), enhancing the possibility of fluid-induced cooling.

#### **4.5 Conclusion**

The relatively low surface heat flow observed in continental areas above a flat slab is commonly attributed to cooling of the continent by the presence of the cold oceanic plate at the base of the continental lithosphere (e.g. Dumitru et al., 1991; van Hunen et al., 2004; Currie and Hyndman, 2006; Manea et al., 2017). The numerical models in this study allow an assessment of the evolution of continental thermal structure during flat-slab subduction.

Our models show that once a flat slab forms, the continent undergoes conductive cooling over timescales of 10's of Ma. Cool temperatures diffuse from the slab upward through the continental lithosphere, leading to a delay between the emplacement of the flat slab and the onset of cooling of the shallow continent (Fig. 4.10). This lag time depends primarily on the depth of the flat slab, with surface cooling initiating at 4 and 32 Ma for slabs at 50 and 120 km depth, respectively. At a given time after flat-slab emplacement, the magnitude of cooling is enhanced by a high thermal conductivity, an old and/or shallow oceanic plate, and a fast convergence rate.

Present-day flat slabs have only been in place for <20 Ma. The Mexico and Peru flat slabs are at shallow depths (45-70 km) and therefore the observed low surface heat flow in these areas is likely due to slab cooling. In contrast, the Pampean flat slab is at 90-100 km depth, and conductive cooling cannot explain a reduction of surface heat flow in this area. We suggest that additional cooling mechanisms are needed to explain the low surface heat flow, such as the thermal effect of the cool fluids from slab dehydration. Our models also have implications for ancient flat-slab regions. Widespread cooling in the western US in the Late Cretaceous is consistent with the presence of a long-lived old Farallon flat slab with a fast convergence rate and slab dehydration across a wide area.

---

## Chapter 5 Formation of the Sierras Pampeanas during Pampean flat-slab subduction

---

### Abstract

The Sierras Pampeanas (27°-33°S) in western South America is characterized by thick-skinned deformation, including basement-cored uplifts and shortening that occurs 500-700 km from the nearest convergent margin. Deformation in the Sierras Pampeanas correlates spatially and temporally with an area of flat-slab subduction of the Nazca plate in the last ~ca. 10 Ma. We use 2D thermal-mechanical models to study the dynamics of Pampean flat-slab subduction and the origin of the Sierras Pampeanas. Models examine a geological time from ca. 12 Ma to present-day, during which time the Juan Fernandez Ridge subducted beneath South America. Models show that the buoyant ridge triggers slab flattening, resulting in regional compression of the continent through end-loading at the plate margin. Deformation in the continental interior depends on the inherited structure of the continental plate, where surface uplifts and shortening are concentrated at pre-existing weak zones. Inboard migration of deformation is controlled by surface topography caused by the buoyant ridge, rather than basal shear from the growing flat slab. Deformation occurs prior to the passage of the ridge and is inhibited when the ridge is beneath the region owing to dynamic uplift.

### 5.1 Introduction

Orogenic processes near convergent margins are driven by forces associated with plate convergence and lead to two styles of plate shortening, thin-skinned and thick-skinned deformation (e.g. Pfiffner, 2006). Whereas thin-skinned deformation involves only

the cover rocks, thick-skinned deformation involves crystalline basement rocks as faults cut through the entire crust (e.g. Rodgers, 1949; Pfiffner, 2006). Thick-skinned deformation is generally associated with regions that have large compressional forces, such as those near arc or continental collision zones (e.g. Smalley and Isacks, 1990), and is less common in subduction zones. However, basement-cored uplifts and crustal shortening have been observed in foreland regions that are hundreds of kilometers inboard of a subduction margin, including the Late Cretaceous Laramide Orogeny in western United States and the present-day Sierras Pampeanas in western Argentina (e.g. Jordan and Allmendinger, 1986; Bird, 1998); these contrast with thin-skinned deformation that is found elsewhere at these margins.

The origin of thick-skinned deformation in the continental interior is unclear. Deformation in these two regions coincides with areas of flat-slab subduction of the Farallon and Nazca Plates (Jordan and Allmendinger, 1986; Bird, 1998), where the oceanic plates travel subhorizontally at a depth of ~100 km depth below the continent. Thus, it is speculated that deformation is related to the flat slabs (Dickinson and Snyder, 1978; Jordan and Allmendinger, 1986; Ramos et al., 2002). However, how flat subduction causes intraplate thick-skinned deformation is debated. Two main mechanisms have been proposed: (1) basal shear, where stresses created through coupling along the slab-continent interface transfer upward into the continent, and (2) end-loading, where stresses are primarily transferred horizontally from the distal plate margin, with increasing stress as the slab flattens (e.g. Dickinson and Snyder, 1978; Bird, 1998). Here, we present 2D thermal-mechanical models that are based on Pampean flat subduction. These are used to assess the stress regime associated with flat subduction and the factors that cause uplift and shortening

of the Sierras Pampeanas. As this region is the modern analog of the Laramide Orogeny, our results also provide insights into Laramide deformation.

## **5.2 Tectonics of Pampean flat subduction and the Sierras Pampeanas**

The Sierras Pampeanas coincides with a segment of flat-slab subduction of the Nazca plate (the Pampean flat slab) and is inboard of where the Juan Fernandez Ridge enters the subduction zone (Fig. 5.1, e.g. Pilger, 1984; Yáñez et al., 2001; Yáñez et al., 2002; Kay and Mpodozis, 2002). Seismic studies show that the Nazca plate subducts to a depth of 80-110 km beneath the South American plate and then unbends to form a horizontal geometry for ~300 km inboard before plunging steeply into the mantle (e.g. Porter et al., 2012). The thick crust of the subducted Juan Fernandez Ridge is believed to provide buoyancy forces that support the Pampean flat slab (e.g. Yáñez et al., 2002; Gans et al., 2011). The timing of flattening is constrained by the eastward migration and expansion of magmatism (Kay and Mpodozis, 2002). At ~32°S, arc magmatism was initially located in the Frontal Cordillera and started to migrate east approximately 2 Myr after the Juan Fernandez Ridge started to subduct at 12 Ma, with the last magmatism observed in the Sierras Pampeanas at 1.9 Ma (e.g. Yáñez et al., 2001; Kay and Mpodozis, 2002).

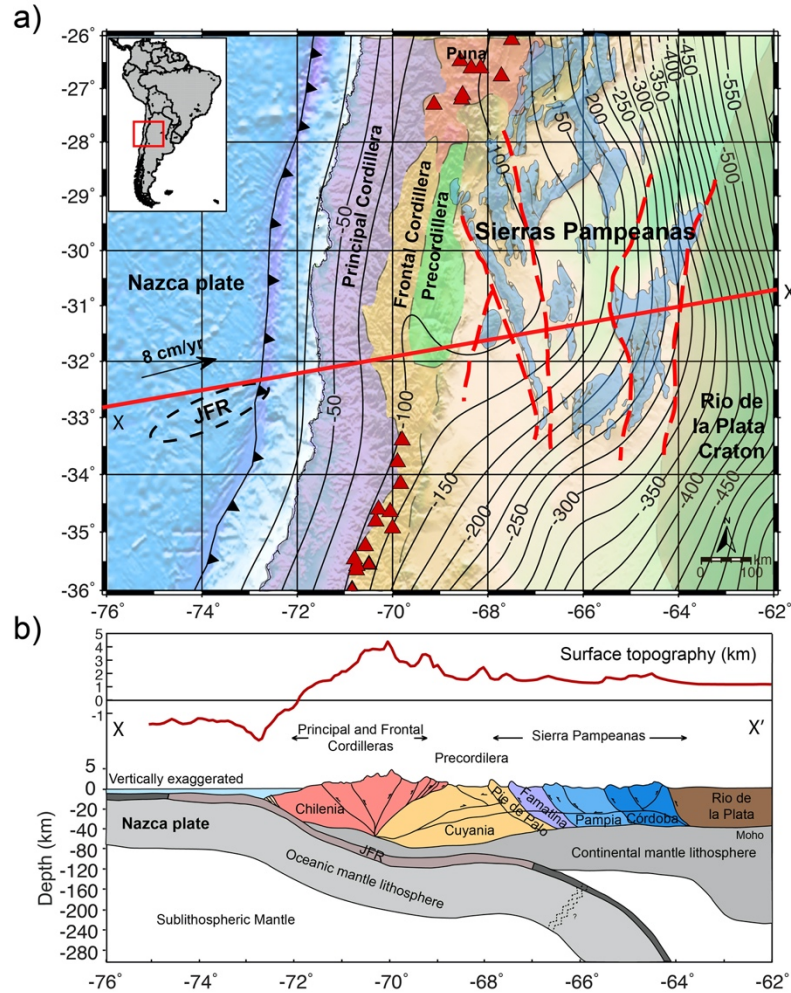


Figure 5.1. (a) Map of the Pampean flat-slab region. Red triangles are active volcanoes. Red dashed lines are the major terrane boundaries (Ramos et al., 2002; Richardson et al., 2013). (b) Cross section along X-X' (red line in (a)); top plot is the surface topography along X-X'. JFR is Juan Fernandez Ridge.

The Sierras Pampeanas has a complex deformation history. The current phase of deformation at  $\sim 32^\circ\text{S}$  initiated at ca. 6-5.5 Ma and coincides with the eastward propagation of magmatism (Ramos et al., 2002). Deformation includes basement-involved folds and east-dipping faults that strike N-S, approximately perpendicular to the subduction direction (e.g. Richardson et al., 2013). The uplifts correlate spatially with major terrane sutures, shear zones and fault zones from earlier tectonics, with an average uplift of 2 km (Fig. 5.1;

e.g. Ramos et al., 2002; Löbens et al., 2011). In the early to middle Paleozoic, east directed subduction resulted in a series of terrane accretions to the western side of the Rio de la Plata craton (e.g. Rapela et al., 2007). Between the Late Paleozoic to early Cretaceous, there were two extensional events that caused rift zones and faults along the suture zones (e.g. Ramos et al., 2002). There are five recognized faults and major sutures (Fig. 5.1; e.g. Ramos et al., 2002; Richardson et al., 2013), and these inherited structures are believed to play an important role in basement block uplift during Sierras Pampeanas deformation (e.g. Pilger, 1984).

### **5.3 Geodynamic modelling**

To investigate the causes of the Sierras Pampeanas deformation, we develop 2D numerical models of the Pampean flat-slab region. The models are used to study the thermal-mechanical behavior of the lithosphere and upper mantle, including material deformation and development of topography (e.g. Fullsack, 1995; Beaumont et al., 2006). The model is 1800 km wide and 1200 km deep (Fig. 5.5). Within the domain, we model subduction of the Nazca plate beneath the South America plate along profile X-X' in Figure 5.1, where the subduction evolves dynamically. The Nazca plate age is 40 Ma, corresponding to an 80 km-thick lithosphere (Stein and Stein, 1992; Müller et al., 2008). Within the oceanic plate, there is a 1200 km long oceanic ridge with 12-18 km crust, representing the Juan Fernandez Ridge (Yáñez et al., 2001; Kopp et al., 2004). This subducts below a 120 thick continental plate. Further inboard, we include a 200 km thick craton that is located 1000 km from the trench, corresponding to the Rio de la Plata craton (Bologna et al., 2019). We impose a constant convergence rate of 8 cm/yr on the lithosphere side boundaries, with 3.3 cm/yr on the oceanic plate and 4.7 cm/yr on the continent. The

top boundary is a free surface where topography can self-consistently develop. The detailed model setup is given in Section 5.6.1. We model a geological time from ca. 12 Ma to present-day, which covers the development of Pampean flat slab at  $\sim 32^\circ\text{S}$  (e.g. Yáñez et al., 2001). The models test the individual effects of a flat slab and continental weak zones, as well as the combination of these factors on continental deformation.

Figure 5.2a shows a model in which the continent does not have weak zones. The model starts with a steep-angle subduction zone and the oceanic ridge is located at the trench at the beginning of the model (0 Myr); this corresponds to a geological time of 12 Ma. As the low-density oceanic ridge subducts, its buoyancy leads to a shallowing of the subducting slab angle (e.g. van Hunen et al., 2002; Liu and Currie, 2019). Low-angle subduction starts to form at  $\sim 5$  Myr and transient dynamic uplift of the overlying continent is observed due to the buoyant ridge (Fig 5.2; Dávila and Lithgow-Bertelloni, 2015). By the end of the 12 Myr model run, the slab has a 300-400 km wide subhorizontal portion at 90-110 km depth. This matches the Pampean flat-slab structure from present-day seismic observations (e.g. Porter et al., 2012). However, during the 12 Myr model run, there is no obvious deformation in the continent.

In Figure 5.2b, five weak zones are added to the continent. Their locations are based on the major terrane suture zones in the Pampean region (Fig. 5.1; Ramos et al., 2002). The weak zones have a low frictional angle ( $\phi=1^\circ$ ) and extend through the upper and lower crust. The overall evolution of the subduction geometry is similar to that in the previous model. However, with the development of flat slab, shortening and uplift occur near the weak zones. This creates local fluctuations in the model topography that match the observed surface topography in this region, including regions with  $\sim 2$  km uplift (Fig. 5.2b).

Additional models show that the depth extent of the weak zones strongly affects the results, such the deformation occurs for weak zones that extend through the lower crust, with larger deformation as the weak zone depth increases (Fig. 5.7). In the final model, we test the effect of slab geometry. In this model, there is no buoyant oceanic ridge, and as a result, no flat slab develops (Fig. 5.2c). This model includes the continental weak zones as in Figure 5.2b, but the continuous steep-angle subduction does not result in continental deformation.

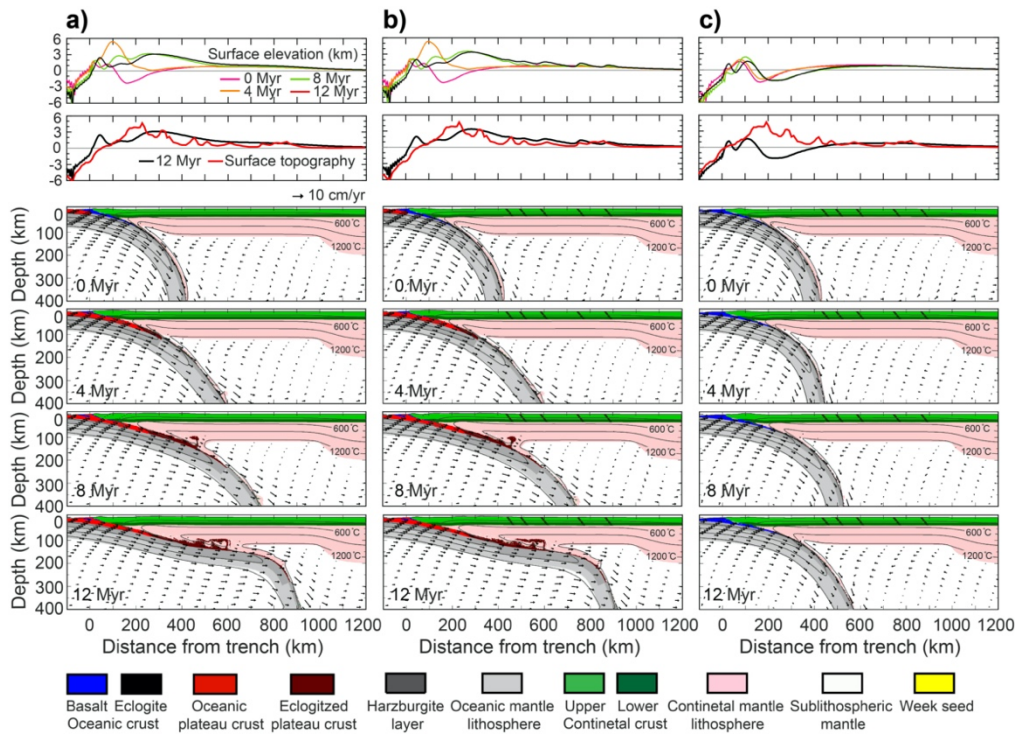


Figure 5.2. Model evolution with surface elevation every 4 Myr. Plots in second line compare the 12 Myr model topography (black line) and observed topography (red line). (a) Flat subduction below a continent with no weak zones. (b) Flat subduction with weak zones (dark green inclined structures in the continent). (c) Steep-angle subduction with weak zones.

## 5.4 Discussion

The models show that continental deformation only occurs if there is both flat subduction and pre-existing weak zones in the continent (Fig. 5.2). However, the stress regime that leads to deformation remains unclear. In Figure 5.3, we plot the horizontal deviatoric stress of the model shown in Figure 5.2b.

At 0 Myr, the horizontal deviatoric stress in the continental crust is relatively low (<100 MPa) and mainly reflects the flexure of the continental plate, where surface extension occurs 200-400 km from the trench and compression farther inboard. This is commonly observed above steep-angle subduction zones (e.g. Turcotte and Schubert, 2002). As the buoyant oceanic ridge enters the subduction zone, horizontal compression is observed throughout the continental crust and the magnitude increases as the flat slab develops (Fig. 5.3a). Compression originates from end-loading where the high stresses are created by the buoyant oceanic ridge and shallow subduction angle, and there is no significant upward transfer of stress from the top of the flat slab, as the rheology of the material above the slab limits the effects of basal shearing (Axen et al, 2019).

The continental yield stress and the modeled horizontal deviatoric stress at 700 km (normal lithosphere) are shown in Figures 5.3b and 5.3c, respectively. The continental crust is generally in the viscous-plastic regime, where strength increases with depth, based on the friction angle ( $\phi$ ), with the highest strength in the deep crust and shallow mantle (Fig. 5.3c). Weak zones must therefore cut through the lower crust (and possibly upper most mantle) in order for the high compressional stresses due to flat subduction to trigger continental deformation (Fig. 5.7). For comparison, we plot the horizontal deviatoric stress of steep-angle subduction model (Fig. 5.3d). Continuous steep subduction causes long-

wavelength flexure of the continent, as shown by the wider region under extension, but the stress level is not enough to cause deformation (Fig. 5.8).

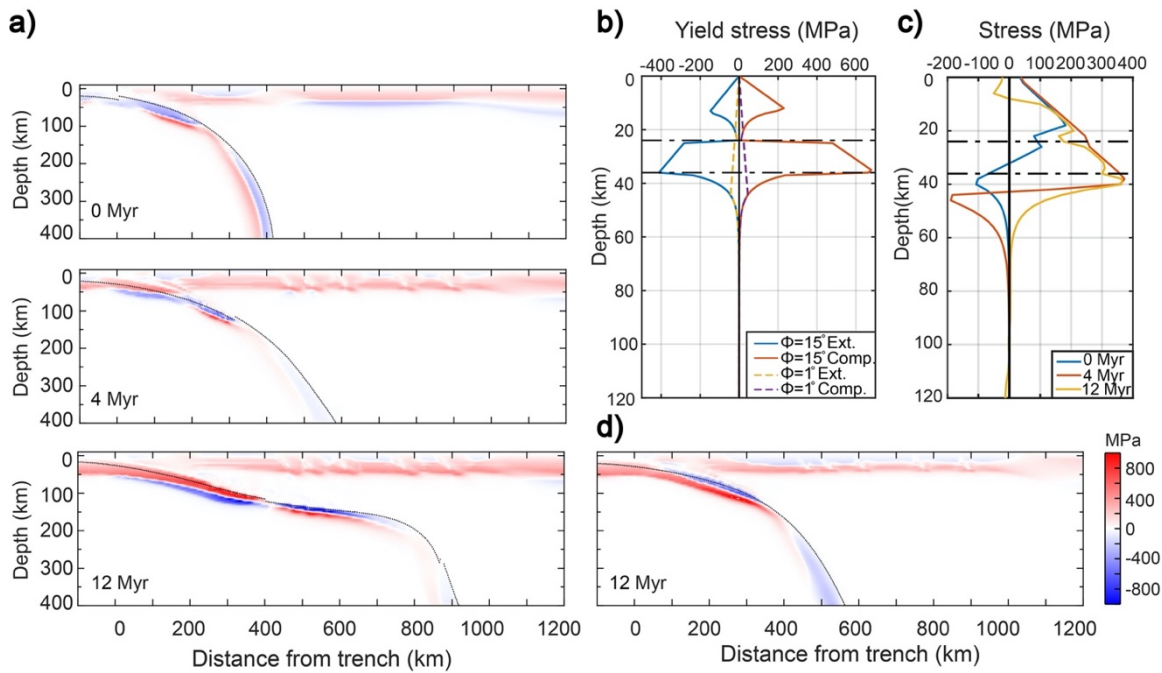


Figure 5.3. (a) Horizontal deviatoric stress field of the model in Figure 5.2b. (b) Theoretical continental yield stress profiles based on model rheologies and thermal structure (strain rate of  $10^{-16} \text{ s}^{-1}$ ) for extension and compression and different friction angles ( $\phi$ ). (c) Model horizontal deviatoric stress at 700 km from the trench. (d) Horizontal deviatoric stress field of the steep-angle subduction model in Figure 5.2c.

To examine the temporal evolution of deformation, Figure 5.4a shows the maximum shear strain rate at the surface for the model in Figure 5.2b. As the slab shallows and the flat slab starts to form at  $\sim 5$  Myr, the strain rate increases for all five weak zones. Strain rates are initially highest at the weak zones closest to the trench, and the maximum deformation migrates to the east. After  $\sim 10$  Myr, the highest strain rate occurs at the two inboard weak zones.

This migrating pattern of deformation seems inconsistent with the compression experienced by the entire continent by end-loading. The migration is caused by the surface uplift and subsidence due to the passage of the buoyant oceanic ridge. Initially, all continental regions have low elevation (Fig. 5.4b). The flat slab causes dynamic uplift that tracks eastward as the flat slab grows. The temporary surface uplift exerts a horizontal extensional force on the shallow crust above the oceanic ridge, which partially compensates the compressional force from end-loading and inhibits deformation while the buoyant ridge is beneath this region (Fig. 5.4a). At 12 Myr in our model, the ridge has not reached beneath the two easternmost weak zones, and deformation continues in these regions, while there is little deformation in the high-elevation region to the west. This also explains why the weak zones near the trench start to deform  $\sim 1$  Myr earlier than the weak zone that is farthest from the trench. In the first 4 Myr of the model, there is a transient surface subsidence at these locations owing to the descending slab.

The models show that deformation initiates 5-7 Myr after the oceanic ridge started to subduct (Fig. 5.4a), corresponding to a geological time of ca. 7-5 Ma. This agrees with the onset (ca. 6-5.5 Ma) of the Sierras Pampeanas uplift at  $\sim 32^\circ\text{S}$  based on geochronological data (Ramos et al., 2002). One thing we did not consider in the models is magmatism. Previous studies show that magmatism leads to thermal weakening of the continent that decreases the rock strength and promote deformation (James and Sacks, 1999; Ramos et al., 2002). In the Pampean region, magmatism expanded eastward as the flat slab developed (Fig. 5.4a; Capaldi et al., 2020). Our modeled deformation lies within the area affected by magmatism, and therefore the effects of magmatism may enhance the eastward migration of deformation.

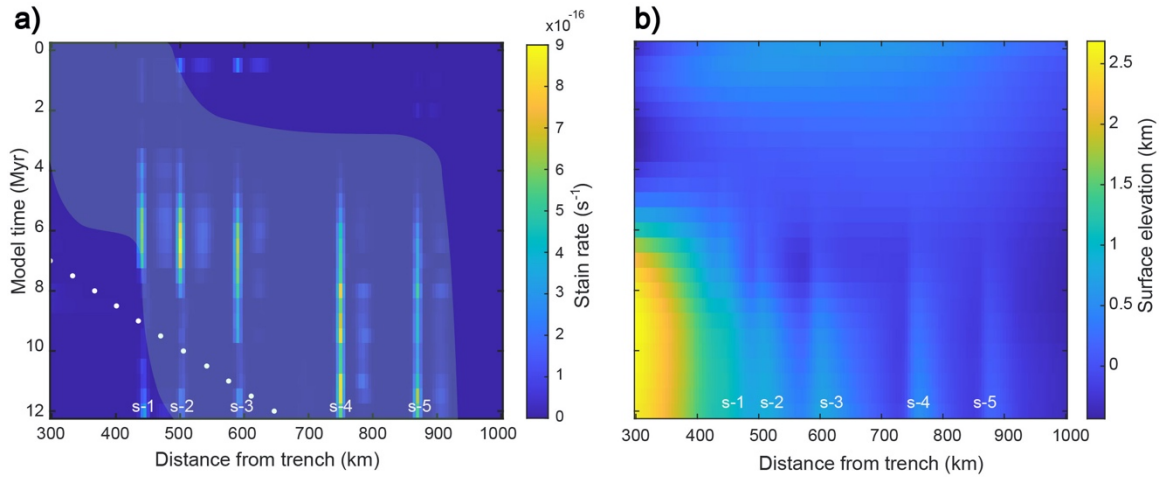


Figure 5.4. (a) Temporal changes in surface maximum shear strain rate for the continent of the model in Figure 5.2b. The white dots show the trajectory of the center of the oceanic ridge. The shaded region shows the volcanism migration patterns (Capaldi et al., 2020). (b) Temporal evolution of continental surface elevation of the model in Figure 5.2b.

## 5.5 Implications and conclusion

Our models show that flat-slab subduction causes regional continental compression through end-loading at the plate margin. However, this may not be sufficient to induce deformation in the continental interior. Pre-existing weak zones that extend into the deep crust are needed in order to allow crustal shortening and uplift, where deformation is concentrated at these zones. Therefore, inboard deformation is a result of combined effects of weak regions, either inherited structures or thermal weakening due to magmatism, and compression from flat subduction. We also find that the flat slab creates transient surface uplift of the continent. This inhibits deformation in the region that is underlain by the buoyant ridge. The eastward migration of deformation observed in the Sierras Pampeanas

is controlled by dynamic topography due to passage of the buoyant Juan Fernandez Ridge, instead of basal shear from underlying slab.

These results also have implications for the Laramide Orogeny in North America that occurred during flat subduction of the Farallon Plate (e.g. Dickinson and Snyder, 1978; Bird, 1988). Laramide deformation appears to be localized by Precambrian sutures (Karlstrom and Humphreys, 1998), and within the weaker crust of the Archean Wyoming craton compared to the adjacent Proterozoic terranes in Colorado (e.g. Snelson et al., 1998; Worthington et al., 2016). Deformation generally migrated inboard toward the northeast and correlates with a northeastward migration of surface uplift and the inferred position of the Conjugate Shatsky Rise below the continent (Copeland et al., 2017). However, there is evidence of deformation in Montana, ~1000 km from the trench, in the Early Cretaceous at the onset of slab-flattening (Carrapa et al., 2019). We suggest that this deformation may have been caused by regional compression from end-loading.

## **5.6 Supplemental materials**

### **5.6.1 Numerical model setup**

Our model geometry is based on Pampean flat-slab subduction in central Chile (~31°S-33°S). In this area, the Nazca plate subducts under the South America Plate and then unbends to become subhorizontal at ~110 km depth. The geometry of the subducting slab is well constrained by tomography and intra-slab earthquake locations (e.g. Kopp et al., 2004; Anderson et al., 2007; Porter et al., 2012).

The 2D model plane is oriented parallel to plate convergence direction along X-X' in Figure 5.1. Figure 5.5 shows the initial model geometry. The model domain is 1800 km wide and 1200 km deep. The oceanic plate is on the left side of the model domain and the

continental lithosphere is on the right side. The trench is located at 300 km from the left boundary. In this study, we report all distances with respect to the trench.

The subducting Nazca plate in the Pampean region has an age of 40 Ma at the trench (e.g. Müller et al., 2008). This corresponds to 80 km thick oceanic lithosphere based on the GDH1 plate cooling model (Stein and Stein, 1992). At this latitude, the Nazca plate contains a linear aseismic oceanic ridge (a chain of volcanic islands and seamounts), the Juan Fernandez Ridge (e.g. Yáñez et al., 2002; Gans et al., 2011). Plate reconstructions show that the ridge started to subduct at ca. 12 Ma at  $\sim 32^\circ\text{S}$ , and the orientation of the ridge is in the direction of subduction (Yáñez et al., 2001). Seismic studies indicate that the average crustal thickness of the aseismic ridge is 10-22 km (Gans et al., 2011), with a thinner crust for the offshore portion (Kopp et al., 2004) and a thicker crust for the subducted portion (Yáñez et al., 2002). In our models, the oceanic plate has a 1200 km wide oceanic ridge to represent the Juan Fernandez Ridge. The thickness of the ridge crust is 18 km for the east portion of the ridge (500 km in length), which will be fully subducted during the model run. The rest of the ridge has a crustal thickness of 12 km. The thickness of the normal oceanic crust is 8 km. There is a layer of harzburgite that has twice the thickness of the crust to represent melt-depleted mantle (van Hunen et al., 2004). The ridge is positioned so that its eastern end is located at the trench at the start of the model run (0 Myr).

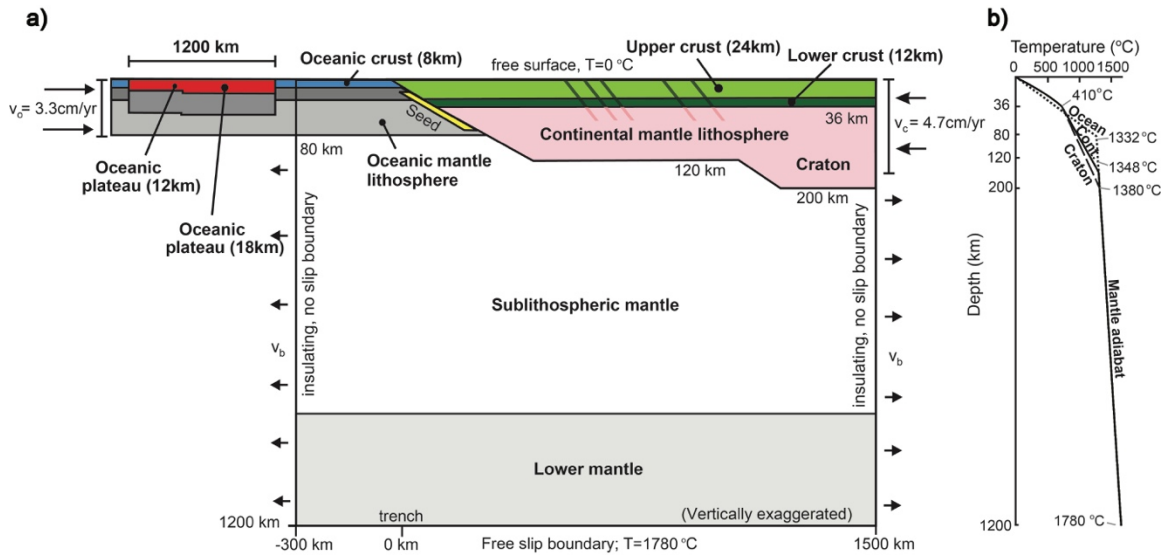


Figure 5.5. (a) Initial model geometry and boundary conditions. Inclined planes in the continent are weak zones. (b) Initial geotherms for the continental and oceanic lithosphere.

The continental plate is divided into a 120 km thick lithosphere adjacent to the plate margin and a 200 km thick lithosphere that starts 1000 km away from the margin (Fig .5.5). The thick lithosphere represents the Rio de la Plata craton (Fig .5.1), and the thickness of ~200 km is based on magnetotelluric data (e.g. Bologna et al., 2019). For simplicity, the continental crust has the same thickness of 36 km for both parts of the continent (Assumpção et al., 2013). The continental crust is divided into a 24 km thick upper crust and 12 km thick lower crust. We also introduce five weak zones in the continental lithosphere. Their locations are based on the position of major terrane boundaries and suture zones in the Pampean region (Fig .5.1). Surface observations and focal mechanisms studies show that the faults and shear zones within the terrane sutures have a dominantly east-dipping trend, with a dip angle of  $20^\circ\text{E}$  to  $60^\circ\text{E}$  (e.g., Jordan and Allmendinger, 1986; Regnier et al. 1992; Costa and Vita-Finzi, 1996; Ramos et al., 2002). Therefore, in the models, the weak zones dip toward the east (craton-ward) at  $50^\circ$ . The width of each weak

zone is 10 km and the top of the five weak zones are 430 km, 490 km, 580 km, 740 km, and 860 km from the trench, respectively. We test the effects of weak zones that extend from the surface to three different depths: 24 km, 36 km, and 72 km. This corresponds to weak zones that cut through the upper crust, upper and lower crust, and the entire crust plus uppermost mantle, respectively.

### 5.6.2 Material properties

The thermal and mechanical properties of all model materials are listed in Table 5.1. These follow values used in previous chapters. All materials undergo viscous-plastic deformation and have a temperature dependent density. Frictional-plastic deformation is determined by the Drucker-Prager yield criterion, and viscous deformation, based on power-law creep occurs at stresses below frictional-plastic yield. We use laboratory-derived viscous rheologies with a linear scaling factor ( $f$ ) to vary the strength of the model materials, in order to account for the effects of composition and hydration variations relative to the laboratory samples (Beaumont et al., 2006). Materials undergo frictional-plastic strain softening and viscous strain weakening following Warren et al. (2008) and Beaumont et al. (2006). The weak zones have a low effective internal angle of friction of  $1^\circ$ , with all other properties the same as the adjacent rocks. The sub-lithospheric mantle has a wet olivine rheology, with  $f=1$  to a depth of  $\sim 660$  km and  $f=10$  below, to represent the increase in viscosity in lower mantle (Karato, 1981; Karato and Wu, 1993). We do not model detailed phase changes through the mantle transition zone.

Models include a phase change of the oceanic crust from basalt to eclogite when the temperature and pressure conditions reach the eclogite stability field (Hacker et al., 2003). As oceanic crust enters the eclogite field, there is an increase in reference density

from 2950 to 3500 kg/m<sup>3</sup> but no other properties change. Normal oceanic crust undergoes full eclogitization, whereas the oceanic ridge crust undergoes 10% eclogitization to a reference density of 3125 kg/m<sup>3</sup>. This assumes that the oceanic ridge remains partially metastable due to its dryness; this allows the oceanic ridge to remain buoyant enough for slab flattening to occur (Liu and Currie, 2019).

### 5.6.3 Boundary conditions and model initialization

Figure 5.5 shows the model boundary conditions during the model run. In this study, we use a constant convergence rate of 8 cm/yr, consistent with the average convergence rate between the Nazca and South America plates in the past ~10 Ma (e.g. Müller et al., 2016). This is composed of an oceanic plate velocity ( $v_o = 3.3$  cm/yr) and continental plate velocity ( $v_c = 4.7$  cm/yr), based on the hotspot reference frame, HS3-NUVEL 1A (Gripp and Gordon, 2002). Models are run in the continental reference frame; therefore  $v_c$  is added to all boundaries. The plate velocities are applied to the lithosphere side boundaries. This is balanced by an outflux velocity along the sublithospheric mantle ( $v_b$ ), to maintain a constant mass in the model domain. A geotherm corresponding to an oceanic plate age of 40 Ma (Stein and Stein, 1992) is assigned to the incoming oceanic lithosphere (Fig 5.5b). The remaining side boundaries are no-slip, insulating boundaries. The top boundary is a free surface and the bottom boundary is a closed, free-slip boundary. The temperatures of the top and bottom boundaries are 0°C and 1780°C, respectively. The bottom temperature is calculated based on a 1300°C mantle adiabat with vertical gradient of 0.4 °C/km.

Model runs are divided into three phases. In phase one, the models undergo isostatic adjustment based on the initial thermal structure of the oceanic and continental plate (Fig .5.5b), in which the dense oceanic plate subsides by ~4 km. There are no plate

velocities in this phase. In phase two, a velocity of 5 cm/yr is applied to the oceanic plate in order to initiate subduction. This phase is run to 700 km convergence and results in the formation of a steep-angle subduction zone. By the end of phase two, the oceanic plateau is located at the trench. The models shown in this study start at this point (0 Myr), corresponding to the third phase. All times are reported relative to this time. Models are run for 12 Myr in phase three with the convergence rate of 8 cm/yr described above.

#### 5.6.4 Supplemental model plots

Figure 5.6 shows the full model domain for the model shown in Figure 5.2b, where there is a flat slab and continental weak zones.

Figure 5.7 shows the effects of variations in the depth of the weak zones. In Figure 5.7a, the weak zones are limited to the upper continental crust. During the development and growth of the flat slab, there is negligible deformation of the continent. Figure 5.7b show a model in which the weak zones extend through the continental crust and the top 36 km of the mantle lithosphere. In this model, significant deformation occurs and causes over 6 km uplift and over 150 km shortening. With the large amount of shortening, the slab does not have enough time to form a flat geometry within 12 Myr model run. When the buoyant ridge reaches beneath to the seaward weak zones, dynamic surface uplift inhibits deformation in these zones. The two models in Figure 5.7 along with the model shown in Figure 5.2b (weak zones to the base of the crust) indicate that the amount of deformation depends on the depth of the weak zones, with a greater amount of deformation as the weak zone depth increases. This is consistent with the strength profiles for the continent in our models (Figs. 6.3b and 6.3c). If the weak zones cut through at least the lower crust, the continent is susceptible to deformation.

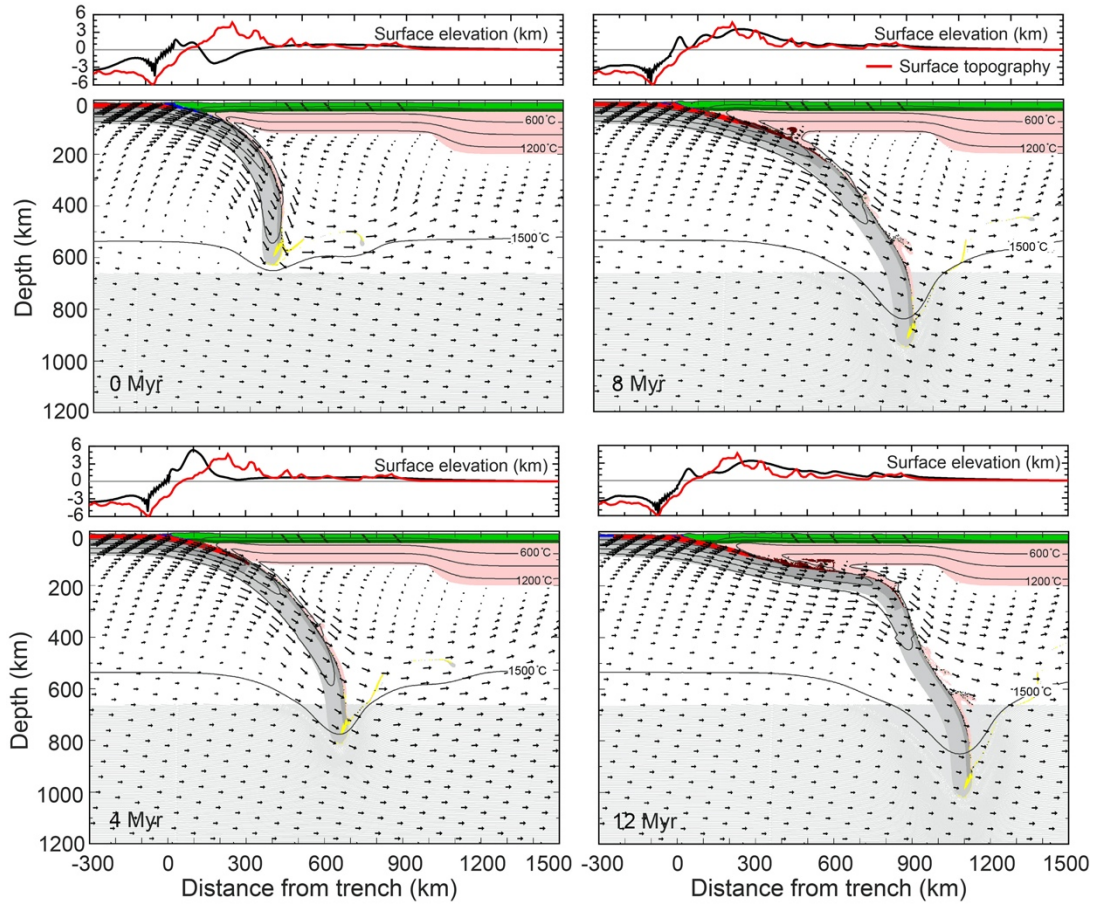


Figure 5.6. Evolution of the model shown in Figure 5.2 with the full model domain. The top plots show the surface topography of the model at each time (black line), and red line is the observed present-day surface topography along X-X' in Figure 5.1. The material colors follow those in Figure 5.2.

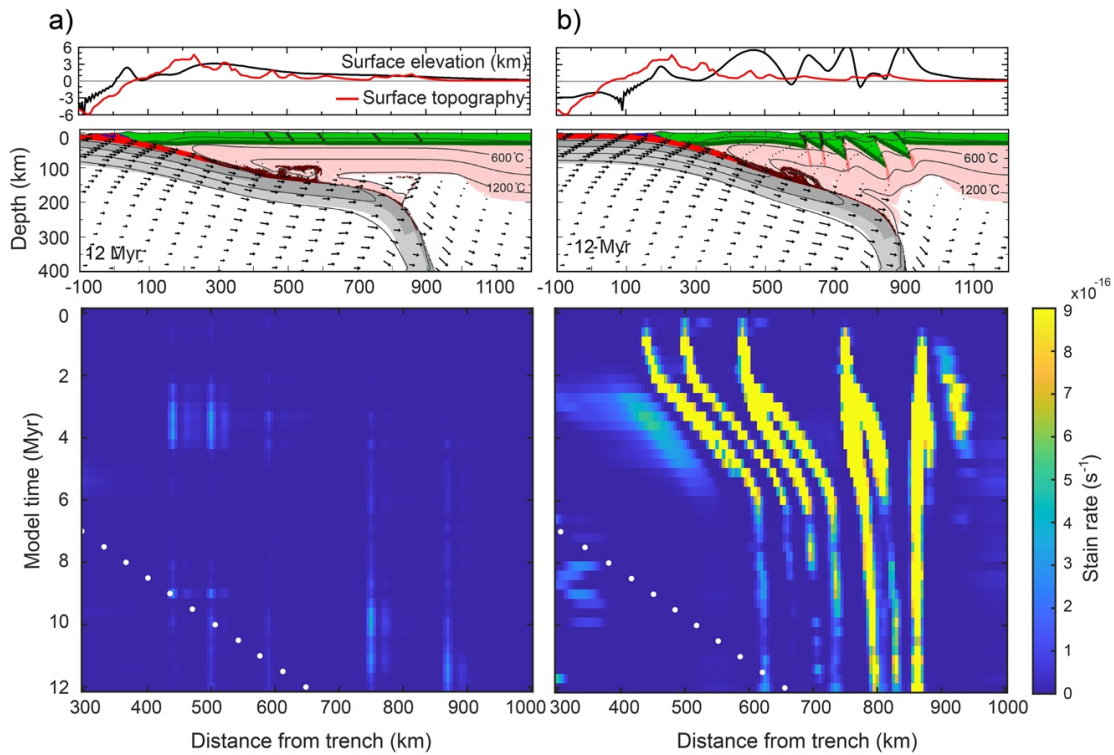


Figure 5.7. Model geometry at 12 Myr and surface maximum shear strain rate of (a) a model with weak zones within the upper continental crust only and (b) a model with weak zones that cut through the whole crust and the upper 36 km of the mantle lithosphere. The material colors follow those in Figure 5.2. The white dots show the trajectory of the center of the east portion of the ridge (500 km wide).

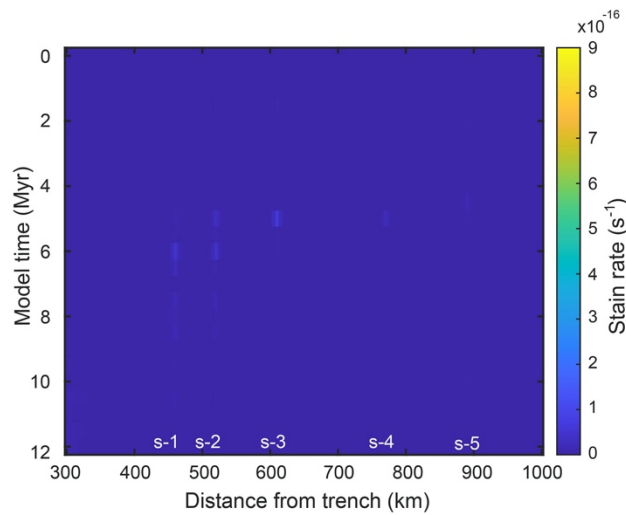


Figure 5.8. Surface maximum shear strain of model in Figure 5.2c.

## 5.6.5 Table of model parameters

Table 5.1. Model parameters

	Oceanic crust	Oceanic mantle lithosphere	Cont. upper crust	Cont. lower crust	Cont. mantle lithosphere	Sub-lithospheric mantle
<b>Plastic rheology *</b>						
$C_0$ (MPa)	0	0	20	0	0	0
$\phi_{eff}$	15° †	15°	15° †	15° †	15° †	15° †
<b>Viscous rheology §</b>						
<b>Material #</b>	Dry Maryland diabase	Wet olivine	Wet quartzite	Dry Maryland diabase	Wet olivine	Wet olivine
<b>f</b>	0.1 **	10	50	1	10 **	1 **
$A_{ps}$ (Pa <sup>-n</sup> s <sup>-1</sup> ) ††	5.78×10 <sup>-27</sup>	1.76×10 <sup>-14</sup>	8.57×10 <sup>-28</sup>	5.78×10 <sup>-27</sup>	1.76×10 <sup>-14</sup>	1.76×10 <sup>-14</sup>
$B^*$ (Pa <sup>-n</sup> s <sup>-1</sup> ) ††	1.91×10 <sup>5</sup>	1.92×10 <sup>4</sup>	2.92×10 <sup>6</sup>	1.91×10 <sup>5</sup>	1.92×10 <sup>4</sup>	1.92×10 <sup>4</sup>
<b>n</b>	4.7	3.0	4.0	4.7	3.0	3.0
<b>Q</b> (kJ mol <sup>-1</sup> )	485	430	223	485	430	430
<b>V*</b> (cm <sup>3</sup> mol <sup>-1</sup> )	0	10	0	0	10	10
<b>Thermal parameters</b>						
<b>k</b> (Wm <sup>-1</sup> K <sup>-1</sup> ) §§	2.25	2.25	2.25	2.25	2.25	2.25
<b>A</b> (μWm <sup>-3</sup> )	0	0	1.0	0.4	0	0
<b>c<sub>p</sub></b> (J kg <sup>-1</sup> K <sup>-1</sup> )	750	1250	750	750	1250	1250
<b>α</b> (K <sup>-1</sup> )	3.0×10 <sup>-5</sup>	3.0×10 <sup>-5</sup>	3.0×10 <sup>-5</sup>	3.0×10 <sup>-5</sup>	3.0×10 <sup>-5</sup>	3.0×10 <sup>-5</sup>
<b>Density ##</b>						
<b>ρ<sub>0</sub></b> (kg m <sup>-3</sup> )	2950	3250	2800	2900	3250	3250
<b>T<sub>0</sub></b> (°C)	0	1344	200	500	1344	1344
<b>Eclogite ρ<sub>0</sub></b> (kg m <sup>-3</sup> )	3500	—	—	—	—	—
<b>Eclogite T<sub>0</sub></b> (°C)	0	—	—	—	—	—
* Frictional-plastic deformation uses the Drucker-Prager yield criterion: $(J'_2)^{1/2} = P \sin \phi_{eff} + C_0 \cos \phi_{eff}$ , where $J'_2$ is second invariant of the deviatoric stress tensor, P is pressure, $\phi_{eff}$ is effective internal angle of friction, and $C_0$ is cohesion.						
† Softens through a decrease in $\phi_{eff}$ from 15° to 2° over accumulated strain of 0.5 to 1.5 (Beaumont et al., 2006).						
§ Effective viscosity: $\eta_{eff} = f(B^*) I'_2 \frac{1-n}{2n} \exp \left[ \frac{Q+PV^*}{nRT} \right]$ , where $I'_2$ is the second invariant of the strain rate tensor, f is a scaling factor, R is the gas constant, and $B^*$ , n, Q and $V^*$ are the pre-exponential viscosity parameter, stress exponent, activation energy and activation volume, respectively.						
# The rheologies are based on laboratory experiments, including wet quartzite (Gleason and Tullis, 1995), dry Maryland diabase (Mackwell et al., 1998), and wet olivine (Karato and Wu, 1993).						
** Weakening through a decrease in f by a factor of 2 over accumulated strain of 2.0 to 5.0 (Warren et al., 2008).						
†† $B^* = \frac{1}{2} A_{ps}^{-1/n}$ . $A_{ps}$ is the plane strain pre-exponential factor that converted from uniaxial laboratory experimented pre-exponential viscosity parameter ( $A_{uni}$ ). $A_{ps} = \frac{1}{2} (3^{(n+1)/2}) A_{uni}$ .						
§§ Thermal conductivity at temperatures <1396°C; above this, thermal conductivity increases linearly to 54.25 Wm <sup>-1</sup> K <sup>-1</sup> at 1436°C (Pysklywec and Beaumont, 2004).						
## Temperature dependent density: $\rho(T) = \rho_0 [1 - \alpha(T - T_0)]$ , where $\rho_0$ is the reference density at temperature $T_0$ and $\alpha$ is the volumetric thermal expansion coefficient.						

---

## Chapter 6 Controlling factors of inboard deformation

---

### 6.1 Introduction

Continental deformation is one of the tectonic responses that is observed in regions of plate convergence, including subduction and collision zones. Convergence of the two plates results in horizontal compression and leads to orogenic events that include shortening and uplift of the continent. There are two distinct types of deformation associated with mountain building, thin-skinned and thick-skinned deformation, which are based on the involvement of the crystalline basement rocks in the crust (Rodgers, 1949; Pfiffner, 2006). Thin-skinned deformation occurs through shallow thrust faulting that only involves the cover sedimentary rocks, where the faults extend to a depth of 5-8 km (Pfiffner, 2006). Thin-skinned deformation is typical in the foreland fold and thrust belts and may be associated with the development of a basal decollement that limits the depth of deformation (e.g. Pfiffner, 2006; Sarkarinejad and Goftari, 2019). In thick-skinned deformation, the thrust faults cut through the entire continental crust and may extend into the uppermost mantle lithosphere (e.g. Rodgers, 1949; Pfiffner, 2006; Pfiffner, 2017). This type of deformation is less common and is generally associated with regions of arc (e.g. the Andes Mountains) or continent-continent collision (e.g. the Himalayan Mountains), where there are large compressional forces (e.g. Smalley and Isacks, 1990).

In most ocean-continent subduction zones, continental deformation is commonly observed as thin-skinned. However, there are examples of thick-skinned deformation. Two key regions of thick-skinned deformation are found in North and South America, the Laramide Orogeny and the Sierras Pampeanas (Fig. 6.1; e.g. Dickinson and Snyder, 1978;

Jordan and Allmendinger, 1986). In these areas, deformation occurred in the foreland region, hundreds of kilometers from the nearest convergent margin. The origin of deformation so far from the plate boundary is enigmatic.

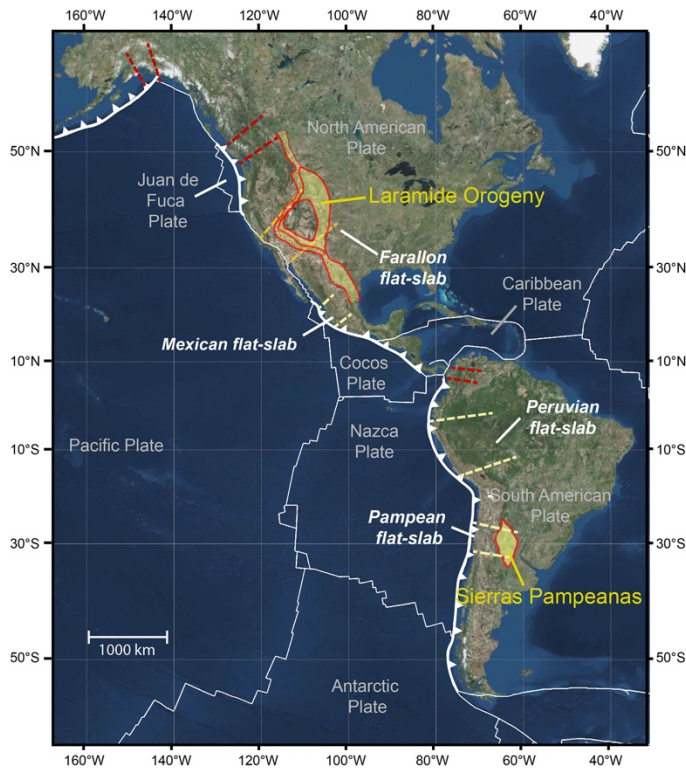


Figure 6.1. Shallow and flat subduction in North and South America. The white lines show the modern subduction zones. The yellow dashed lines show the boundaries of flat-slab regions and the red dashed lines are shallow subduction regions. Yellow shaded areas are areas of inboard thick-skinned deformation. The figure is modified from Figure 3.1.

The Late Cretaceous Laramide Orogeny (~75 Ma to ~40 Ma) was a period of crustal-scale shortening and surface uplift in the western United States (US) and also

extended north to the fold and thrust belt in Canada and Alaska and south to the fold and thrust belt in east-central Mexico (e.g. Dickinson and Snyder, 1978; Bird, 1998; English et al., 2003). In the US, deformation occurred more than 700 km inboard of the convergent margin, which is generally taken to be the Farallon-North America subduction margin. One hypothesis is that the Laramide orogeny developed during an episode of the ancient Farallon flat-slab subduction in the Late Cretaceous (e.g. Dickinson and Snyder, 1978), although there are alternate interpretations such as Cordilleran transpressional collision and westward subduction (e.g., English and Johnston, 2004; Johnston and Borel, 2007; Johnston, 2008; Hildebrand, 2009).

Similar deformation structures are found in South America, in the Sierras Pampeanas of Chile and western Argentina (27-33°S; Fig. 6.1). Here, deformation occurs up to ~1000 km from the Nazca-South America subduction margin and includes basement-cored uplifts (Ramos et al., 2002). This area overlies a region where the subducting Nazca plate has a subhorizontal geometry at ~110 km depth below the continent (Jordan and Allmendinger, 1986). Therefore, it is hypothesized that the flat-slab geometry may have led to Sierras Pampeanas deformation and that this region is the present-day analog of the Laramide Orogeny (Jordan and Allmendinger, 1986).

The inboard crustal-scale deformation for the Laramide and Sierras Pampeanas is generally attributed to subduction of a flat slab beneath the continent. In a normal steep-angle subduction zone, the oceanic plate descends into the mantle at an angle of 30-60°, and there is an asthenosphere wedge above the slab that leads to arc magmatism at 100 km to 300 km from the trench (Dickinson and Snyder, 1978). However, in flat-slab regions, the subducting plate descends into the mantle and then unbends to form a flat geometry at

45-150 km depth below the continent. These regions are often associated with suppressed arc volcanism and anomalous deformation patterns, including reverse faults and basement-cored block uplifts that are found hundreds of kilometers inboard of the plate margin (e.g. Bird, 1988). Previous studies hypothesized that the flat slab increases compressional stresses in the continent through either basal shear traction along the top of the flat slab or end-loading at the distal plate margin (e.g. Dickinson and Snyder, 1978; Bird, 1998).

In addition to the stresses associated with subduction, there may be other factors that contribute to continental deformation. As the subducting slab enters the asthenosphere, the hydrated oceanic crust and mantle undergo metamorphism that releases water and hydrates the mantle wedge and upper plate mantle lithosphere. In flat-slab areas, especially in a cold thermal regime, dehydration reaction may be delayed, and fluids can be carried far inboard of the plate margin (Currie and Beaumont, 2011). The addition of slab-derived fluids to the overlying continent may weaken the continental mantle lithosphere and promote deformation (Humphreys et al., 2003). Further, the upper plate is often composed of heterogeneous blocks of material, where there may be pre-existing weak zones (e.g., terrane suture zones and shear zones), as well as regions that are more prone to weakening by hydration or temperature changes (e.g. Ramos, 1994).

In Chapter 5, we examined the origin of the thick-skinned deformation in the Sierras Pampeanas and found that the deformation occurred under high compressional forces from end-loading at the plate boundary during flat subduction and that deformation concentrated near the pre-existing weak zones. We also showed that the flat slab creates a transient wave of dynamic topography that modulates the stresses in the continent and can explain the observed inboard migration of deformation. In this study, we continue to

investigate inboard thick-skinned deformation related to flat-slab subduction. The objective of this work is to assess the effects of the properties of the weak zone and continental and oceanic structure on deformation.

## **6.2 Numerical model setup**

The 2D numerical models are modified from the models in Chapter 5, in order to simplify the structure so that the effects of parameter variations can be more easily assessed. The model domain is 1800 km wide and 1200 km deep. The initial model geometry is shown in Figure 6.2. The models are set up so that an oceanic plate subducts below a continental plate. The oceanic plate is on the left (western) side of the model. For the reference model, the oceanic plate of the reference model is based on the Nazca plate in South America. It has a thickness of 80 km that is corresponding to a 40 Myr old plate (Stein and Stein, 1992). In later models, we modify the oceanic plate age and test its effect on the inboard deformation. For most of the oceanic plate, the crustal thickness is 8 km. The oceanic plate includes a 600 km wide oceanic plateau, with an 18 km thick oceanic crust. This thickness is set based on both the Juan Fernandez Ridge in the Nazca plate in South America and the Conjugate Shatsky Rise oceanic plateau in the Farallon plate that subducted beneath the North American plate in the Late Cretaceous (e.g. Yáñez et al., 2002; Korenaga and Sager, 2012). The continental lithosphere has a uniform thickness of 120 km, including a 24 km upper crust and 12 km lower crust. In the model tests below, we introduce a block of the weak zone with different widths and thicknesses to the continent.

Materials have temperature-dependent densities and viscous-plastic rheologies. The parameters for density, thermal properties, frictional-plastic deformation and the viscous rheologies used in the reference model are followed those in Chapter 5 (Table 5.1).

The weak zone in the continent is implemented by decreasing the viscous strength of the upper crust, lower crust, and continental mantle lithosphere in this region, by decreasing the scaling factor  $f$  relative to the reference values (Eqn. 2.9; Table 5.1). In this study, we focus on testing how variations in the strength of this weak zone affect continental deformation. For the detailed model parameter setup and methodology, please refer to Chapter 2 and Chapter 5.

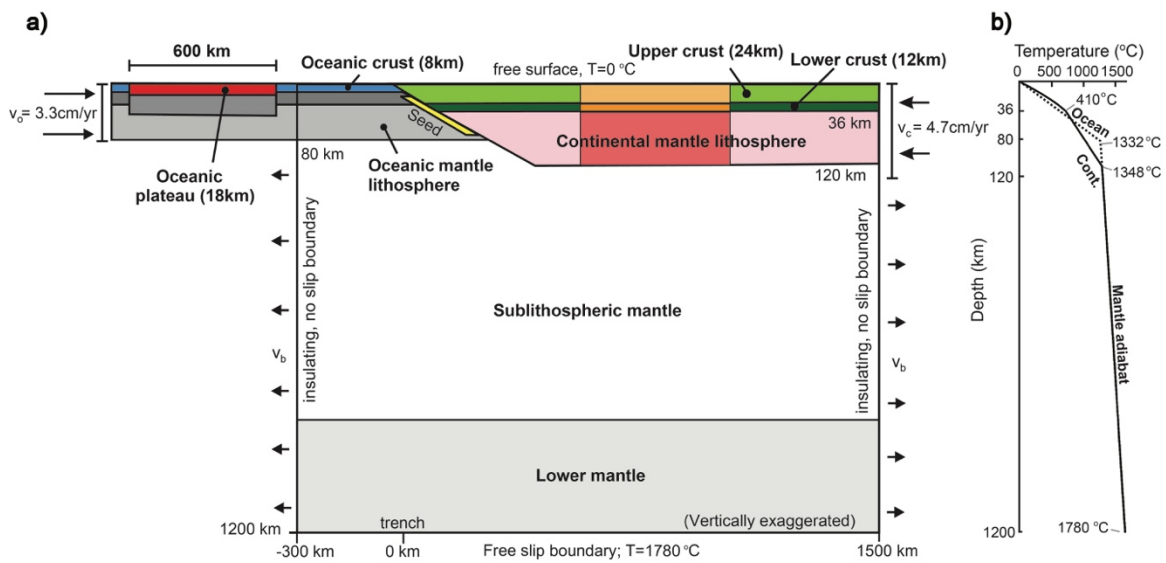


Figure 6.2. a) Initial model geometry and boundary conditions. The orange and red region in the continent is a weak zone. Models examine the effects of variations in its rheology and geometry. b) Initial geotherms for the continental and oceanic plates.

## 6.3 Results

### 6.3.1 Reference model

In this section, a reference model is presented (Fig. 6.3) in which a 500 km wide weak zone is introduced to the continental plate, starting 500 km from the trench (this is indicated by the orange colour in Fig. 6.3). The reference model is modified based on the

model from Chapter 5 (Fig. 5.2b). Within the weak zone, the rheologies of the upper crust and lower crust are a factor of 100 weaker than the adjacent normal crust (Table 5.1). In other words, the weak zone rheologies WQ x 0.5 and DMD x 0.01 for the upper and lower crust, respectively, where WQ is the wet quartzite rheology and DMD is Dry Maryland diabase. The underlying mantle lithosphere and all other materials have the rheologies as listed in Table 5.1. The convergence rate in this model is the same as in Chapter 5, where a constant convergence rate of 8 cm/yr has been applied to the side model boundaries, with 3.3 cm/yr on the oceanic plate and 4.7 cm/yr on the continental plate.

Figure 6.3 shows the evolution of the model geometry and the corresponding surface elevation from 0 to 20 Myr. The model starts with steep-angle subduction. As the oceanic plateau enters the trench, the slab gradually develops a flat geometry, with the onset of the shallowing at ~ 5 Myr. This follows the same trend that was observed in the previous chapters. During the 20 Myr model run, shortening, buckling, and surface uplift occur within the weak zone region (Fig. 6.3). There is a total of 28 km shortening during the 20 Myr (Fig. 6.4c). Shortening starts at ~ 5 Myr, which corresponds to the time at which the slab geometry starts to flatten. Figure 6.3b shows the maximum shear stress of the model. As the oceanic plateau enters the trench, the flattening of the slab increases the maximum shear stress in the continent through end-loading. As described in the previous chapter, the increased stress exceeds the yield stress in the weak zone part, which leads to deformation (Fig. 5.3).

In order to quantitatively examine the scale and location of the deformation, we plot the strain rate at the continental surface in Figure 6.4a. The strain rate in the weak zone increases at ~5 Myr as slab flattening begins. The strain rate increases evenly across the

weak zone at this time. This is consistent with our conclusion from the previous chapter that end-loading results in a regional increase in compressional stress, rather than continental compression created by the upward stress transfer from the slab surface. Starting at  $\sim 7$  Myr, strain rates on the western (i.e., trenchward) side of the weak zone decrease, and the zone of low strain rates expands toward the east over time. We propose that this change is related to the eastward migration of the oceanic plateau beneath the continent. Figure 6.4b shows the surface elevation for a model with a flat slab subducting below a uniform (no weak zone) continent (the model is shown Fig. 6.5b). As the plateau moves eastward, there is a transient surface uplift above the oceanic plateau location. This matches with the location and time of the pause of the deformation. As discussed in Chapter 5, the surface uplift results in horizontal extension in the continent surface, which compensates for the increased compression from end-loading. This results in the pause of the deformation.

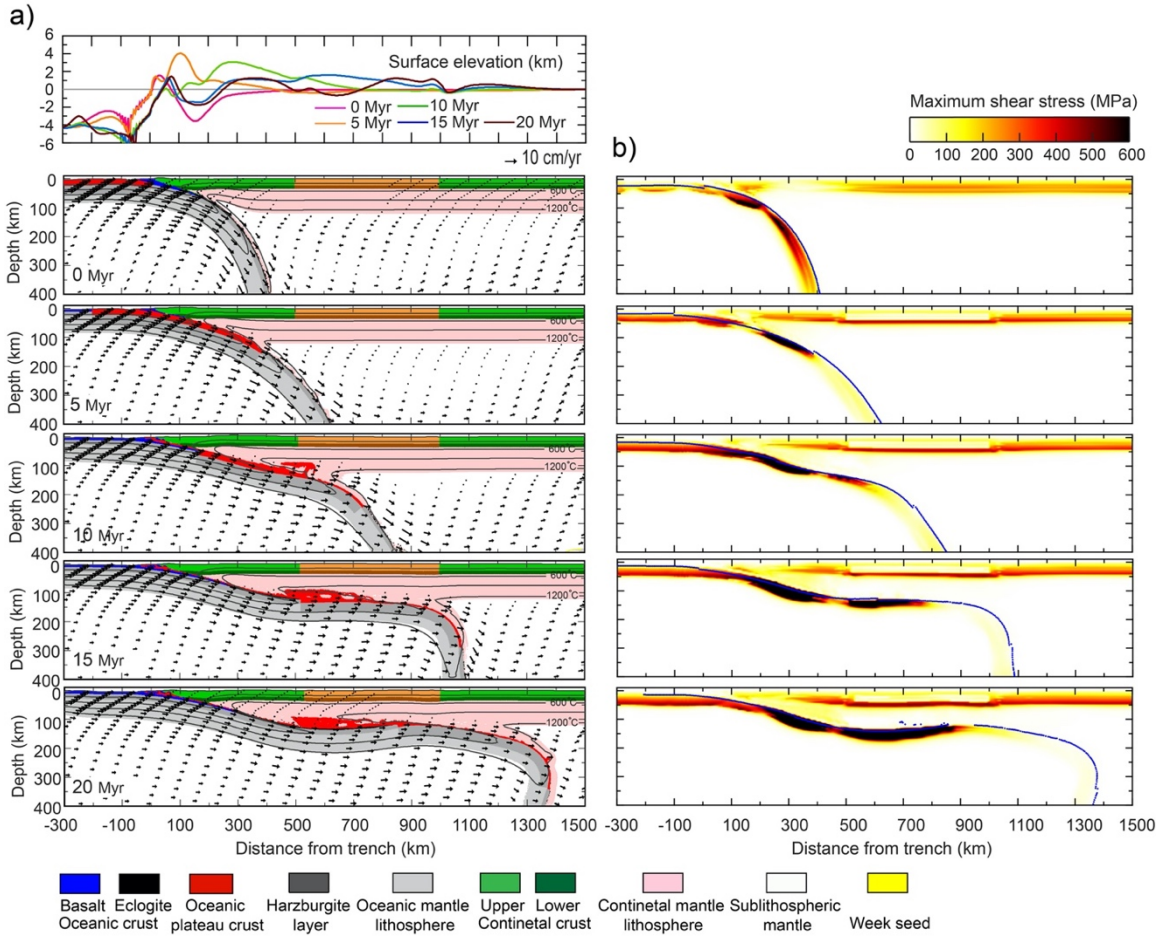


Figure 6.3. Reference model. (a) Model evolution from 0 to 20 Myr along with the surface elevation (top plot). (b) Maximum shear stress for the model. The dark blue dots track the position of the oceanic Moho.

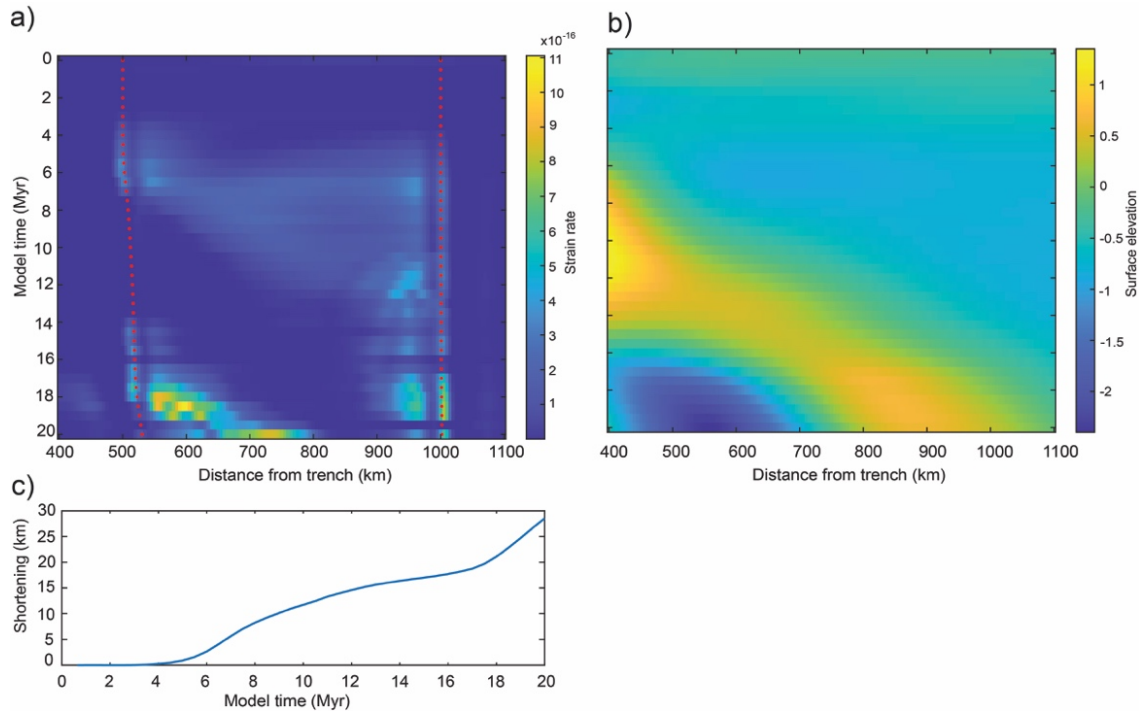


Figure 6.4. (a) Strain rate at the surface for the reference model. Red dots mark the position of the edges of the continental weak zone. (b) Surface elevation for a model with flat-slab subduction below a continent with no weak zones (model shown in Fig. 6.5b). (c) Horizontal shortening of the weak zone of the reference model during the 20 Myr model run.

### 6.3.2 Effects of presence of weak zone and flat-slab subduction

In the reference model, two factors allow for continental deformation: the presence of the continental weak zone and the development of the flat slab. In this section, we present models that investigate each factor individually. Figure 6.5a shows a model with steep-angle subduction under continent with weak zone (Fig 6.5a) and Figure 6.5b shows a model with flat-slab subduction under a uniform continent (with no weak zone). In Figure 6.5a, there is continued steep-angle subduction (no flat slab) and the upper and lower crust of the weak zone are 100x weaker than the reference values; this is the same weak zone rheology as the reference model. In this model, there is no oceanic plateau, and therefore,

there is not enough buoyant force to cause flat subduction (e.g. van Hunen, 2002; Liu and Currie, 2019). The slab dip becomes shallower during the model because of the high continental trenchward velocity, but it never reaches a flat geometry. The surface elevation does not vary in the continental interior, and there is a slight subsidence above the part of the continent where the slab is coupled with the continental lithosphere. This is caused by the subducting dense slab. In Fig. 6.5b, a flat slab develops below a uniformly strong continent. The surface topography in this model shows a region of uplift that moves inboard due to the buoyant oceanic plateau. There is no continental deformation in either model.

Figure 6.5d compares the shortening in between 500 km and 1000 km from the trench (the weak zone region) of these two models and the reference model. With a single factor, a flat slab or the existence of weak zone alone, there is a negligible amount of shortening of the continent ( $<5$  km), whereas the reference model with both factors has  $\sim 28$  km of shortening. Based on the results so far, inboard deformation does not occur in models in which either the continent is strong or there is normal (steep) angle subduction. Deformation requires both a long flat slab and a pre-existing weak zone in the continent, which is consistent with the findings from Chapter 5.

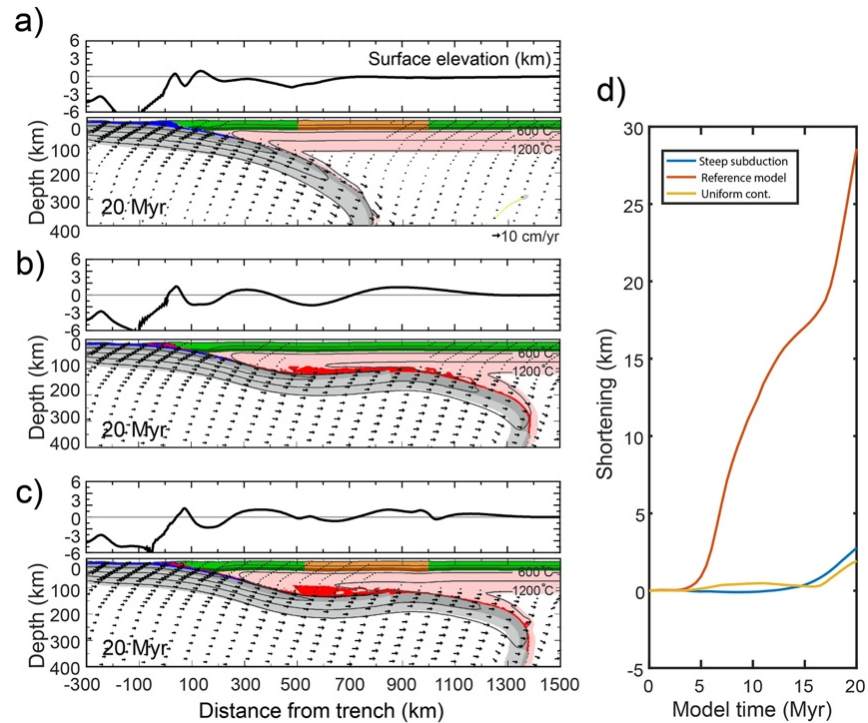


Figure 6.5. Model geometry at 20 Myr for (a) steep-angle subduction with continental weak zone (orange region), (b) a flat-slab subduction without the weak zone, and (c) flat-slab subduction with the weak zone (reference model). (d) Comparison of the shortening between 500 km and 1000 km from the trench (in the area of the weak zone) for the three models.

### 6.3.3 Weak zone depth and mantle lithosphere strength

In this section, we examine how the weak zone depth and mantle lithosphere rheology might affect the scale of continental deformation. For these models, the rheologies of the weak zone upper crust and the lower crust are the same as in the reference model (WQ x 0.5 for the upper crust and DMD x 0.01 for the lower crust). Figure 6.6 and Figure 6.7b examine the depths of the weak zone. In this set of models, we test models with a weak zone that cuts through (1) the upper crust, (2) upper and lower crust, and (3) the entire crust plus mantle lithosphere to assess their effects on inboard deformation.

When the weak zone is in the upper crust only, the underlying lower crust has the same strength as the adjacent regions (DMD x 1).

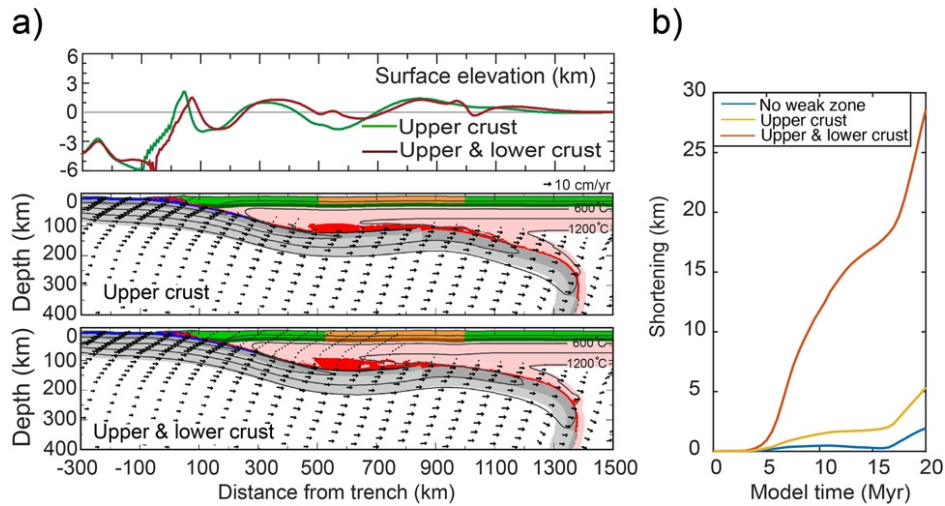


Figure 6.6. (a) Model geometry at 20 Myr for a model with a weak zone in the upper crust only and the reference model with weak zone through the whole continental crust. The top plot shows the surface elevation at 20 Myr for the two models. (b) Comparison of weak zone shortening for the two models, as well as the model with a flat slab but no weak zone (model shown in Fig. 6.5c).

Figure 6.6a shows the model with the weak zone in the upper crust only and in the upper and lower crust. A comparison of the amount shortening shows that the model with the upper crustal weak zone has ~3 km more shortening than the model without a weak zone (Figure 6.6b). If the weak zone extends to the continental Moho (i.e., the reference model), the amount of shortening increases by ~25 km compared to the model with no weak zone. The results agree with the conclusions in Chapter 5 that the weak zone must cut through the whole continental crust (high yield strength region) to allow a larger amount of deformation to occur.

To examine the role of the continental mantle lithosphere strength on inboard deformation, we extend the weak zone to the depth of the lithosphere-asthenosphere boundary. In the reference model, the mantle lithosphere strength is  $WO \times 10$ , where  $WO$  is wet olivine. The model shown in Figure 6.7a has the mantle lithosphere strength weakened by a factor of 2 ( $WO \times 5$ ) in the weak zone. In this model, there is a greater amount of shortening ( $\sim 170$  km) compared with the reference model with weak zone only existing in the crust ( $\sim 28$  km). Figure 6.7b shows a model with the weak zone mantle lithosphere having a rheology of  $WO \times 1$  (i.e., 10 times weaker than the reference model). Here, we observe  $>400$  km of shortening since the flattening of the slab. At  $\sim 8$  Myr, the weak mantle lithosphere starts to peel from the rest of the mantle lithosphere. As the weak zone crust shortens, the weak mantle lithosphere is underthrusting and then detaches from the continent, sinking into the lower mantle. In addition, there is a great amount of buckling of the weak lower crust. The strong normal crust from the two sides converges and shortens the weak crust. With continued convergence, the strong continental crust underthrusts the weak region, with the two sides colliding with each other. This causes significant surface uplift in this region.

In Figure 6.7c, the model has a very weak mantle lithosphere ( $WO \times 1$ ), the same as the model in Figure 6.7b. However, in this model, the weak materials are only in the mantle lithosphere, and the continental crust is strong everywhere. With the development of the flat slab, the lower portion of the weak mantle lithosphere is scraped by the slab. This leads to some shortening ( $\sim 40$  km) and uplift of the weak part, but the amount of deformation is much less than that of the model in Figure 6.7b.

Based on the models in Figures 6.6 and 6.7, continental deformation is controlled by the strength of the weak zone, with a greater amount of deformation for weaker materials. The strengths of the lower crust and mantle lithosphere are important in controlling the scale of deformation, as these are at the depths where the continent has a high yield strength, as discussed in Chapter 5. Therefore, the lower crust and the mantle lithosphere work as a stress-bearing layer, in which the high-strength mantle lithosphere prevents significant shortening of the weak zone, even with a very weak lower crust; it is also true that shortening is inhibited with a high-strength lower crust.

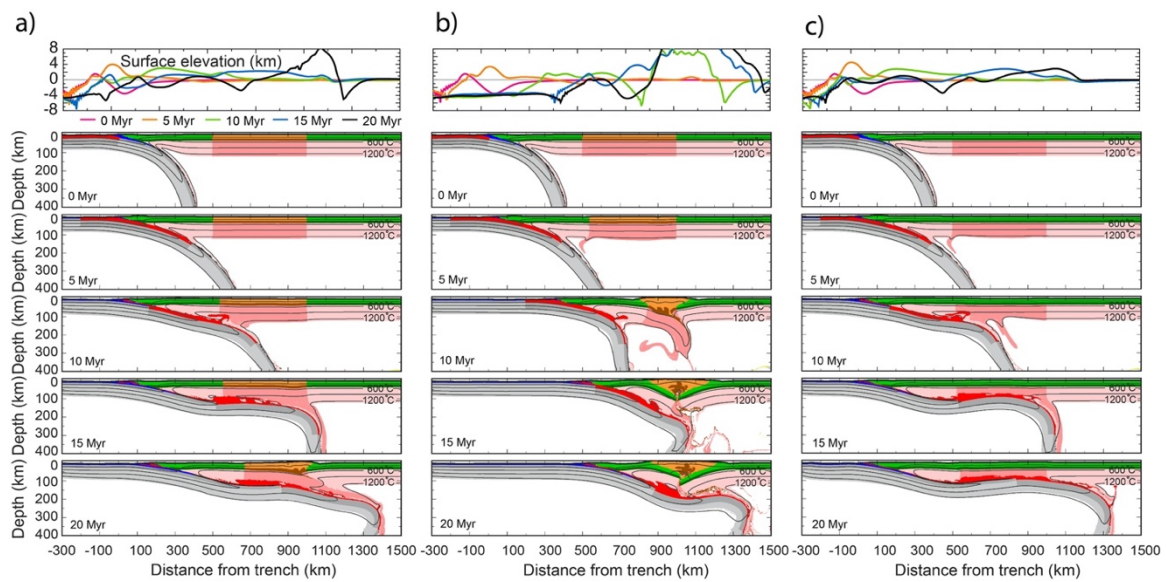


Figure 6.7. Model evolution from 0 Myr to 20 Myr for (a) a model with a weak zone from the surface to the base of the lithosphere, where the weak mantle lithosphere rheology is  $WO \times 5$ , (b) a model with a weak zone from the surface to the base of the lithosphere, where the weak mantle lithosphere rheology is  $WO \times 1$ , and (c) a model with a weak zone only in the continental mantle lithosphere that has a rheology of  $WO \times 1$ .

#### 6.3.4 Weak zone locations and widths

In this section, the location and width of the weak zone are examined to test their effects on continental deformation. In this set of models, the weakening is applied to the upper and lower crust of the weak zone using the parameters of the reference model. We have run models with the left boundary of the weak zone located at 300 km, 500 km (reference model), and 700 km from the trench with the same weak zone width of 500 km. Figure 6.8 shows that within the 20 Myr model run, the three models with different weak zone locations have a similar amount of shortening (22-28 km). However, the timing of the shortening is different. A weak zone that is farther away from the trench is affected by the growing flat slab later. As shown in the plot of shortening (Fig. 6.8), there is an earlier pause in the shortening (i.e., the line becomes flatter) for a model with weak zone closer to the trench as the dynamic uplift due to the buoyant plateau affects these regions earlier. Once the buoyant plateau passes the weak zone, the weak zone is underlain by a denser slab and this causes dynamic subsidence that enhances crustal compression and an increased rate of shortening.

To test the effect of the size of the weak zone, we have run models with weak zone widths of 300 km, 500 km (reference model), 700 km, and 1000 km, with the left boundary of the weak zone at 500 km from the trench for all models. All three models show the same deformation pattern, where deformation is located near the weak zone boundaries. Figure 6.8 compares the amount of shortening between the four models, showing there is a greater amount of shortening when the weak zone is wider. This might be because the strain rate for the weak zone is similar, and therefore during the same time, there is a great amount of shortening for a wider weak zone.

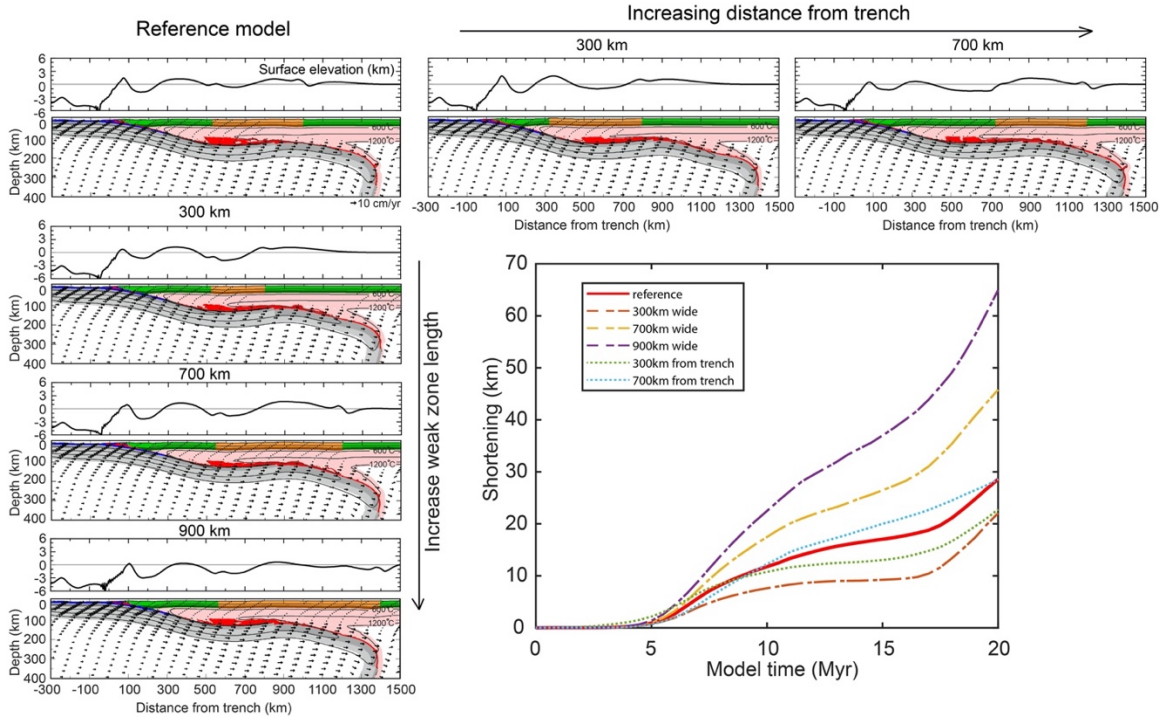


Figure 6.8. Model geometry at 20 Myr for models with different weak zone locations (top row) and different weak zone widths (left column). The lower right plot shows the amount of weak zone shortening for the models.

### 6.3.5 Thickness of continental lithosphere

In this section, we compare models that have initial continental thicknesses of 80 km, 120 km (reference) and 160 km. The initial thickness of the continent decides the temperature structure, such that a thin continental lithosphere has high crustal temperatures (Fig. 6.9b). The strength of the continental lithosphere is dependent on the temperature profile; as the temperature increases, the viscous strength decreases and therefore overall strength is lower. Figure 6.9c shows the effective viscosity of the weak zones of the three models. Within the crust and mantle layers, the effective viscosity is lowest at larger depths owing to higher temperatures. The weak zone viscosity (weak crust viscosity) of the model

with an 80 km thick continent has relatively low values of  $10^{20}$  -  $10^{22}$  Pa·s, while the weak zone viscosity of the model with a 160 km thick continent has a viscosity of  $10^{23}$  -  $10^{28}$  Pa·s.

Figure 6.9a shows the model geometry at the end of the 20 Myr model run. The different continental thicknesses result in different amounts of deformation. Due to the high temperatures and low strength, the model with an 80 km thick continent has the greatest amount of shortening (~500 km) and uplift (>6 km) during the 20 Myr model run. In comparison, the model with the thickest continent (160 km) has a negligible amount of deformation during the same model run, even though the weak zone cuts through the entire continental crust. Owing to the low temperatures, this model has a thick region of cool, strong mantle lithosphere, and therefore it is too strong to be deformed by the compressional stresses created by the flat slab. This is consistent with the earlier conclusion that the amount of deformation depends on the strength of the continent, which in turn depends on the continental rheology and temperature structure.

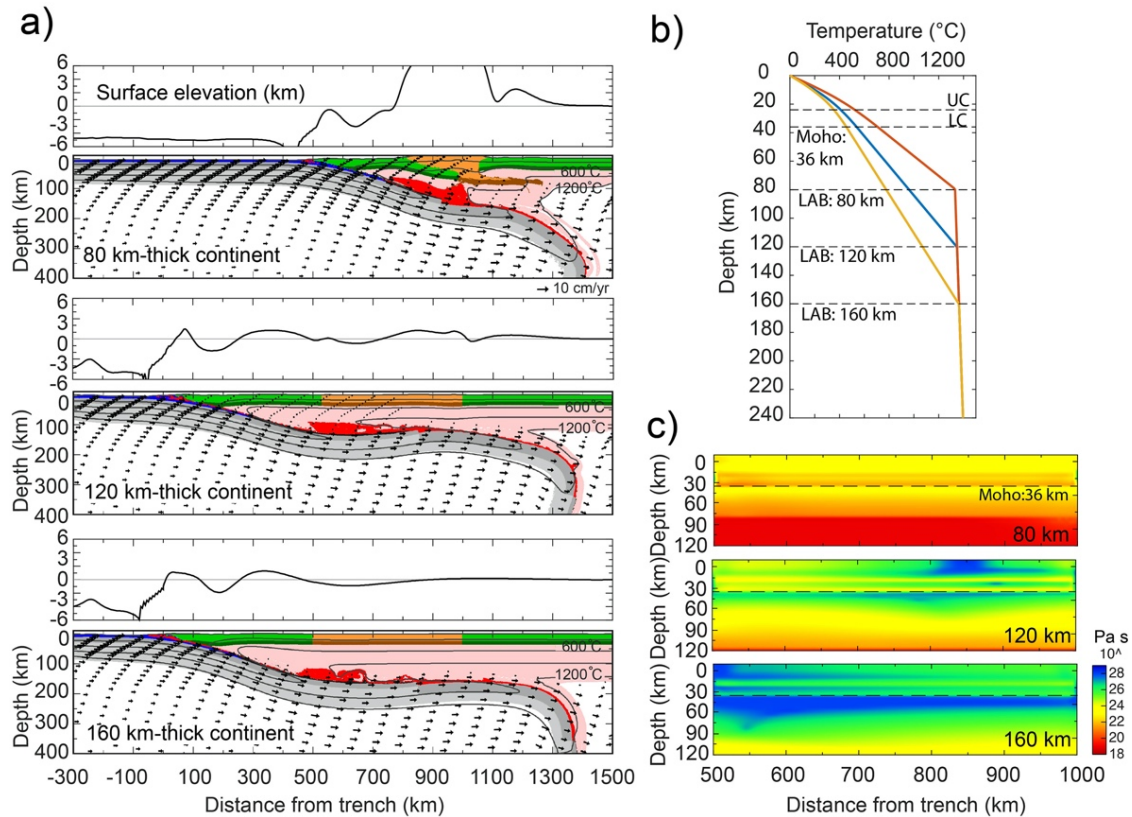


Figure 6.9. (a) Model geometry at 20 Myr for models with initial continental thicknesses of 80 km, 120 km (reference model), and 160 km. (b) Initial geotherms of the three models. UC is the upper crust, LC is the lower crust, and LAB is the lithosphere-asthenosphere boundary. (c) Effective viscosity of the weak zone of the three models at the beginning of the model run (0 Myr).

### 6.3.6 Oceanic plate age and convergence rate

The models in the previous sections have an 80 km thick oceanic plate that corresponds to an oceanic plate with an age of 40 Ma. However, there are flat-slab regions where the oceanic plate is older than this. For example, the Farallon flat slab in North America had >100 Ma oceanic plate (e.g. Usui et al., 2003). This flat slab is associated with a wide region of thick-skinned deformation, the Laramide Orogeny, that is over 700 km away from the plate margin (e.g. Dickinson and Snyder, 1978; Copeland et al., 2017).

To demonstrate the effect of the subducting plate age on continental deformation, we present a model with a 90 km thick oceanic plate, corresponding to an age of 100 Ma.

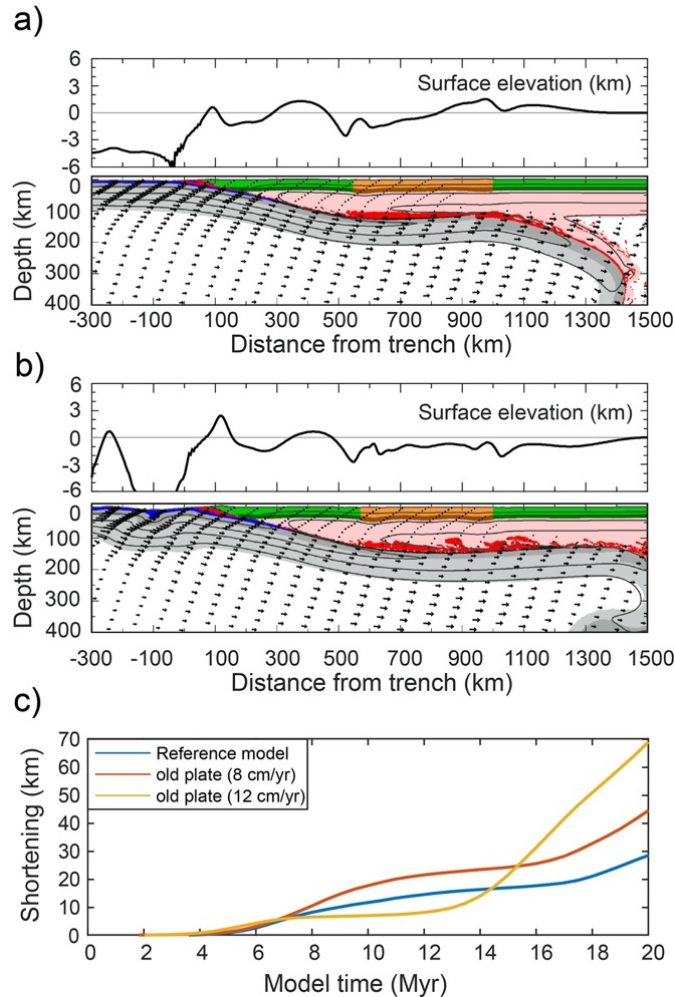


Figure 6.10. Model geometry at 20 Myr and the corresponding surface elevation for (a) a model with a 100 Ma oceanic plate and convergence rate of 8 cm/yr and (b) a model with a 100 Ma oceanic plate and convergence rate of 12 cm/yr. (c) Comparison of the continental shortening of the reference model (Fig. 6.3), the model in (a), and the model in (b).

Figure 6.10a shows the model with a 90 km thick oceanic plate after 20 Myr. All the other parameters are the same as those in the reference model. The overall dynamics

are similar to the reference model, where the deformation is concentrated at the weak zone boundaries and there is dynamic uplift that migrates inland due to the underlying buoyant plateau. The amount of weak zone shortening over time is plotted in Figure 6.10c. During the 20 Myr model run, the model with the older plate has ~16 km more shortening than the equivalent model with a younger plate.

In Figure 6.10a, the flat slab has a slight deeper depth of 100-110 km than that of the model with younger plate in the reference model (90-100 km deep; Fig. 6.3a). This is because that the oceanic plateau crust of the young plate got scraped and accumulated beneath continent near the trench. Considering that an older plate causes a greater amount of deformation, our result once again indicates that the compression due to the flat-slab subduction is from end-loading at the plate margin, rather than basal shear traction from the top of the slab. If basal shear was significant, stresses from a deeper slab should take longer to affect the surface and therefore should result in less deformation. The greater amount of shortening for the model with an older plate is due to the higher compression at the plate margin (Fig. 6.11) compared to that for the young plate (Fig. 6.3b). This appears to be due to the wider contact area between the plates, as the older oceanic lithosphere has a slightly shallower dip. This may be because the plate is thicker, cooler and stronger and therefore does not bend as easily.

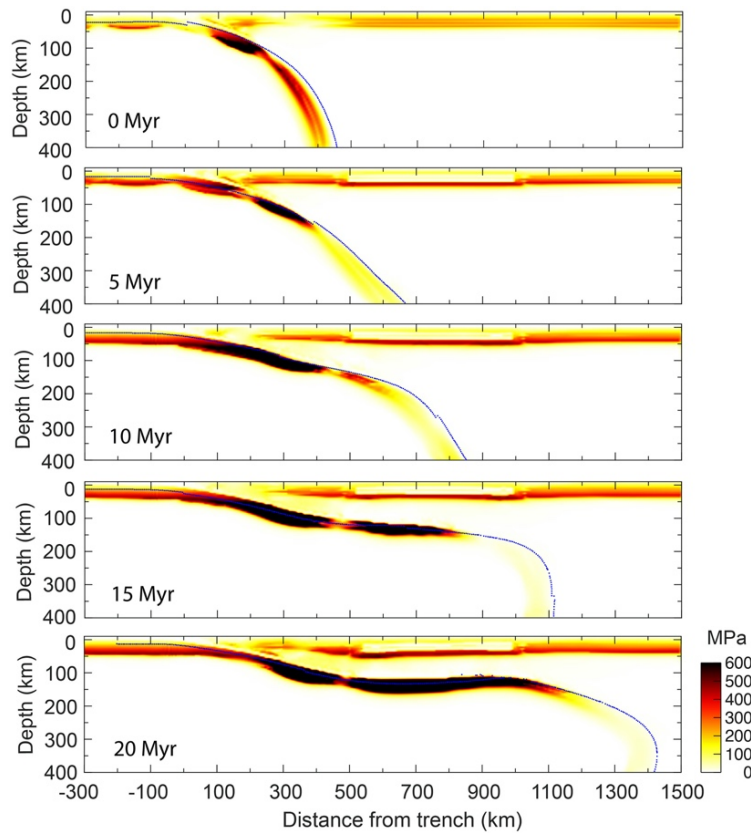


Figure 6.11. Maximum shear stress for the model in Figure 6.10a. The dark blue dots indicate the oceanic Moho locations.

Another factor that may be important is the rate of plate convergence. The convergence rate between the Farallon plate and the North America plate in the Late Cretaceous was  $\sim 12$  cm/yr (e.g. Torsvik et al., 2008). To test the effect of a higher convergence rate on continental deformation, we have run the model shown in Figure 6.10a with a convergence rate of 12 cm/yr (8 cm/yr on the oceanic plate and 4 cm/yr on the continental plate). During the 20 Myr model run, there is  $\sim 2400$  km convergence for a high convergence rate (12 cm/yr) in comparison to 1600 km convergence for the model with the reference convergence rate of 8 cm/yr. Figure 6.10b shows the model geometry at 20 Myr. By this time, the buoyant oceanic plateau has passed below the weak zone, and the weak

zone region is an area of subsidence due to the dense slab underneath. The record of shortening (Fig. 6.10c) shows that there was a time of limited shortening from ~7 to ~13 Myr, coinciding with the time when there was dynamic surface uplift, followed by more rapid shortening as compression due to subsidence enhances the compression from the flat-slab subduction. The results show that the deformation is concentrated at the boundaries of the weak zone, with less buckling in the middle part of the weak zone.

#### **6.4 Discussion and conclusions**

Based on the model results, we find that both the continental lithosphere and the oceanic lithosphere structure have an effect on the extent of continental deformation above a flat slab. If the slab has a steep-angle geometry, the compressional stresses associated with subduction are not large enough to induce deformation, even if there are weak zones in the continent. Deformation is also inhibited for a flat-slab subduction zone if the continent is uniform and strong. Therefore, large-scale deformation in the continental interior results from combined effects of high compression due to the flat slab and the pre-existing weak zones. In our models, the compressional stresses originate from end-loading at the plate margin once the flat slab forms. Our models show that the lower crust and mantle lithosphere play an important role in controlling continental interior deformation, as these are the regions where the continental strength is highest. This is consistent with the results of Heron et al. (2016) who argue that a strong layer in the continent acts as a stress-bearing layer that prevents deformation. The width of the weak zone also controls the rate of deformation, as a wider weak zone has a higher shortening rate and accommodates a greater amount of shortening. The age of the subducting plate and the convergence rate affects the horizontal stress in the continent. A thicker oceanic plate due

to an older lithosphere or higher convergence rate causes higher compressional stresses in the continent. This leads to a greater amount of deformation.

In addition, the initial temperature structure of the continent plays an important role in continental deformation. The temperature structure determines the overall strength of the continent, as higher temperatures reduce the viscosity of crust and mantle materials, making them prone to deformation. This means that deformation is also sensitive to local temperature and rheological changes, such as those from magmatic activities and hydration associated with flat-slab subduction. This is consistent with previous studies that argue that thermal weakening due to migration of arc magmatism and expansion of slab dehydration with a growing flat slab leads to the migration of deformation from the convergent margin to the continental interior (e.g. Ramos et al., 2002; Humphreys et al., 2003).

Our results provide further insights into the Laramide Orogeny of North America and the Sierras Pampeanas of South America. Please refer to Chapter 5 for the initial discussion for the two regions. Here, we will show some comparisons between the two areas. During the Laramide Orogeny, the continent underwent ~200 km of shortening (Bird, 1998), which is greater than that of the Sierras Pampeanas (~90 km; e.g. Bellahsen et al., 2016). Our models show that an older and thus thicker oceanic plate causes greater compression in the continent (Fig. 6.11). In addition, the convergence rate between the Farallon Plate and North America Plate was 12 cm/yr and flat-slab subduction lasted about 40 Ma in the Late Cretaceous (e.g. Bird, 1988; Torsvik et al., 2008). The faster convergence in the Laramide region and a longer flat-slab subduction period would lead to a greater amount of deformation and crustal shortening (Fig. 6.10).

Migration of deformation from the regions near the convergent margin to the continental interior occurred in both the Laramide Orogeny and the Sierras Pampeanas (e.g. Ramos et al., 2002; Copeland et al., 2017). As shown in Chapter 5, the migration of deformation above a flat slab is modulated by the migrating topographic uplift due to the passing buoyant oceanic plateau. In addition, the migration of deformation in both areas correlates with the migration and expansion of magmatism (e.g. Dickinson and Snyder, 1978; Ramos et al., 2002). Magmatic activity increases the temperature of the continental crust, which should decrease its viscosity and make it more susceptible to deformation. This is consistent with our results (Fig. 6.9) showing that a lower viscosity tends to have a greater amount of deformation.

Compared with the Sierras Pampeanas, the Laramide Orogeny affected a wider region. Except for the main thick-skinned deformation in the central-western US, the Laramide-aged deformation also extended northwest to the thin-skinned deformation in western Canada and Alaska and extended south to the fold and thrust belt in east-central Mexico (Fig. 6.1; e.g. Dickinson and Snyder, 1978; Bird, 1998; English et al., 2003; English and Johnston, 2004). The basement-cored uplift in the western US is more likely to be caused by the long (>1000 km) Farallon flat-slab subduction (Dickinson and Snyder, 1978; Bird, 1998; Heller and Liu, 2016). Except for the high compression caused by flat subduction, slab-related dehydration and magmatism may lead to a weakened continental lithosphere which is easier to get deformed (e.g. English et al., 2003; Humphreys et al., 2003). However, in both Mexico and western Canada, there was no flat-slab subduction during the Laramide time, and therefore the deformation here must be attributed to other mechanisms (e.g. English and Johnston, 2004; Johnston, 2008). Despite the fact that there

were terrane accretions history in both Mexico and western Canada (Coney et al., 1980; Monger et al., 1982), geological evidence shows that terrane accretion does not play a role in the deformation here (e.g. Martini et al., 2009). Other driving forces that lead to the thin-skinned deformation of the Laramide Orogeny in Canada and Mexico), such as increasing subduction rate from the west coast (e.g. Martini and Ferrari, 2011) and an alternative mechanism that the end of the westward subduction of an oceanic crust under the Cordilleran ribbon continent caused high compression and uplift of the continent (e.g. Johnston and Borel, 2007; Hildebrand, 2009).

In summary, our models show that flat-slab subduction can lead to a large scale of deformation in the continental interior. This depends on many factors. The flat slab leads to high compressional stresses within the continent due to end-loading. Deformation also requires that the continental is weak enough to deform under these stresses. In our models, deformation is localized within a pre-existing weak zone. The models also show that both the structure of the continental plate (e.g., weak zone size and location, and the initial temperature structure) and the structure of the oceanic plate (e.g. age of the oceanic plate) and the convergence rate also affect the scale of the deformation through either changing the strength of the continental plate or changing the compressional force between the two plates.

---

## Chapter 7 Conclusion

---

This thesis aims to advance our understanding of subduction processes, especially in areas of flat-slab subduction, and addresses the fundamental question of how continental topography and deformation are affected by the subduction process. Subduction zones are the largest recycling system of the Earth, involving consumption and descent of oceanic plates deep into the mantle. Earth's most devastating earthquakes, largest volcanoes, and significant mountain belts are caused by subduction (Turcotte and Schubert, 2022). The geometry of the descending oceanic plate affects the location and magnitude of these geologic hazard events. A special type of subduction is flat-slab subduction, where the oceanic plate travels horizontally directly below the continent for hundreds of kilometers. This can lead to termination or migration of arc volcanism and propagation of crustal deformation far inland of the plate margin (e.g. Coney and Reynolds, 1977; Dickinson and Snyder, 1978; Kay and Abbruzzi, 1996; Gutscher et al., 2000a; Ramos et al., 2002; G erault et al., 2015; Copeland et al., 2017). Flat-slab subduction is observed in 10% of modern subduction zones (Gutscher et al., 2000a). The landscapes of both western North and South America have been greatly affected by episodes of flat-slab subduction. In this thesis, I examine the dynamics of flat-slab subduction using 2D numerical models that are based on observed flat-slab regions in both North and South America. The models provide an experimental framework for exploring the dynamics of flat subduction and make quantitative predictions that can be tested against geological and geophysical observations.

## 7.1 Conclusions

This thesis investigates three key aspects of flat-slab subduction and the interactions between the flat slab and overriding plate (Fig. 7.1):

1. Controls on flat-slab depth (Chapter 3)

Chapter 3 examines the factors that control the depth at which a flat slab forms. This study is motivated by the observations that show that natural flat slabs are found at a range of depths. In some areas, the flat slab is shallow and is found right below the continental crust, where it may even have displaced the lowermost crust (45-60 km, e.g. Mexican flat slab and Peruvian flat slab; Kim et al., 2012; Bishop et al., 2017). In other areas, the flat slab is well below the Moho, with a depth of over 100 km (e.g. Farallon flat slab in the Late Cretaceous; Usui et al., 2003; Liu et al., 2008). Numerical models are used to examine the effects of continental and oceanic structures on flat-slab depth. The results show that the depth of a flat slab is primarily controlled by continental structure, and the oceanic plate parameters (age and subducting velocity) have less influence on the slab depth. A shallow flat slab occurs when the initial overriding continental plate is thin, as the slab is able to displace the lower hot and weak mantle lithosphere due to the temperature-dependent mantle lithosphere rheology. The strength of the continental mantle lithosphere plays a secondary role in controlling flat-slab depth, with a shallower slab for a weaker mantle lithosphere. A flat slab is able to displace a great thickness (up to 50%) of the deep mantle lithosphere, which corresponds to temperatures as low as  $\sim 900^{\circ}\text{C}$ . The models provide possible explanations for the observations in flat-slab regions. Shallow flat slabs observed in Mexico and Peru must have resulted from an anomalously thin continent prior to the flat-slab emplacement. The model results also have implications for the observations

in the Wyoming craton in the western United States. It is suggested that a long Farallon flat slab in the Late Cretaceous was able to reach the Wyoming craton region and displaced the bottom of the craton root.

## 2. Cooling effects of a flat slab (Chapter 4)

Chapter 4 assesses temporal variation in the continental thermal structure during the development of a flat slab. This study is motivated by observations of low surface heat flow in the flat-slab regions (20-70 mW/m<sup>2</sup>; Henry and Pollack, 1988; Hamza and Muñoz, 1996; Marot et al., 2014; Sánchez et al., 2018); in comparison, heat flow is higher above areas of normal-angle subduction (80±20 mW/m<sup>2</sup>; Hyndman et al., 2005; Currie and Hyndman, 2006; Wada and Wang, 2009). The low heat flow above a flat slab is commonly attributed to the cooling of the continental plate by the cold oceanic plate at its base (e.g. Dumitru et al., 1991; van Hunen et al., 2004). However, our results show that the conductive cooling of the continent takes 10's of millions of years, whereas modern flat slabs have only been in place for <20 Ma. We find that the flat-slab depth is the primary control on the timescale of continental cooling, and there is a delay in cooling with a lag time range from 4 to 32 Myr for slabs at 50 to 120 km depth. A longer-lived flat slab and faster convergence rate both enhance continental cooling.

Our results imply that the low surface heat flow in Mexico and Peru region are likely associated with the underlying flat slabs, as the Mexican flat slab and Peruvian flat slab are at shallow depth (45-60 km). However, in the Pampean region (flat-slab depth of ~110 km) our models show that conductive cooling due to the flat slab cannot fully explain observations of low surface heat flow. Additional cooling mechanisms are needed. One possibly cooling mechanism are fluids-related thermal alteration due to slab dehydration.

3. Deformation in the continental interior during flat-slab subduction (Chapter 5 and Chapter 6)

Chapter 5 and Chapter 6 investigate the origin of thick-skinned deformation in the continental interior. Crustal scale shortening and uplift are observed in the Sierras Pampeanas in South America and the Laramide Orogeny in North America, which are regions that are hundreds of kilometers away from the convergent margin (e.g. Jordan and Allmendinger, 1986; Bird, 1998). The thick-skinned deformation appears to be related to the coeval flat-slab subduction in these regions, but the relationship between flat-slab dynamics and continental deformation is not well understood. Chapter 5 focuses on the Sierras Pampeanas region using models that are designed to represent Pampean flat-slab subduction. The models show that as a flat slab develops, the continent experiences compressional stress through end-loading at the plate margin. Deformation is localized within pre-existing weak zones (suture zones and shear zones) in the continent. The deformation is also controlled by dynamic topography, where the inboard migration of deformation in the Sierras Pampeanas can be explained by the passage of the subducted buoyant Juan Fernandez Ridge which leads to a transient surface uplift that inhibits the deformation.

Chapter 6 continues the study of flat-slab subduction and continental deformation that occurs far from the convergent plate margin. Building on the models in Chapter 5, Chapter 6 examines how inboard deformation is affected by the properties of continental weak zones and variations in continental and oceanic structure. The results confirm the findings of Chapter 5 that continental deformation requires both flat-slab subduction and pre-existing weak zones. For deformation to occur, the weak zones need to cut through the

whole continental crust and possibly the uppermost mantle lithosphere; this is because of the high rock strength in the lower crust and the shallow mantle lithosphere. The width and location of the weak zone, continental lithosphere thickness, and the age and velocity of the subducting plate also affect the scale of deformation by changing either the compressional force in the continent or the strength of the weak zone.

In summary, this thesis provides detailed dynamic modelling studies of flat-slab subduction and advances our understanding of subduction dynamics and the relationship between flat subduction and continental evolution, including thermal structure, dynamic topography, and orogenic events. It also provides insights into the complex tectonic history of the Sierras Pampeanas in South America and the Laramide Orogeny in North America. The work presented here may also spark new studies on subduction-related issues such as magmatism and surface erosion, as well as subducting slab and mantle interaction.

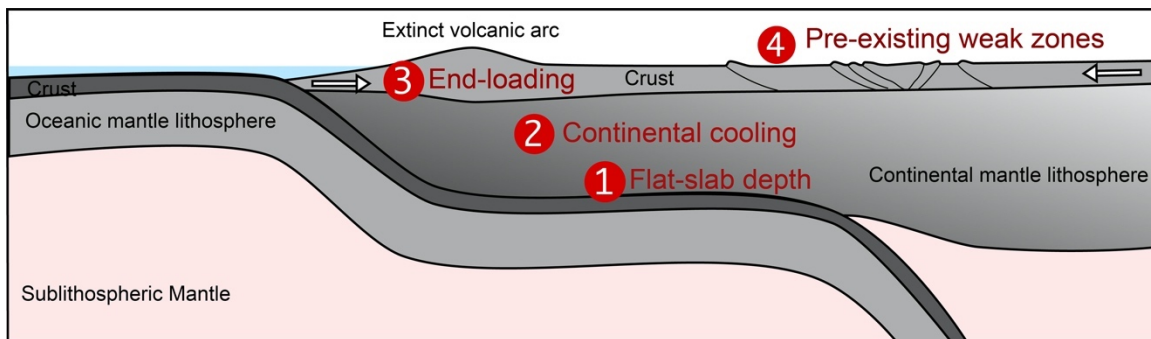


Figure 7.1. Summary of the key findings in this thesis. (1) Flat-slab depth is mainly dependent on the continental structure (e.g. thickness and rheology). (2) Flat slab cools the overlying continent through thermal conduction over 10's Myr. (3) Compression in the continent due to flat slab is through end-loading. (4) Compression leads to deformation near the pre-existing weak zones.

## 7.2 Future work

All the models in this thesis are limited to a 2D modelling domain. The 2D models provide perspectives on how a subducting plate can evolve into a flat geometry and the effects on the overlying plate. However, they do not assess how along-strike processes may affect the dynamics. The flat-slab segments in nature have a limited width along-strike, and they are attached to adjacent regions where the subducting plate descends at a steep angle. In the 2D models, it is implicitly assumed that continued plate convergence in the flat-slab region is driven by slab pull in the adjacent section where there is a dense oceanic plate. Therefore, how flat-slab subduction forms in the 3D world and the effects on the distribution of earthquakes, volcanism, and deformation remain unclear. One important direction for future work is to use 3D numerical models to investigate flat-slab subduction and unravel the poorly understood subduction dynamics, namely the development of flat-slab segments, and how these may relate to the observed seismicity and crustal deformation that occur in the continental interior. Using smaller-scale 3D models, a series of model tests could be carried out to understand the subsurface physical conditions required to deflect a segment of the oceanic plate into a flat geometry. This would allow several fundamental questions to be addressed, including: (1) what causes a flat slab segment in 3D; (2) does slab flattening create a tear at the edges (Fig. 7.2); and (3) how do these processes affect the surrounding overriding plate?

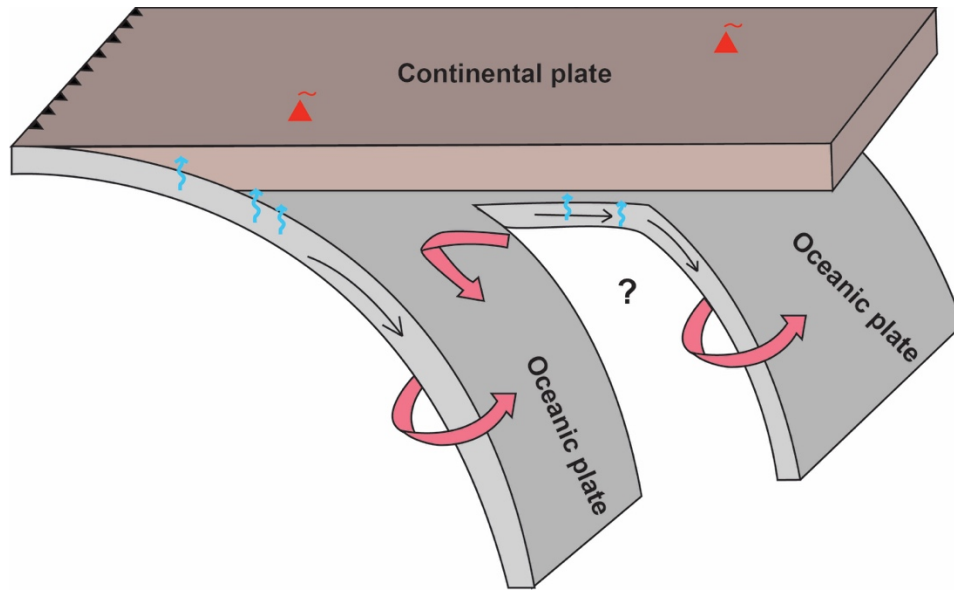


Figure 7.2. Flat-slab subduction in 3D. The black arrows indicate the plate motion. The blue arrows show the slab dehydration. The pink arrows are the possible edge flow patterns. The red triangles are volcanoes.

One other direction for future work follows the study in Chapter 4 on continental cooling during the development of a flat slab. Our results show that during the 12 Ma existence time of the present-day Pampean flat slab, the flat slab does not lead to enough cooling to explain the observed low surface heat flow. Therefore, other mechanisms are needed. Chapter 4 proposes that one possible explanation is that cool fluids released from the flat slab penetrate through the overlying continental mantle lithosphere may cool the material through advective heat transfer. Future work should look at the temperature field and petrologic structure of the subducting slab and the continental plate. Numerical models could be used to predict the amount of fluid carried by flat slab, the possible regions where slab dehydration occurs (Fig. 7.2), and the mantle lithosphere conditions needed to allow fluids to pass through. Such work is needed to assess whether advective cooling is a significant factor during flat-slab subduction. A detailed thermal-petrological study would

also provide insights into the evolution of arc magmatism. In some areas, the magmatic arc appears to move inland during the development of a flat slab (e.g., Kay and Abbruzzi, 1996). Dynamic models are needed to examine whether the thermal conditions in the slab will allow for fluids to be carried inland and then released where they can induce partial melting. Such models would also allow for an assessment of whether fluids from flat slabs can result in extensive hydration of the continental lithosphere, as proposed for western North America during Farallon flat-slab subduction (e.g., Humphreys et al., 2003).

In short, recent geophysical and geological studies on flat-slab subduction in the recent decades have made significant progress in understanding the geometry of the flat slab and the effects on the overriding plate. Geodynamic models, including the models in this thesis, provide important insights into the cause of flat-slab subduction and how this affects the thermal structure, stress field and deformation of the overlying continent over time. However, there are many other topics related to flat subduction that still need to be explored. As one of the main driving forces of tectonics, subduction alters both tectonic plates on the Earth's surface and the dynamics of the mantle in the Earth's interior. The study of the special form of the subduction, flat-slab subduction, as in this thesis, shows how both surface processes and Earth's inner dynamics are affected by subduction.

---

## References

---

- Abers, G. A., & Hacker, B. R. (2016). A MATLAB toolbox and Excel workbook for calculating the densities, seismic wave speeds, and major element composition of minerals and rocks at pressure and temperature. *Geochemistry, Geophysics, Geosystems*, 17(2), 616-624. <https://doi.org/10.1002/2015gc006171>
- Alvarado, P., Pardo, M., Gilbert, H., Miranda, S., Anderson, M., Saez, M., & Beck, S. (2009). Flat-slab subduction and crustal models for the seismically active Sierras Pampeanas region of Argentina. *Backbone of the Americas: Shallow subduction, plateau uplift, and ridge and terrane collision*, 204, 261-278. [https://doi.org/10.1130/2009.1204\(12\)](https://doi.org/10.1130/2009.1204(12))
- Anderson, M., Alvarado, P., Zandt, G., & Beck, S. (2007). Geometry and brittle deformation of the subducting Nazca Plate, Central Chile and Argentina. *Geophysical Journal International*, 171(1), 419-434. <https://doi.org/10.1111/j.1365-246x.2007.03483.x>
- Antonijevic, S. K., Wagner, L. S., Kumar, A., Beck, S. L., Long, M. D., Zandt, G., ... & Condori, C. (2015). The role of ridges in the formation and longevity of flat slabs. *Nature*, 524(7564), 212-215. <https://doi.org/10.1038/nature14648>
- Arrial, P. A., & Billen, M. I. (2013). Influence of geometry and eclogitization on oceanic plateau subduction. *Earth and Planetary Science Letters*, 363, 34-43. <https://doi.org/10.1016/j.epsl.2012.12.011>

- Artemieva, I. M., & Mooney, W. D. (2001). Thermal thickness and evolution of Precambrian lithosphere: A global study. *Journal of Geophysical Research: Solid Earth*, 106(B8), 16387-16414. <https://doi.org/10.1029/2000jb900439>
- Assumpção, M., Feng, M., Tassara, A., & Julià, J. (2013). Models of crustal thickness for South America from seismic refraction, receiver functions and surface wave tomography. *Tectonophysics*, 609, 82-96. <https://doi.org/10.1016/j.tecto.2012.11.014>
- Austrheim, H. (1991). Eclogite formation and dynamics of crustal roots under continental collision zones. *Terra Nova*, 3(5), 492-499. <https://doi.org/10.1111/j.1365-3121.1991.tb00184.x>
- Axen, G. J., van Wijk, J. W., & Currie, C. A. (2018). Basal continental mantle lithosphere displaced by flat-slab subduction. *Nature Geoscience*, 1. <https://doi.org/10.1038/s41561-018-0263-9>
- Bahadori, A., Holt, W. E., & Rasbury, E. T. (2018). Reconstruction modeling of crustal thickness and paleotopography of western North America since 36 Ma. *Geosphere*, 14(3), 1207-1231. <https://doi.org/10.1130/ges01604.1>
- Batchelor, G. K. (1967), *An Introduction to Fluid Dynamics*, Cambridge Univ. Press, Cambridge, U. K.
- Beaumont, C., Nguyen, M. H., Jamieson, R. A., & Ellis, S. (2006). Crustal flow modes in large hot orogens. *Geological Society, London, Special Publications*, 268(1), 91-145. <https://doi.org/10.1144/gsl.sp.2006.268.01.05>
- Bellahsen, N., Sébrier, M., & Siame, L. (2016). Crustal shortening at the Sierra Pie de Palo (Sierras Pampeanas, Argentina): near-surface basement folding and

- thrusting. *Geological Magazine*, 153(5-6), 992-1012.  
<https://doi.org/10.1017/S0016756816000467>
- Bevis, M. (1986). The curvature of Wadati-Benioff zones and the torsional rigidity of subducting plates. *Nature*, 323(6083), 52-53. <https://doi.org/10.1038/323052a0>
- Bilek, S. L., & Lay, T. (2018). Subduction zone megathrust earthquakes. *Geosphere*, 14(4), 1468-1500. <https://doi.org/10.1130/ges01608.1>
- Bird, P. (1988). Formation of the Rocky Mountains, western United States: A continuum computer model. *Science*, 239(4847), 1501–1507.  
<https://doi.org/10.1126/science.239.4847.1501>
- Bird, P. (1998). Kinematic history of the Laramide orogeny in latitudes 35–49 N, western United States. *Tectonics*, 17(5), 780-801. <https://doi.org/10.1029/98tc02698>
- Bishop, B. T., Beck, S. L., Zandt, G., Wagner, L., Long, M., Antonijevic, S. K., ... & Tavera, H. (2017). Causes and consequences of flat-slab subduction in southern Peru. *Geosphere*, 13(5), 1392-1407. <https://doi.org/10.1130/ges01440.1>
- Bloch, W., John, T., Kummerow, J., Salazar, P., Krüger, O.S. and Shapiro, S.A., 2018. Watching dehydration: Seismic indication for transient fluid pathways in the oceanic mantle of the subducting Nazca slab. *Geochemistry, Geophysics, Geosystems*, 19(9), pp.3189-3207. <https://doi.org/10.1029/2018gc007703>
- Bologna, M. S., Dragone, G. N., Muzio, R., Peel, E., Nuñez-Demarco, P., & Ussami, N. (2019). Electrical structure of the lithosphere from Rio de la Plata Craton to Paraná Basin: Amalgamation of cratonic and refertilized lithospheres in SW Gondwanaland. *Tectonics*, 38(1), 77-94. <https://doi.org/10.1029/2018tc005148>

- Burns, E. R., Williams, C. F., Ingebritsen, S. E., Voss, C. I., Spane, F. A., & DeAngelo, J. (2015). Understanding heat and groundwater flow through continental flood basalt provinces: insights gained from alternative models of permeability/depth relationships for the Columbia Plateau, USA. *Geofluids*, *15*(1-2), 120-138. <https://doi.org/10.1002/9781119166573.ch13>
- Cai, C., Wiens, D.A., Shen, W., Eimer, M. (2018). Water input into the Mariana subduction zone estimated from ocean-bottom seismic data. *Nature* *563*, 389-394. <https://doi.org/10.1038/s41586-018-0655-4>
- Capaldi, T. N., Horton, B. K., McKenzie, N. R., Mackaman-Lofland, C., Stockli, D. F., Ortiz, G., & Alvarado, P. (2020). Neogene retroarc foreland basin evolution, sediment provenance, and magmatism in response to flat slab subduction, western Argentina. *Tectonics*, *39*(7), e2019TC005958. <https://doi.org/10.1029/2019TC005958>
- Carrapa, B., DeCelles, P. G., & Romero, M. (2019). Early inception of the Laramide orogeny in southwestern Montana and northern Wyoming: Implications for models of flat-slab subduction. *Journal of Geophysical Research: Solid Earth*, *124*(2), 2102-2123. <https://doi.org/10.1029/2018JB016888>
- Cerpa, N. G., Wada, I., & Wilson, C. R. (2017). Fluid migration in the mantle wedge: Influence of mineral grain size and mantle compaction. *Journal of Geophysical Research: Solid Earth*, *122*(8), 6247-6268. <https://doi.org/10.1002/2017jb014046>
- Clauser, C., & Huenges, E. (1995). Thermal conductivity of rocks and minerals. *Rock physics and phase relations: a handbook of physical constants*, *3*, 105-126. <https://doi.org/10.1029/rf003p0105>

- Collo, G., Dávila, F. M., Nóbile, J., Astini, R. A., & Gehrels, G. (2011). Clay mineralogy and thermal history of the Neogene Vinchina Basin, central Andes of Argentina: Analysis of factors controlling the heating conditions. *Tectonics*, 30(4).  
<https://doi.org/10.1029/2010tc002841>
- Collo, G., Dávila, F. M., Teixeira, W., Nóbile, J. C., Sant, L. G., & Carter, A. (2017). Isotopic and thermochronologic evidence of extremely cold lithosphere associated with a slab flattening in the Central Andes of Argentina. *Basin Research*, 29(1), 16-40. <https://doi.org/10.1111/bre.12163>
- Collo, G., Ezpeleta, M., Dávila, F. M., Giménez, M., Soler, S., Martina, F., ... & Schiuma, M. (2018). Basin Thermal Structure in the Chilean-Pampean Flat Subduction Zone. *In the Evolution of the Chilean-Argentinean Andes* (pp. 537-564). Springer, Cham. [https://doi.org/10.1007/978-3-319-67774-3\\_21](https://doi.org/10.1007/978-3-319-67774-3_21)
- Coney, P. J., & Reynolds, S. J. (1977). Cordilleran Benioff zones. *Nature*, 270, 403–406.  
<http://doi.org/10.1038/270403a0>
- Coney, P. J., Jones, D. L., & Monger, J. W. (1980). Cordilleran suspect terranes. *Nature*, 288(5789), 329-333. <https://doi.org/10.1038/288329a0>
- Copeland, P., Currie, C. A., Lawton, T. F., & Murphy, M. A. (2017). Location, location, location: The variable lifespan of the Laramide orogeny. *Geology*, 45(3), 223-226.  
<https://doi.org/10.1130/G38810.1>
- Costa, C. H., & Finzi, C. V. (1996). Late Holocene faulting in the southeast Sierras Pampeanas of Argentina. *Geology*, 24(12), 1127-1130.  
[https://doi.org/10.1130/0091-7613\(1996\)024<1127:lhfits>2.3.co;2](https://doi.org/10.1130/0091-7613(1996)024<1127:lhfits>2.3.co;2)

- Cramer, F., Lithgow-Bertelloni, C. R., & Tackley, P. J. (2017). The dynamical control of subduction parameters on surface topography. *Geochemistry, Geophysics, Geosystems*, 18(4), 1661-1687. <https://doi.org/10.1002/2017gc006821>
- Currie, C. A., & Beaumont, C. (2011). Are diamond-bearing Cretaceous kimberlites related to low-angle subduction beneath western North America? *Earth and Planetary Science Letters*, 303(1-2), 59-70. <https://doi.org/10.1016/j.epsl.2010.12.036>
- Currie, C. A., & Hyndman, R. D. (2006). The thermal structure of subduction zone back arcs. *Journal of Geophysical Research: Solid Earth*, 111(B8). <https://doi.org/10.1029/2005jb004024>
- Davies, G.F., and Richards, M.A., (1992), Mantle convection, *J.Geol.*, 100, 151-206. [https://doi.org/10.1086/629582\\_](https://doi.org/10.1086/629582_)
- Dávila, F. M., & Lithgow-Bertelloni, C. (2015). Dynamic uplift during slab flattening. *Earth and Planetary Science Letters*, 425, 34-43. <https://doi.org/10.1016/j.epsl.2015.05.026>
- Dickinson, W.R. and Snyder, W.S. (1978). Plate tectonics of the Laramide orogeny. In Matthews, V. (Eds). Laramide folding associated with basement block faulting in the western United States. *Geological Society of America*. 151, 355–366. <https://doi.org/10.1130/mem151-p355>
- Dumitru, T. A. (1990). Subnormal Cenozoic geothermal gradients in the extinct Sierra Nevada magmatic arc: Consequences of Laramide and post-Laramide shallow-angle subduction. *Journal of Geophysical Research: Solid Earth*, 95(B4), 4925-4941. <https://doi.org/10.1029/jb095ib04p04925>

- Dumitru, T. A., Gans, P. B., Foster, D. A., & Miller, E. L. (1991). Refrigeration of the western Cordilleran lithosphere during Laramide shallow-angle subduction. *Geology*, *19*(11), 1145-1148. [https://doi.org/10.1130/0091-7613\(1991\)019<1145:rotwcl>2.3.co;2](https://doi.org/10.1130/0091-7613(1991)019<1145:rotwcl>2.3.co;2)
- English, J. M., & Johnston, S. T. (2004). The Laramide orogeny: What were the driving forces?. *International Geology Review*, *46*(9), 833-838. <https://doi.org/10.2747/0020-6814.46.9.833>
- English, J. M., Johnston, S. T., & Wang, K. (2003). Thermal modelling of the Laramide orogeny: testing the flat-slab subduction hypothesis. *Earth and Planetary Science Letters*, *214*(3-4), 619-632. [https://doi.org/10.1016/s0012-821x\(03\)00399-6](https://doi.org/10.1016/s0012-821x(03)00399-6)
- Espurt, N., Funicciello, F., Martinod, J., Guillaume, B., Regard, V., Faccenna, C., & Brusset, S. (2008). Flat subduction dynamics and deformation of the South American plate: Insights from analog modeling. *Tectonics*, *27*(3). <https://doi.org/10.1029/2007tc002175>
- Ferrand, T. P., Hilairet, N., Incel, S., Deldicque, D., Labrousse, L., Gasc, J., ... & Schubnel, A. (2017). Dehydration-driven stress transfer triggers intermediate-depth earthquakes. *Nature communications*, *8*(1), 1-11. <https://doi.org/10.1038/ncomms15247>
- Ferrari, L. (2004). Slab detachment control on mafic volcanic pulse and mantle heterogeneity in central Mexico. *Geology*, *32*(1), 77-80. <https://doi.org/10.1130/g19887.1>
- Ferrari, L., López-Martínez, M., Aguirre-Díaz, G., & Carrasco-Núñez, G. (1999). Space-time patterns of Cenozoic arc volcanism in central Mexico: From the Sierra

- Madre Occidental to the Mexican Volcanic Belt. *Geology*, 27(4), 303-306.  
[https://doi.org/10.1130/0091-7613\(1999\)027<0303:stpoca>2.3.co;2](https://doi.org/10.1130/0091-7613(1999)027<0303:stpoca>2.3.co;2)
- Fromm, R., Alvarado, P., Beck, S.L. Zandt, G. (2006). The April 9, 2001 Juan Fernández Ridge (Mw 6.7) tensional outer-rise earthquake and its aftershock sequence. *Journal of Seismology*, 10(2), 163-170. <https://doi.org/10.1007/s10950-006-9013-3>
- Fullsack, P. (1995). An arbitrary Lagrangian-Eulerian formulation for creeping flows and its application in tectonic models. *Geophysical Journal International*, 120(1), 1-23. <https://doi.org/10.1111/j.1365-246x.1995.tb05908.x>
- Gans, C. R., Beck, S. L., Zandt, G., Gilbert, H., Alvarado, P., Anderson, M., & Linkimer, L. (2011). Continental and oceanic crustal structure of the Pampean flat slab region, western Argentina, using receiver function analysis: new high-resolution results. *Geophysical Journal International*, 186(1), 45-58.  
<https://doi.org/10.1111/j.1365-246x.2011.05023.x>
- Gérault, M., Husson, L., Miller, M. S., & Humphreys, E. D. (2015). Flat-slab subduction, topography, and mantle dynamics in southwestern Mexico. *Tectonics*, 34(9), 1892-1909. <https://doi.org/10.1002/2015tc003908>
- Gerya, T. (2019). Introduction to numerical geodynamic modelling. Cambridge University Press. <https://doi.org/10.1017/cbo9780511809101.018>
- Gleason, G. C., & Tullis, J. (1995). A flow law for dislocation creep of quartz aggregates determined with the molten salt cell. *Tectonophysics*, 247(1-4), 1-23.  
[https://doi.org/10.1016/0040-1951\(95\)00011-b](https://doi.org/10.1016/0040-1951(95)00011-b)

- Grevenmeyer, I., Ranero, C. R., & Ivandic, M. (2018). Structure of oceanic crust and serpentization at subduction trenches. *Geosphere*, 14(2), 395-418.  
<https://doi.org/10.1130/ges01537.1>
- Griffin, W. L., O'Reilly, S. Y., Abe, N., Aulbach, S., Davies, R. M., Pearson, N. J., ... & Kivi, K. (2003). The origin and evolution of Archean lithospheric mantle. *Precambrian Research*, 127(1-3), 19-41. [https://doi.org/10.1016/s0301-9268\(03\)00180-3](https://doi.org/10.1016/s0301-9268(03)00180-3)
- Gripp, A. E., & Gordon, R. G. (2002). Young tracks of hotspots and current plate velocities. *Geophysical Journal International*, 150(2), 321-361.  
<https://doi.org/10.1046/j.1365-246x.2002.01627.x>
- Gutscher, M. A. (2002). Andean subduction styles and their effect on thermal structure and interplate coupling. *Journal of South American Earth Sciences*, 15(1), 3-10.  
[https://doi.org/10.1016/s0895-9811\(02\)00002-0](https://doi.org/10.1016/s0895-9811(02)00002-0)
- Gutscher, M. A., Maury, R., Eissen, J. P., & Bourdon, E. (2000b). Can slab melting be caused by flat subduction?. *Geology*, 28(6), 535-538.  
[https://doi.org/10.1130/0091-7613\(2000\)028<0535:csmcbcb>2.3.co;2](https://doi.org/10.1130/0091-7613(2000)028<0535:csmcbcb>2.3.co;2)
- Gutscher, M. A., Spakman, W., Bijwaard, H., & Engdahl, E. R. (2000a). Geodynamics of flat subduction: Seismicity and tomographic constraints from the Andean margin. *Tectonics*, 19(5), 814-833. <https://doi.org/10.1029/1999TC001152>
- Hacker, B. R., & Abers, G. A. (2004). Subduction Factory 3: An Excel worksheet and macro for calculating the densities, seismic wave speeds, and H<sub>2</sub>O contents of minerals and rocks at pressure and temperature. *Geochemistry, Geophysics, Geosystems*, 5(1). <https://doi.org/10.1029/2003gc000614>

- Hacker, B. R., Abers, G. A., & Peacock, S. M. (2003). Subduction factory 1. Theoretical mineralogy, densities, seismic wave speeds, and H<sub>2</sub>O contents. *Journal of Geophysical Research: Solid Earth*, 108(B1).  
<https://doi.org/10.1029/2001JB001127>
- Hager, B. H., & O'Connell, R. J. (1978). Subduction zone dip angles and flow driven by plate motion. *Tectonophysics*, 50(2-3), 111-133. [https://doi.org/10.1016/0040-1951\(78\)90130-0](https://doi.org/10.1016/0040-1951(78)90130-0)
- Hampel, A. (2002). The migration history of the Nazca Ridge along the Peruvian active margin: a re-evaluation. *Earth and Planetary Science Letters*, 203(2), 665-679.  
[https://doi.org/10.1016/s0012-821x\(02\)00859-2](https://doi.org/10.1016/s0012-821x(02)00859-2)
- Hamza, V. M., & Muñoz, M. (1996). Heat flow map of South America. *Geothermics*, 25(6), 599-646. [https://doi.org/10.1016/s0375-6505\(96\)00025-9](https://doi.org/10.1016/s0375-6505(96)00025-9)
- Hayes, G. P., Wald, D. J., & Johnson, R. L. (2012). Slab1. 0: A three-dimensional model of global subduction zone geometries. *Journal of Geophysical Research: Solid Earth*, 117(B1). <https://doi.org/10.1029/2011JB008524>
- Henry, S. G., & Pollack, H. N. (1988). Terrestrial heat flow above the Andean subduction zone in Bolivia and Peru. *Journal of Geophysical Research: Solid Earth*, 93(B12), 15153-15162. <https://doi.org/10.1029/jb093ib12p15153>
- Heron, P. J., Pysklywec, R. N., & Stephenson, R. (2016). Lasting mantle scars lead to perennial plate tectonics. *Nature Communications*, 7(1), 1-7.  
<https://doi.org/10.1038/ncomms11834>

- Heuret, A., & Lallemand, S. (2005). Plate motions, slab dynamics and back-arc deformation. *Physics of the Earth and Planetary Interiors*, 149(1-2), 31-51. <https://doi.org/10.1016/j.pepi.2004.08.022>
- Hirt, C. W., Amsden, A. A., & Cook, J. L. (1974). An arbitrary Lagrangian-Eulerian computing method for all flow speeds. *Journal of computational physics*, 14(3), 227-253. [https://doi.org/10.1016/0021-9991\(74\)90051-5](https://doi.org/10.1016/0021-9991(74)90051-5)
- Hildebrand, R. S. (2009). *Did westward subduction cause Cretaceous-Tertiary orogeny in the North American Cordillera?* (Vol. 457). Geological Society of America.
- Hofmann, A. W. (1997). Mantle geochemistry: the message from oceanic volcanism. *Nature*, 385(6613), 219-229. <https://doi.org/10.1038/385219a0>
- Hu, J., & Liu, L. (2016). Abnormal seismological and magmatic processes controlled by the tearing South American flat slabs. *Earth and Planetary Science Letters*, 450, 40-51. <https://doi.org/10.1016/j.epsl.2016.06.019>
- Huisman, R. S., & Beaumont, C. (2003). Symmetric and asymmetric lithospheric extension: Relative effects of frictional-plastic and viscous strain softening. *Journal of Geophysical Research: Solid Earth*, 108(B10). <https://doi.org/10.1029/2002jb002026>
- Humphreys, E. D., Schmandt, B., Bezada, M. J., & Perry-Houts, J. (2015). Recent craton growth by slab stacking beneath Wyoming. *Earth and Planetary Science Letters*, 429, 170-180. <https://doi.org/10.1016/j.epsl.2015.07.066>
- Humphreys, E., Hessler, E., Dueker, K., Farmer, G. L., Erslev, E., & Atwater, T. (2003). How Laramide-age hydration of North American lithosphere by the Farallon slab

- controlled subsequent activity in the western United States. *International Geology Review*, 45(7), 575-595. <https://doi.org/10.2747/0020-6814.45.7.575>
- Hyndman, R. D., Currie, C. A., & Mazzotti, S. P. (2005). Subduction zone backarcs, mobile belts, and orogenic heat. *GSA Today*, 15(2), 4-10. [https://doi.org/10.1130/1052-5173\(2005\)015<4:szbmba>2.0.co;2](https://doi.org/10.1130/1052-5173(2005)015<4:szbmba>2.0.co;2)
- International Seismological Centre (2020). On-line Bulletin, <https://doi.org/10.31905/D808B830>
- James, D., and S. Sacks (1999). Cenozoic formation of the central Andes: A geophysical perspective. In *Geology of Ore Deposits of the Central Andes*, B. Skinner (Eds). *Spec. Publ. Soc. Econ. Geol.*, 7, 1–25, <https://doi.org/10.5382/sp.07.01>
- Jarrard R.D., (1986), Relations among subduction parameters, *Rev. Geophys.*, 24, 217–284. <https://doi.org/10.1029/RG024i002p00217>
- Jaupart, C., & Mareschal, J.-C. (2014). Constraints on Crustal Heat Production from Heat Flow Data. *Treatise on Geochemistry*, 53-73. <https://doi.org/10.1016/b978-0-08-095975-7.00302-8>
- Jordan, T.E. and Allmendinger, R.W. (1986). The Sierras Pampeanas of Argentina; a modern analogue of Rocky Mountain foreland deformation. *American Journal of Science*, 286(10), 737-764. <https://doi.org/10.2475/ajs.286.10.737>
- Johnston, S. T., & Borel, G. D. (2007). The odyssey of the Cache Creek terrane, Canadian Cordillera: Implications for accretionary orogens, tectonic setting of Panthalassa, the Pacific superwell, and break-up of Pangea. *Earth and Planetary Science Letters*, 253(3-4), 415-428. <https://doi.org/10.1016/j.epsl.2006.11.002>

- Johnston, S. T. (2008). The cordilleran ribbon continent of North America. *Annu. Rev. Earth Planet. Sci.*, 36, 495-530.  
<https://doi.org/10.1146/annurev.earth.36.031207.124331>
- Karato, S. I. (1981). Rheology of the lower mantle. *Physics of the Earth and Planetary Interiors*, 24(1), 1-14. [https://doi.org/10.1016/0031-9201\(81\)90074-1](https://doi.org/10.1016/0031-9201(81)90074-1)
- Karato, S. I., & Wu, P. (1993). Rheology of the upper mantle: A synthesis. *Science*, 260(5109), 771-778. <https://doi.org/10.1126/science.260.5109.771>
- Karlstrom, K. E., & Humphreys, E. D. (1998). Persistent influence of Proterozoic accretionary boundaries in the tectonic evolution of southwestern North America: Interaction of cratonic grain and mantle modification events. *Rocky Mountain Geology*, 33(2), 161-179. <https://doi.org/10.2113/33.2.161>
- Kay, S. M., & Abbruzzi, J. M. (1996). Magmatic evidence for Neogene lithospheric evolution of the central Andean “flat-slab” between 30°S and 32°S. *Tectonophysics*, 259, 15-28. [https://doi.org/10.1016/0040-1951\(96\)00032-7](https://doi.org/10.1016/0040-1951(96)00032-7)
- Kay, S. M., & Mpodozis, C. (2002). Magmatism as a probe to the Neogene shallowing of the Nazca plate beneath the modern Chilean flat-slab. *Journal of South American Earth Sciences*, 15(1), 39-57. [https://doi.org/10.1016/s0895-9811\(02\)00005-6](https://doi.org/10.1016/s0895-9811(02)00005-6)
- Kim, Y., Miller, M. S., Pearce, F., & Clayton, R. W. (2012). Seismic imaging of the Cocos plate subduction zone system in central Mexico. *Geochemistry, Geophysics, Geosystems*, 13(7). <https://doi.org/10.1029/2012gc004033>
- Kirby, S., Engdahl, R. E., & Denlinger, R. (1996). Intermediate-depth intraslab earthquakes and arc volcanism as physical expressions of crustal and uppermost mantle metamorphism in subducting slabs. *Washington DC American*

- Geophysical Union Geophysical Monograph Series*, 96, 195-214.  
<https://doi.org/10.1029/GM096p0195>
- Kopp, H., Flueh, E. R., Papenberg, C., & Klaeschen, D. (2004). Seismic investigations of the O'Higgins Seamount Group and Juan Fernández Ridge: aseismic ridge emplacement and lithosphere hydration. *Tectonics*, 23(2).  
<https://doi.org/10.1029/2003tc001590>
- Korenaga, J., & Sager, W. W. (2012). Seismic tomography of Shatsky Rise by adaptive importance sampling. *Journal of Geophysical Research: Solid Earth*, 117(B8).  
<https://doi.org/10.1029/2012jb009248>
- Krystopowicz, N. J., & Currie, C. A. (2013). Crustal eclogitization and lithosphere delamination in orogens. *Earth and Planetary Science Letters*, 361, 195-207.  
<https://doi.org/10.1016/j.epsl.2012.09.056>
- Kumar, A., Wagner, L. S., Beck, S. L., Long, M. D., Zandt, G., Young, B., ... & Minaya, E. (2016). Seismicity and state of stress in the central and southern Peruvian flat slab. *Earth and Planetary Science Letters*, 441, 71-80.  
<https://doi.org/10.1016/j.epsl.2016.02.023>
- Lallemand, S., Heuret, A., & Boutelier, D. (2005). On the relationships between slab dip, back-arc stress, upper plate absolute motion, and crustal nature in subduction zones. *Geochemistry, Geophysics, Geosystems*, 6(9).  
<https://doi.org/10.1029/2005gc000917>
- Lewis, T. J., Hyndman, R. D., & Flück, P. (2003). Heat flow, heat generation, and crustal temperatures in the northern Canadian Cordillera: thermal control of tectonics.

*Journal of Geophysical Research: Solid Earth*, 108(B6).

<https://doi.org/10.1029/2002jb002090>

- Li, Z. X., & Li, X. H. (2007). Formation of the 1300-km-wide intracontinental orogen and postorogenic magmatic province in Mesozoic South China: a flat-slab subduction model. *Geology*, 35(2), 179-182. <https://doi.org/10.1130/g23193a.1>
- Lipman, P. W., Prostka, H. J., & Christiansen, R. L. (1972). A Discussion on volcanism and the structure of the Earth-Cenozoic volcanism and plate-tectonic evolution of the Western United States. I. Early and middle cenozoic. *Philosophical Transactions of the Royal Society of London. Series A, Mathematical and Physical Sciences*, 271(1213), 217-248. <https://doi.org/10.1098/rsta.1972.0008>
- Liu, L., Gurnis, M., Seton, M., Saleeby, J., Müller, R. D., & Jackson, J. M. (2010). The role of oceanic plateau subduction in the Laramide orogeny. *Nature Geoscience*, 3(5), 353. <https://doi.org/10.1038/ngeo829>
- Liu, L., Spasojević, S., & Gurnis, M. (2008). Reconstructing Farallon plate subduction beneath North America back to the Late Cretaceous. *Science*, 322(5903), 934-938. <https://doi.org/10.1126/science.1162921>
- Liu, S., & Currie, C. A. (2016). Farallon plate dynamics prior to the Laramide orogeny: Numerical models of flat subduction. *Tectonophysics*, 666, 33-47. <https://doi.org/10.1016/j.tecto.2015.10.010>
- Liu, X., & Currie, C. A. (2019). Influence of Upper Plate Structure on Flat-slab Depth: Numerical modeling of subduction dynamics. *Journal of Geophysical Research: Solid Earth*, 124(12), 13150–13167. <https://doi.org/10.1029/2019JB018653>

- Liu, X., Currie, C. A., & Wagner, L. S. (2022). Cooling of the continental plate during flat-slab subduction. *Geosphere*, 18(1), 49-68.  
<https://doi.org/10.1130/GES02402.1>
- Livaccari, R. F., & Perry, F. V. (1993). Isotopic evidence for preservation of Cordilleran lithospheric mantle during the Sevier-Laramide orogeny, western United States. *Geology*, 21(8), 719-722. [https://doi.org/10.1130/0091-7613\(1993\)021<0719:IEFPOC>2.3.CO;2](https://doi.org/10.1130/0091-7613(1993)021<0719:IEFPOC>2.3.CO;2)
- Livaccari, R. F., Burke, K., & Şengör, A. M. C. (1981). Was the Laramide Orogeny related to subduction of an oceanic plateau? *Nature*, 289(5795), 276-278.  
<https://doi.org/10.1038/289276a0>
- Löbens, S., Bense, F. A., Wemmer, K., Dunkl, I., Costa, C. H., Layer, P., & Siegesmund, S. (2011). Exhumation and uplift of the Sierras Pampeanas: preliminary implications from K–Ar fault gouge dating and low-T thermochronology in the Sierra de Comechingones (Argentina). *International Journal of Earth Sciences*, 100(2-3), 671-694. <https://doi.org/10.1007/s00531-010-0608-0>
- Mackwell, S. J., Zimmerman, M. E., & Kohlstedt, D. L. (1998). High-temperature deformation of dry diabase with application to tectonics on Venus. *Journal of Geophysical Research: Solid Earth*, 103(B1), 975-984.  
<https://doi.org/10.1029/97jb02671>
- Manea, V. C., & Gurnis, M. (2007). Subduction zone evolution and low viscosity wedges and channels. *Earth and Planetary Science Letters*, 264 (2007), 22–45.  
<https://doi.org/10.1016/j.epsl.2007.08.030>

- Manea, V. C., Manea, M., Ferrari, L., Orozco-Esquivel, T., Valenzuela, R. W., Husker, A., & Kostoglodov, V. (2017). A review of the geodynamic evolution of flat slab subduction in Mexico, Peru, and Chile. *Tectonophysics*, 695, 27-52.  
<https://doi.org/10.1016/j.tecto.2016.11.037>
- Manea, V. C., Pérez-Gussinyé, M., & Manea, M. (2012). Chilean flat slab subduction controlled by overriding plate thickness and trench rollback. *Geology*, 40(1), 35-38. <https://doi.org/10.1130/g32543.1>
- Marot, M., Monfret, T., Gerbault, M., Nolet, G., Ranalli, G., & Pardo, M. (2014). Flat versus normal subduction zones: a comparison based on 3-D regional travelttime tomography and petrological modelling of central Chile and western Argentina (29–35 S). *Geophysical Journal International*, 199(3), 1633-1654.  
<https://doi.org/10.1093/gji/ggu355>
- Martin, E. L., Collins, W. J., & Spencer, C. J. (2020). Laurentian origin of the Cuyania suspect terrane, western Argentina, confirmed by Hf isotopes in zircon. *Bulletin*, 132(1-2), 273-290. <https://doi.org/10.1130/b35150.1>
- Martini, M., Ferrari, L., López-Martínez, M., Cerca-Martínez, M., Valencia, V., Serrano-Durán, L., ... & Dickinson, W. R. (2009). Cretaceous–Eocene magmatism and Laramide deformation in southwestern Mexico: No role for terrane accretion. *Backbone of the Americas: Shallow subduction, plateau uplift, and ridge and terrane collision: Geological Society of America Memoir*, 204, 151-182.
- Martini, M., & Ferrari, L. (2011). Style and chronology of the Late Cretaceous shortening in the Zihuatanejo area (southwestern Mexico): Implications for the timing of the

- Mexican Laramide deformation. *Geosphere*, 7(6), 1469-1479.  
<https://doi.org/10.1130/GES00743.1>
- Martinod, J., Funicello, F., Faccenna, C., Labanieh, S., & Regard, V. (2005). Dynamical effects of subducting ridges: insights from 3-D laboratory models. *Geophysical Journal International*, 163(3), 1137-1150. <https://doi.org/10.1111/j.1365-246x.2005.02797.x>
- McGeary, S. U. S. A. N., Nur, A., & Ben-Avraham, Z. (1985). Spatial gaps in arc volcanism: The effect of collision or subduction of oceanic plateaus. *Tectonophysics*, 119(1-4), 195-221. [https://doi.org/10.1016/0040-1951\(85\)90039-3](https://doi.org/10.1016/0040-1951(85)90039-3)
- Meade, C., & Jeanloz, R. (1991). Deep-focus earthquakes and recycling of water into the Earth's mantle. *Science*, 252(5002), 68-72.  
<https://doi.org/10.1126/science.252.5002.68>
- Meier, M. A., Ampuero, J. P., & Heaton, T. H. (2017). The hidden simplicity of subduction megathrust earthquakes. *Science*, 357(6357), 1277-1281.  
<https://doi.org/10.1126/science.aan5643>
- Mibe, K., Kawamoto, T., Matsukage, K. N., Fei, Y., & Ono, S. (2011). Slab melting versus slab dehydration in subduction-zone magmatism. *Proceedings of the National Academy of Sciences*, 108(20), 8177-8182.  
<https://doi.org/10.1073/pnas.1010968108>
- Miller, H., & Söllner, F. (2005). The Famatina complex (NW Argentina): back-docking of an island arc or terrane accretion? Early Palaeozoic geodynamics at the western

- Gondwana margin. *Geological Society, London, Special Publications*, 246(1), 241-256. <https://doi.org/10.1144/gsl.sp.2005.246.01.08>
- Monger, J. W. H., Price, R. A., & Tempelman-Kluit, D. J. (1982). Tectonic accretion and the origin of the two major metamorphic and plutonic belts in the Canadian Cordillera. *Geology*, 10(2), 70-75. [https://doi.org/10.1130/0091-7613\(1982\)10<70:TAATOO>2.0.CO;2](https://doi.org/10.1130/0091-7613(1982)10<70:TAATOO>2.0.CO;2)
- Müller, R. D., Sdrolias, M., Gaina, C., & Roest, W. R. (2008). Age, spreading rates, and spreading asymmetry of the world's ocean crust. *Geochemistry, Geophysics, Geosystems*, 9(4). <https://doi.org/10.1029/2007gc001743>
- Muñoz, M. (2005). No flat Wadati–Benioff Zone in the central and southern central Andes. *Tectonophysics*, 395(1-2), 41-65. <https://doi.org/10.1016/j.tecto.2004.09.002>
- Norabuena, E. O., Dixon, T. H., Stein, S., & Harrison, C. G. (1999). Decelerating Nazca–South America and Nazca–Pacific plate motions. *Geophysical Research Letters*, 26(22), 3405-3408. <https://doi.org/10.1029/1999gl005394>
- O'Driscoll, L. J., Humphreys, E. D., & Saucier, F. (2009). Subduction adjacent to deep continental roots: Enhanced negative pressure in the mantle wedge, mountain building and continental motion. *Earth and Planetary Science Letters*, 280(1-4), 61-70. <https://doi.org/10.1016/j.epsl.2009.01.020>
- Oxburgh, E. R., & Parmentier, E. M. (1978). Thermal processes in the formation of continental lithosphere. *Philosophical Transactions of the Royal Society of London. Series A, Mathematical and Physical Sciences*, 288(1355), 415-429. <https://doi.org/10.1098/rsta.1978.0025>

- Oyhantçabal, P., Siegesmund, S., & Wemmer, K. (2011). The Río de la Plata Craton: a review of units, boundaries, ages and isotopic signature. *International Journal of Earth Sciences*, 100(2-3), 201-220. <https://doi.org/10.1007/s00531-010-0580-8>
- Pankhurst, R. J., Rapela, C. W., Saavedra, J., Baldo, E., Dahlquist, J., Pascua, I., & Fanning, C. M. (1998). The Famatinian magmatic arc in the central Sierras Pampeanas: an Early to Mid-Ordovician continental arc on the Gondwana margin. *Geological Society, London, Special Publications*, 142(1), 343-367. <https://doi.org/10.1144/gsl.sp.1998.142.01.17>
- Pasyanos, M. E., Masters, T. G., Laske, G., & Ma, Z. (2014). LITHO1. 0: An updated crust and lithospheric model of the Earth. *Journal of Geophysical Research: Solid Earth*, 119(3), 2153-2173. <https://doi.org/10.1002/2013jb010626>
- Pérez-Campos, X., Kim, Y., Husker, A., Davis, P. M., Clayton, R. W., Iglesias, A., ... & Gurnis, M. (2008). Horizontal subduction and truncation of the Cocos Plate beneath central Mexico. *Geophysical research letters*, 35(18). <https://doi.org/10.1029/2008gl035127>
- Perry, M., Spinelli, G. A., Wada, I., & He, J. (2016). Modeled temperatures and fluid source distributions for the Mexican subduction zone: Effects of hydrothermal circulation and implications for plate boundary seismic processes. *Geochemistry, Geophysics, Geosystems*, 17(2), 550-570. <https://doi.org/10.1002/2015gc006148>
- Pfiffner, O. A. (2006). Thick-skinned and thin-skinned styles of continental contraction. *Special Papers-Geological Society of America*, 414, 153. [https://doi.org/10.1130/2006.2414\(09\)](https://doi.org/10.1130/2006.2414(09))
- Pfiffner, O. A. (2017). Thick-skinned and thin-skinned tectonics: a global perspective. *Geosciences*, 7(3), 71. <https://doi.org/10.3390/geosciences7030071>

- Pilger, R. H. (1984). Cenozoic plate kinematics, subduction and magmatism: South American Andes. *Journal of the Geological Society*, 141(5), 793-802.  
<https://doi.org/10.1144/gsjgs.141.5.0793>
- Pope, D. C., & Willett, S. D. (1998). Thermal-mechanical model for crustal thickening in the central Andes driven by ablative subduction. *Geology*, 26(6), 511-514.  
[https://doi.org/10.1130/0091-7613\(1998\)026<0511:tmmfct>2.3.co;2](https://doi.org/10.1130/0091-7613(1998)026<0511:tmmfct>2.3.co;2)
- Porter, R., Gilbert, H., Zandt, G., Beck, S., Warren, L., Calkins, J., ... & Anderson, M. (2012). Shear wave velocities in the Pampean flat-slab region from Rayleigh wave tomography: Implications for slab and upper mantle hydration. *Journal of Geophysical Research: Solid Earth*, 117(B11).  
<https://doi.org/10.1029/2012jb009350>
- Portner, D. E., Beck, S., Zandt, G., & Scire, A. (2017). The nature of subslab slow velocity anomalies beneath South America. *Geophysical Research Letters*, 44(10), 4747-4755. <https://doi.org/10.1002/2017gl073106>
- Portner, D. E., Beck, S., Zandt, G., & Scire, A. (2017). The nature of subslab slow velocity anomalies beneath South America. *Geophysical Research Letters*, 44(10), 4747-4755. <https://doi.org/10.1002/2017gl073106>
- Pysklywec, R. N., & Beaumont, C. (2004). Intraplate tectonics: feedback between radioactive thermal weakening and crustal deformation driven by mantle lithosphere instabilities. *Earth and Planetary Science Letters*, 221(1-4), 275-292.  
[https://doi.org/10.1016/s0012-821x\(04\)00098-6](https://doi.org/10.1016/s0012-821x(04)00098-6)
- Quinteros, J., & Sobolev, S. V. (2013). Why has the Nazca plate slowed since the Neogene?. *Geology*, 41(1), 31-34. <https://doi.org/10.1130/g33497.1>

- Ramos, V. A. (1988). Tectonics of the Late Proterozoic early Paleozoic: a collisional history of southern South America. *Episodes*, 11(3), 168-174.  
<https://doi.org/10.18814/epiiugs/1988/v11i3/003>
- Ramos, V. A. (1994). Terranes of southern Gondwanaland and their control in the Andean structure (30–33 S latitude). In *Tectonics of the southern Central Andes* (pp. 249-261). Springer, Berlin, Heidelberg. [https://doi.org/10.1007/978-3-642-77353-2\\_18](https://doi.org/10.1007/978-3-642-77353-2_18)
- Ramos, V. A. (2004). Cuyania, an exotic block to Gondwana: review of a historical success and the present problems. *Gondwana Research*, 7(4), 1009-1026.  
[https://doi.org/10.1016/s1342-937x\(05\)71081-9](https://doi.org/10.1016/s1342-937x(05)71081-9)
- Ramos, V. A., & Folguera, A. (2009). Andean flat-slab subduction through time. *Geological Society, London, Special Publications*, 327(1), 31-54.  
<https://doi.org/10.1144/sp327.3>
- Ramos, V. A., Cristallini, E. O., & Pérez, D. J. (2002). The Pampean flat-slab of the Central Andes. *Journal of South American earth sciences*, 15(1), 59-78.  
<https://doi.org/10.1016/j.tecto.2015.11.019>
- Ramos, V. A., Vujovich, G., Martino, R., & Otamendi, J. (2010). Pampia: a large cratonic block missing in the Rodinia supercontinent. *Journal of Geodynamics*, 50(3-4), 243-255. <https://doi.org/10.1016/j.jog.2010.01.019>
- Ranero, C.R., Phipps Morgan, J., McIntosh, K., Reichert, C. (2003). Bending-related faulting and mantle serpentinitization at the Middle America trench. *Nature* 425, 367 – 373. <https://doi.org/10.1038/nature01961>

- Rapela, C. W., Pankhurst, R. J., Casquet, C., Fanning, C. M., Baldo, E. G., González-Casado, J. M., ... & Dahlquist, J. (2007). The Río de la Plata craton and the assembly of SW Gondwana. *Earth-Science Reviews*, 83(1-2), 49-82.  
[https://doi.org/10.1130/2007.2423\(01\)](https://doi.org/10.1130/2007.2423(01))
- Regnier, M., Chatelain, J. L., Smalley Jr, R., Chiu, J. M., Isacks, B. L., & Araujo, M. (1992). Seismotectonics of Sierra Pie de Palo, a basement block uplift in the Andean foreland of Argentina. *Bulletin of the Seismological Society of America*, 82(6), 2549-2571.
- Richardson, T., Ridgway, K. D., Gilbert, H., Martino, R., Enkelmann, E., Anderson, M., & Alvarado, P. (2013). Neogene and Quaternary tectonics of the Eastern Sierras Pampeanas, Argentina: Active intraplate deformation inboard of flat-slab subduction. *Tectonics*, 32(3), 780-796. <https://doi.org/10.1002/tect.20054>
- Rodgers, J. (1949). Evolution of thought on structure of middle and southern Appalachians. *AAPG Bulletin*, 33(10), 1643-1654.  
<https://doi.org/10.1306/3d933e00-16b1-11d7-8645000102c1865d>
- Rodríguez-González, J., Negredo, A. M., & Billen, M. I. (2012). The role of the overriding plate thermal state on slab dip variability and on the occurrence of flat subduction. *Geochemistry, Geophysics, Geosystems*, 13(1).  
<https://doi.org/10.1029/2011gc003859>
- Rosenbaum, G., Giles, D., Saxon, M., Betts, P. G., Weinberg, R. F., & Duboz, C. (2005). Subduction of the Nazca Ridge and the Inca Plateau: Insights into the formation of ore deposits in Peru. *Earth and Planetary Science Letters*, 239(1-2), 18-32.  
<https://doi.org/10.1016/j.epsl.2005.08.003>

- Ruiz, F., & Introcaso, A. (2004). Curie point depths beneath Precordillera Cuyana and Sierras Pampeanas obtained from spectral analysis of magnetic anomalies. *Gondwana Research*, 7(4), 1133-1142. [https://doi.org/10.1016/s1342-937x\(05\)71089-3](https://doi.org/10.1016/s1342-937x(05)71089-3)
- Sánchez, M. A., Ariza, J. P., García, H. P., Gianni, G. M., Weidmann, M. C., Folguera, A., ... & Martínez, M. P. (2018). Thermo-mechanical analysis of the Andean lithosphere over the Chilean-Pampean flat-slab region. *Journal of South American Earth Sciences*, 87, 247-257. <https://doi.org/10.1016/j.jsames.2017.09.036>
- Sarkarinejad, K., & Goftari, F. (2019). Thick-skinned and thin-skinned tectonics of the Zagros orogen, Iran: Constraints from structural, microstructural and kinematics analyses. *Journal of Asian Earth Sciences*, 170, 249-273. <https://doi.org/10.1016/j.jseaes.2018.10.021>
- Schepers, G., Van Hinsbergen, D. J., Spakman, W., Kosters, M. E., Boschman, L. M., & McQuarrie, N. (2017). South-American plate advance and forced Andean trench retreat as drivers for transient flat subduction episodes. *Nature communications*, 8, 15249. <https://doi.org/10.1038/ncomms15249>
- Schmidt, M. W., & Poli, S. (1998). Experimentally based water budgets for dehydrating slabs and consequences for arc magma generation. *Earth and Planetary Science Letters*, 163(1-4), 361-379. [https://doi.org/10.1016/s0012-821x\(98\)00142-3](https://doi.org/10.1016/s0012-821x(98)00142-3)
- Scire, A., Zandt, G., Beck, S., Long, M., Wagner, L., Minaya, E., & Tavera, H. (2016). Imaging the transition from flat to normal subduction: Variations in the structure of the Nazca slab and upper mantle under southern Peru and northwestern

- Bolivia. *Geophysical Journal International*, 204(1), 457-479.  
<https://doi.org/10.1093/gji/ggv452>
- Skinner, S. M., & Clayton, R. W. (2011). An evaluation of proposed mechanisms of slab flattening in central Mexico. *Pure and Applied geophysics*, 168(8-9), 1461-1474.  
<https://doi.org/10.1007/s00024-010-0200-3>
- Skinner, S. M., & Clayton, R. W. (2013). The lack of correlation between flat slabs and bathymetric impactors in South America. *Earth and Planetary Science Letters*, 371, 1-5. <https://doi.org/10.1016/j.epsl.2013.04.013>
- Smalley Jr, R., & Isacks, B. L. (1990). Seismotectonics of thin-and thick-skinned deformation in the Andean Foreland from local network data: Evidence for a seismogenic lower crust. *Journal of Geophysical Research: Solid Earth*, 95(B8), 12487-12498. <https://doi.org/10.1029/JB095iB08p12487>
- Smith, D. (2020). Trace elements in Cr-pyrope from the Navajo volcanic field of the Colorado Plateau, SW USA, and implications for the mantle wedge during low-angle subduction. *Lithos*, 105460. <https://doi.org/10.1016/j.lithos.2020.105460>
- Snelson, C. M., Henstock, T. J., Keller, G. R., Miller, K. C., & Levander, A. (1998). Crustal and uppermost mantle structure along the Deep Probe seismic profile. *Rocky Mountain Geology*, 33(2), 181-198.  
<https://doi.org/10.2113/33.2.181>
- Stein, C. A., & Stein, S. (1992). A model for the global variation in oceanic depth and heat flow with lithospheric age. *Nature*, 359(6391), 123-129.  
<https://doi.org/10.1038/359123a0>

- Stern, R. J. (2002). Subduction zones. *Reviews of geophysics*, 40(4), 3-1.  
<https://doi.org/10.1029/2001rg000108>
- Stevens Goddard, A. L., & Carrapa, B. (2018). Using basin thermal history to evaluate the role of Miocene–Pliocene flat-slab subduction in the southern Central Andes (27° S–30° S). *Basin Research*, 30(3), 564-585. <https://doi.org/10.1111/bre.12265>
- Stevenson, D. J., & Turner, J. S. (1977). Angle of subduction. *Nature*, 270(5635), 334.  
<https://doi.org/10.1038/270334a0>
- Syracuse, E. M., & Abers, G. A. (2006). Global compilation of variations in slab depth beneath arc volcanoes and implications. *Geochemistry, Geophysics, Geosystems*, 7(5). <https://doi.org/10.1029/2005gc001045>
- Syracuse, E. M., van Keken, P. E., & Abers, G. A. (2010). The global range of subduction zone thermal models. *Physics of the Earth and Planetary Interiors*, 183(1-2), 73-90. <https://doi.org/10.1016/j.pepi.2010.02.004>
- Taramón, J. M., Rodríguez-González, J., Negredo, A. M., & Billen, M. I. (2015). Influence of cratonic lithosphere on the formation and evolution of flat slabs: Insights from 3-D time-dependent modeling. *Geochemistry, Geophysics, Geosystems*, 16(9), 2933-2948. <https://doi.org/10.1002/2015gc005940>
- Tatsumi, Y., & Eggins, S. (1995). Subduction zone magmatism (Vol. 1). Wiley.
- Thomas, W. A., & Astini, R. A. (1996). The Argentine precordillera: a traveler from the Ouachita embayment of North American Laurentia. *Science*, 273(5276), 752-757.  
<https://doi.org/10.1126/science.273.5276.752>

- Till, C. B., Grove, T. L., & Withers, A. C. (2012). The beginnings of hydrous mantle wedge melting. *Contributions to Mineralogy and Petrology*, 163(4), 669-688. <https://doi.org/10.1007/s00410-011-0692-6>
- Torsvik, T. H., Müller, R. D., Van der Voo, R., Steinberger, B., & Gaina, C. (2008). Global plate motion frames: Toward a unified model. *Reviews of Geophysics*, 46(3). <https://doi.org/10.1029/2007rg000227>
- Tovish, A., Schubert, G., & Luyendyk, B. P. (1978). Mantle flow pressure and the angle of subduction: Non-Newtonian corner flows. *Journal of Geophysical Research: Solid Earth*, 83(B12), 5892-5898. <https://doi.org/10.1029/jb083ib12p05892>
- Turcotte, D. L., & Schubert, G. (2002). *Geodynamics*: New York, Cambridge University Press.
- Urbina, N. P., Sruoga, P., & Malvicini, L. (1997). Late Tertiary gold-bearing volcanic belt in the Sierras Pampeanas of San Luis, Argentina. *International Geology Review*, 39(4), 287-306. <https://doi.org/10.1080/00206819709465272>
- Usui, T., Nakamura, E., Kobayashi, K., Maruyama, S., & Helmstaedt, H. (2003). Fate of the subducted Farallon plate inferred from eclogite xenoliths in the Colorado Plateau. *Geology*, 31(7), 589-592. [https://doi.org/10.1130/0091-7613\(2003\)031<0589:fotsfp>2.0.co;2](https://doi.org/10.1130/0091-7613(2003)031<0589:fotsfp>2.0.co;2)
- Uyeda, S., & Watanabe, T. (1982). Terrestrial heat flow in western South America. *Tectonophysics*, 83(1-2), 63-70. [https://doi.org/10.1016/0040-1951\(82\)90007-5](https://doi.org/10.1016/0040-1951(82)90007-5)

- van Hunen, J., & Allen, M. B. (2011). Continental collision and slab break-off: A comparison of 3-D numerical models with observations. *Earth and Planetary Science Letters*, 302(1-2), 27-37. <https://doi.org/10.1016/j.epsl.2010.11.035>
- van Hunen, J., van den Berg, A. P., & Vlaar, N. J. (2000). A thermo-mechanical model of horizontal subduction below an overriding plate. *Earth and Planetary Science Letters*, 182(2), 157-169. [https://doi.org/10.1016/S0012-821X\(00\)00240-5](https://doi.org/10.1016/S0012-821X(00)00240-5)
- van Hunen, J., van Den Berg, A. P., & Vlaar, N. J. (2002). On the role of subducting oceanic plateaus in the development of shallow flat subduction. *Tectonophysics*, 352(3-4), 317-333. [https://doi.org/10.1016/s0040-1951\(02\)00263-9](https://doi.org/10.1016/s0040-1951(02)00263-9)
- van Hunen, J., van den Berg, A. P., & Vlaar, N. J. (2004). Various mechanisms to induce present-day shallow flat subduction and implications for the younger Earth: a numerical parameter study. *Physics of the Earth and Planetary Interiors*, 146(1-2), 179-194. <https://doi.org/10.1016/j.pepi.2003.07.027>
- van Keken, P. E., Hacker, B. R., Syracuse, E. M., & Abers, G. A. (2011). Subduction factory: 4. Depth-dependent flux of H<sub>2</sub>O from subducting slabs worldwide. *Journal of Geophysical Research: Solid Earth*, 116(B1). <https://doi.org/10.1029/2010jb007922>
- Vlaar, N. J. (1983). Thermal anomalies and magmatism due to lithospheric doubling and shifting. *Earth and Planetary Science Letters*, 65(2), 322-330. [https://doi.org/10.1016/0012-821x\(83\)90170-x](https://doi.org/10.1016/0012-821x(83)90170-x)
- Von Huene, R., Corvalán, J., Flueh, E. R., Hinz, K., Korstgard, J., Ranero, C. R., & Weinrebe, W. (1997). Tectonic control of the subducting Juan Fernández Ridge

- on the Andean margin near Valparaiso, Chile. *Tectonics*, 16(3), 474-488.  
<https://doi.org/10.1029/96tc03703>
- Wada, I., & Wang, K. (2009). Common depth of slab-mantle decoupling: Reconciling diversity and uniformity of subduction zones. *Geochemistry, Geophysics, Geosystems*, 10(10). <https://doi.org/10.1029/2009gc002570>
- Wagner, L. S., Anderson, M. L., Jackson, J. M., Beck, S. L., & Zandt, G. (2008). Seismic evidence for orthopyroxene enrichment in the continental lithosphere. *Geology*, 36(12), 935-938. <https://doi.org/10.1130/g25108a.1>
- Wagner, L. S., Beck, S., & Zandt, G. (2005). Upper mantle structure in the south central Chilean subduction zone (30 to 36 S). *Journal of Geophysical Research: Solid Earth*, 110(B1). <https://doi.org/10.1029/2004jb003238>
- Wagner, L. S., Beck, S., Zandt, G., & Ducea, M. N. (2006). Depleted lithosphere, cold, trapped asthenosphere, and frozen melt puddles above the flat slab in central Chile and Argentina. *Earth and Planetary Science Letters*, 245(1-2), 289-301.  
<https://doi.org/10.1016/j.epsl.2006.02.014>
- Wagner, L.S., Caddick, M.J., Kumar, A., Beck, S.L., and Long, M.D. (2020) Effects of Oceanic Crustal Thickness on Intermediate Depth Seismicity. *Front. Earth Sci.*, p.8-244. <https://doi.org/10.3389/feart.2020.00244>
- Warren, C. J., Beaumont, C., & Jamieson, R. A. (2008). Formation and exhumation of ultra-high-pressure rocks during continental collision: Role of detachment in the subduction channel. *Geochemistry, Geophysics, Geosystems*, 9(4).  
<https://doi.org/10.1029/2007GC001839>

- Warren, C. J., Beaumont, C., & Jamieson, R. A. (2008). Formation and exhumation of ultra-high-pressure rocks during continental collision: Role of detachment in the subduction channel. *Geochemistry, Geophysics, Geosystems*, 9, Q04019.  
<https://doi.org/10.1029/2007GC001839>
- Willett, S.D. (1999). Rheological dependence of extension in wedge models of convergent orogens. *Tectonophysics*, 305(4), 419-435.  
[https://doi.org/10.1016/S0040-1951\(99\)00034-7](https://doi.org/10.1016/S0040-1951(99)00034-7)
- Woods, M. T., & Okal, E. A. (1994). The structure of the Nazca ridge and Sala y Gomez seamount chain from the dispersion of Rayleigh waves. *Geophysical Journal International*, 117(1), 205-222. <https://doi.org/10.1111/j.1365-246x.1994.tb03313.x>
- Worthington, L. L., Miller, K. C., Erslev, E. A., Anderson, M. L., Chamberlain, K. R., Sheehan, A. F., ... & Siddoway, C. S. (2016). Crustal structure of the Bighorn Mountains region: Precambrian influence on Laramide shortening and uplift in north-central Wyoming. *Tectonics*, 35(1), 208-236.  
<https://doi.org/10.1002/2015tc003840>
- Yáñez, G. A., Ranero, C. R., von Huene, R., & Díaz, J. (2001). Magnetic anomaly interpretation across the southern central Andes (32–34 S): The role of the Juan Fernández Ridge in the late Tertiary evolution of the margin. *Journal of Geophysical Research: Solid Earth*, 106(B4), 6325-6345.  
<https://doi.org/10.1029/2000jb900337>
- Yáñez, G., Cembrano, J., Pardo, M., Ranero, C., & Selles, D. (2002). The Challenger–Juan Fernández–Maipo major tectonic transition of the Nazca–Andean subduction

system at 33–34 S: geodynamic evidence and implications. *Journal of South American Earth Sciences*, 15(1), 23-38. [https://doi.org/10.1016/s0895-9811\(02\)00004-4](https://doi.org/10.1016/s0895-9811(02)00004-4)

Ziagos, J. P., Blackwell, D. D., & Mooser, F. (1985). Heat flow in southern Mexico and the thermal effects of subduction. *Journal of Geophysical Research: Solid Earth*, 90(B7), 5410-5420. <https://doi.org/10.1029/jb090ib07p05410>